ABSTRACT

HIGH SPIN STATES IN ^{168}Yb AND ^{128}Ce

By

José Luiz de Santana Carvalho

The high spin states of ^{168}Yb and ^{128}Ce have been studied using in-beam gamma ray spectroscopy. The A ~ 128 region is regarded to be transitional between prolate-deformed and spherical shape. In such deformed regions, the observed anomalous behavior at large angular momentum values in the yrast sequence (backbending) results from the crossing of the ground state rotational band with an aligned quasi-particle band. For ^{168}Yb, $i_{13/2}$ neutrons are involved in this phenomenon, and for ^{128}Ce, $h_{11/2}$ protons.

Several two-quasiparticle bands were observed in ^{168}Yb through the ^{166}Er $(\alpha,2n)$ reaction. Of particular interest is the 5$^-$ isomer and associated band structure identified to 11$^-$, which was determined to be two-quasineutron with some proton character mixed in. The γ-vibrational band was extended up to spin 11$^+$, and displayed a perturbed structure that probably results from mixing with nearby bands.

Jose Luiz de Santana Carvalho

The levels in ^{128}Ce were populated via the ^{112}Cd(^{20}Ne,4n) reaction, and the excitation γ-rays were observed through a multi-Ge detector array. The yrast sequence was observed up to spin 24^+, and a strong backbend is observed around $\hbar\omega = 0.31$ MeV. A pair of two-quasiparticle bands were determined at 1890 keV and 1989 keV, for the lowest observed level. For the former, a $h_{11/2}$ two-quasiproton band structure has been tentatively assigned.

Both isotopes were used to test the applicability of the Cranking Shell Model in the different deformed regions. The behavior of the yrast band was generally well predicted, while for the side-bands difficulties were encountered in trying to describe the amount of relative alignment as a function of angular momentum.

HIGH SPIN STATES IN ^{168}Yb AND ^{128}Ce

By

Jose´ Luiz de Santana Carvalho

A DISSERTATION

Submitted to

Michigan State University

in partial fulfillment of the requirements

for the degree of

DOCTOR OF PHILOSOPHY

Department of Chemistry
Program in Nuclear Chemistry

1982

ACKNOWLEDGMENTS

TABLE OF CONTENTS

LIST OF TABLES

LIST OF FIGURES

CHAPTER I

INTRODUCTION

The main goal of experimental nuclear spectroscopy is to construct the intrinsic, vibrational and rotational spectra of nuclei and relate them to the dynamics of the nucleus according to current ideas and theories. Accordingly, the purpose of this study was to extend any of the previously observed bands, and identify and characterize any additional multiparticle structures of two nuclei, ^{168}Yb and ^{128}Ce.

The deformed rare-earth ^{168}Yb isotope is a slightly neutron-deficient nucleus whose ground state rotational band has been extensively studied, theoretically and experimentally. Yet not much is known about the side-bands of this nucleus as well as of the other neighboring isotopes. With that in mind, a series of studies on several Yb isotopes was started at Michigan State University. These experiments were performed at the M.S.U. sector-focused isochronous cyclotron running in the N=2 harmonic mode for alpha-particle beams in the 25-50 MeV energy range. The investigative technique, in-beam γ-ray spectroscopy, was used because of the detailed information it yields on the intra- and interband transitions, and therefore on the association of the observed bands with certain Nilsson (deformed orbitals) levels and related nuclear behavior.

Most of the computer codes used in this work were developed by previous students. Especially useful codes were the three-parameter event recording and sorting programs for off-line analysis. The high resolution detectors used were Ge(Li) and Ge (intrinsic) and were of reasonable timing quality and efficiency. The Yb experiments were performed during the last year of cyclotron operation before the construction of a new superconducting cyclotron (K=500) was initiated.

When this work was initiated, not much was known about the yrast band and nothing about the sidebands of the highly neutron-deficient ^{128}Ce. Therefore, a series of studies was started at Oak Ridge National Laboratory to investigate the lighter Ce isotopes through detailed in-beam γ-ray spectroscopy. The experiments performed are representative of a new trend in experimental nuclear spectroscopy where the reaction chamber is surrounded by a battery of Ge(Li) and Ge detectors. Since (Heavy Ion, xn) reactions in this region involve high multiplicity events, such multi-Ge detector arrangement is useful in increasing the data collection efficiency. This is especially true when the data acquisition rate of the system as a whole has an upper limit set by the software of the computer. By using large total γ-ray energy filters it is possible to greatly decrease the intensity of the unwanted channels in the data, as well as the contribution to the background from Coulomb excitations. This is necessary because in this deformed region, unfortunately, the compound nucleus reactions produce many reaction channels due to unfavorable balance between protons and neutrons. In the Ce experiments 7 Ge(Li) detectors and 2

Na(I) detectors (acting as a total γ-ray energy filter) were used, and coincidence and angular distribution results could be obtained in one comprehensive experiment. Exhaustive and long analysis is still necessary to sort out the data.

For these experiments, the Oak Ridge Isochronous Cyclotron was used at one of its lowest energy settings for ^{20}Ne beams. The data taking was done with three different computers that operated the basic electronics, the CAMAC crate and the event-recording programs. Especially useful were the Perkin-Elmer 3220 computer and the assorted peripherals that enable close monitoring of the experiment. Some of the computer codes used were developed for these experiments, and since then software improvements have been made to make the codes more flexible and powerful.

Much information was obtained for both nuclei studied here, and many new states were sorted out from the data and placed into single-particle or collective bands. This work has also revealed additional experiments that would be interesting in order to obtain more information about other side bands for both nuclei. Some of the theoretical calculations performed involved the Cranking Shell Model. This model has extended the concepts involved in the Nilsson deformed potential to include the rotation of the nucleus, and how this rotation affects the nuclear orbitals in order to explain the behavior of the nucleus at high excitation energy.

Since 1979 more intense theoretical work has been done with this model, and its success has been quite remarkable, especially in the rare-earth deformed region, in explaining many features of single-particle and rotational spectra. But very few experimental calculations had been made in the A $\sim$ 130 region. In this dissertation, however, the Cranking Shell Model is used to explain some features of the observed bands in ^{128}Ce.

The general organization of this dissertation will consist of:
1) a discussion of the theory as it relates to deformed nuclei;
2) experimental determinations for each nucleus; and 3) a discussion of the results and how the data fit to the band systematics and structure of the region.

CHAPTER II

THEORETICAL REFLECTIONS

2.1 Introduction

A better understanding of nuclear structure requires appropriate

mathematical treatments of a simplified mechanical system. Therefore,

our concept of the nucleus evolves as the properties of different

models emphasize many of the characteristics of the nucleus [In69].

In the mid-1930's N. Bohr compared the nucleus to a liquid drop

[Bo36], giving rise to the idea that collective types of motion would

correspond to fundamental modes of excitation. An apparently contra-

dictory approach introduced by M. Mayer [Ma49] and others [Ha49] was

the nuclear shell model (for several previous attempts concerning the

shell model approach, see [Be36], [Be37], and [Li37]) that brought the

idea that nuclear orbitals could be described in terms of the motions

of individual nucleons in an average force field (this potential

represents the interaction force between a nucleon and all others

collectively within the nuclear volume).

These two models approached different characteristics of nuclear

structure and dynamics, namely, nucleonic collectivity and

individuality, but J. Rainwater [Ra50] was able to combine these two

ideas by suggesting that a nonspherical nuclear shape would arise from the single-particle motion in anisotropic orbitals by including the nuclear deformation as in the liquid-drop model. The mathematical treatment of this unified model was given by A. Bohr and B. Mottelson [Bo52], [Bo53], who were then able to explain simple rotational spectra and many collective properties of the nucleus. With this unified model as a starting point, S. Nilsson [Ni55] set out to describe the behavior of the intrinsic (nucleonic) states under increased deformation of the nuclear potential, and the single-nucleon orbitals obtained, along with some refinements [Gu67], are widely used today in classifying intrinsic spectra.

At about the same time, D. Inglis [In54] suggested that the nuclear moment of inertia could be taken as the summation of the inertial effect of each particle in a rotating deformed potential, therefore giving the appearance that the potential is externally "cranked". A few years later, Thouless and Valatin [Th62] further enhanced this idea by using time-dependent Hartree-Fock equations to obtain an approximation of the self-consistent behavior of a many-body system. Therefore, particle motion could be thought of in terms of a rotating frame of reference (time-dependent), as opposed to a stationary frame of reference (time-independent). Although this self-consistent cranking shell model, also called Hartree-Fock-Bogoljubov Cranking Shell Model (HFBC model), includes the pairing effect (the effect of coupling particles with resulting zero angular momentum), these calculations are very difficult and time-consuming [Che].

In the mid-1970's, with a wealth of new information about the high-spin states in a wide mass region, it became evident that rotational spectra could be understood in terms of configurations of quasiparticles (a mixture of particles and holes; a more detailed description can be found in Chapter II, Section 3.2) in a rotating potential [Be77], giving origin to a simplified Cranking Shell Model [Be79b]. These simplifications are mainly concerned with realistic values for nuclear shape and nucleon pairing.

The Cranking Shell Model has been successfully applied in the rare-earth region [Ri80] and is just beginning to be tested in the region far from β-stability [Nol].

2.2 The Deformed Shell Model

The Hamiltonian for an ensemble of nucleons moving in a deformed potential can be written as

$$H = H_{intr}(q,p) + H_{rot,\alpha}(P_\omega) , \qquad (2.2.1)$$

which corresponds to intrinsic and collective motions. It also indicates that these two types of motions are separable [Bo75]. The intrinsic motion can be described by the body-fixed coordinates q and conjugate momenta p, while the rotational Hamiltonian depends on the conjugate angular momenta P_ω (ω is the angular variable) and may depend on the intrinsic state quantum number α.

For the case of a particle strongly coupled to a rotating core, Equation (2.2.1) can be rearranged to(variables are omitted):

$$H = H_{col} + H_{coup} + H_{int} \qquad (2.2.2)$$

where the first and last terms refer to collective and individual particle (intrinsic) motions, respectively, while the second term (coupling) contains the interaction between the particle and rotational motions. The collective Hamiltonian can be described as

$$H_{col} = \frac{\hbar^2}{2\mathcal{J}} (\hat{I}^2 - \langle \hat{I}^2 \rangle) , \qquad (2.2.3)$$

and the coupling Hamiltonian as

$$H_{coup} = \frac{-\hbar^2}{2\mathcal{J}} (\hat{I}_+ \hat{j}_- + \hat{I}_- \hat{j}_+). \qquad (2.2.4)$$

The moment of inertia of the nucleus is defined by $\mathcal{J}$ while I is the total angular momentum operator. The intrinsic Hamiltonian, i.e., the Nilsson Hamiltonian, yields

$$H_{int} = H_0 + 2\kappa\hbar\omega[\hat{\ell}\cdot\hat{s} - \mu(\hat{\ell}^2 - \langle \hat{\ell}^2 \rangle)] , \qquad (2.2.5)$$

where H_0 is the deformed harmonic oscillator [Ni55] such that, at zero deformation, it corresponds to a spherical harmonic oscillator. The potential parameters κ and μ are obtained by empirically adjusting H_{int} to the available data on the intrinsic spectra of the deformed nuclei [Bo75]. The $\hat{\ell}^2$ term splits the degeneracy in each major oscillator shell (N) by favoring large ℓ values; therefore, in the N=6 shell, the 1i-subshell is energetically favored over the 2g-subshell. The $\hat{\ell}\cdot\hat{s}$ term further splits the subshell into $j=\ell\pm s$ degenerate orbits; hence, the 1i-subshell is separated into $1i_{11/2}$ and $1i_{13/2}$

orbits. With increased deformation, the orbits (like $1i_{13/2}$) display a degeneracy of $(2j+1)/2$ orbitals. For a nucleon in an orbital, the projection of its angular momentum on the symmetry axis of the nucleus can have the values $\Omega=j,j-1,\ldots,1/2$. For prolate deformation, the low Ω-values are energetically favored. The $\langle\hat{\ell}^2\rangle$ term is a constant for each (spherical) oscillator shell so that the average energy difference between the oscillator shells is not affected by the $\hat{\ell}^2$ term.

The eigenstate of the Hamiltonian is a product wave function of the type

$$\psi_{\alpha IKM} = \varphi_\alpha(q)\ \phi_{\alpha IKM}(\omega), \tag{2.2.6}$$

where, for each intrinsic state α, a sequence of rotational levels arise.

The rotational wave function can be further normalized in the body-fixed coordinates (intrinsic coordinates) specified by the three angular momentum quantum numbers I (total angular momentum), M (projection of I on a space-fixed axis), and K (total angular momentum projection on the symmetry axis):

$$\phi_{IKM}(\omega) = \left(\frac{2I+1}{8\pi^2}\right)^{1/2} \mathscr{D}^I_{MK}(\omega) , \tag{2.2.7}$$

where $\mathscr{D}^I_{MK}$ are the rotation matrices [Bo75].

The intrinsic Hamiltonian must be invariant with respect to a 180° rotation about the x axis;

$$\mathscr{R}_x \, \psi_{IKM} \, \mathscr{R}_x^{-1} = \psi_{IKM} \, . \qquad (2.2.8)$$

The final product wave function is [Bo69];

$$\psi_{IKM} = \left(\frac{2I+1}{16\pi^2}\right)^{1/2} \left[\varphi_K(q)\mathscr{D}^I_{MK}(\omega) + (-1)^{I+K} \varphi_{\overline{K}}(q)\mathscr{D}^I_{M\overline{K}}(\omega) \right], \qquad (2.2.9)$$

where $\overline{K}$ implies negative values of K (time-reversed orbits).

By using the intrinsic Hamiltonian, H_{int}, on the product wave function, a set of eigenstates having energies which are dependent on the nuclear deformation can be determined. Each eigenstate (Nilsson level) is labelled with the $\Omega[Nn_z\Lambda]$ quantum numbers where Ω is the intrinsic angular momentum projection on the symmetry axis. Along the symmetry axis, the label n_z represents the number of nodal planes, and Λ is the projection of the intrinsic orbital angular momentum. A Nilsson level diagram is shown in Figure 2.1 for neutron and proton single-particle deformed orbitals at $\varepsilon_2 = 0.255$ and $\varepsilon_4 = 0.110$ deformation(calculated according to the Strutinsky method [Ni69] and the systematics of the mass region).

The collective Hamiltonian, H_{col}, yields the rotational band energies,

$$E_{rot} = \frac{\hbar^2}{2\mathfrak{J}} [I(I+1)-K^2] , \qquad (2.2.10)$$

and the coupling Hamiltonian, H_{coup}, yields

$$E_{coup} = \frac{\hbar^2}{2\mathfrak{J}} [(I\mp K_1)(I\pm K_1+1)]^{1/2}[(j\pm\Omega_1)(j\mp\Omega_1+1)]^{1/2} \, \delta_{K_1,K_2\pm1}\delta_{\Omega_1,\Omega_2\pm1}f \qquad (2.2.11)$$

where f is a pairing reduction factor.
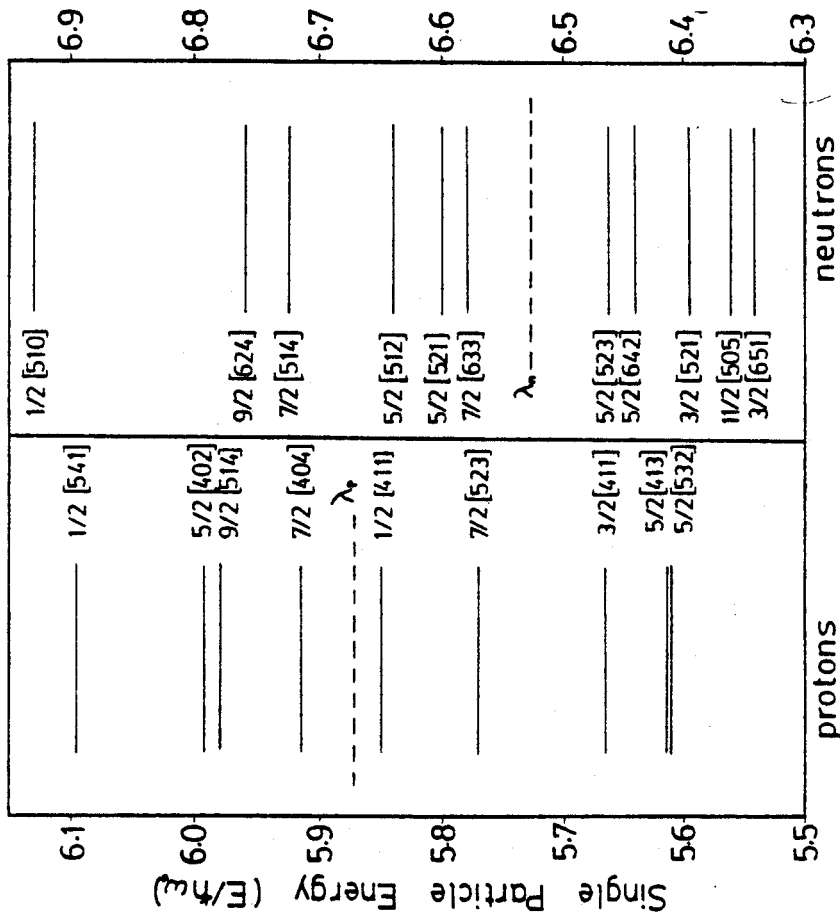
Figure 2.1 Nilsson level diagram for ^{168}Yb using $\epsilon_2=0.255$ and $\epsilon_2=0.11$.

2.3 The Cranking Shell Model

2.3.1 The Cranking Shell Model Hamiltonian

In the cranking model [In54] the average nuclear potential is considered to rotate at a constant frequency, ω, about the x axis (rotational axis). It was suggested again [Bo77], [Be77] in 1977 that it was possible to calculate excitation eigenvalues (excited states in the rotational spectrum) through the appropriate cranking Hamiltonian by including a frequency dependence:

$$H' = H - \omega \hat{J}_x , \qquad (2.3.1)$$

where H is the deformed shell model Hamiltonian and $\hat{J}_x$ yields the total angular momentum projection on the rotational axis. H' is also called the Routhian Hamiltonian, since it refers classically [Ro05] to the rotating frame of reference.

In the analysis, the transformation from the body-fixed to rotating frame of reference allows us to calculate excitation energies (relative to the ground state) involved with valence particles and holes. This leads to the discussion of the concept of quasiparticles.

2.3.2 Pairing Correlations and Quasiparticles

The description of pairing correlations in a superconductor by Bardeen, Cooper and Schreiffer [Ba57a], [Ba57b] can be used for other many-body correlations. As pointed out by Migdal [Mi59] and Belyaev

[Be59], the nuclear pairing effect can be treated in the context of the BCS domain.

In this model, a pair of nucleons in time-reversed deformed orbits interacts with each other through the pairing force. In considering the valence nucleons, the resulting ground state of the nucleus is lowered in energy due to such pairing force. Also, the excited states may be characterized as a mixture of unoccupied orbits (holes) and occupied orbits (particles). One may refer collectively to the holes and particles as quasiparticles, and the related excitation as the quasiparticle excitation [Bo69]. Then, the ground state of an even-even nucleus may be thought of as a zero-quasiparticle state or the quasiparticle vacuum, and the low-lying states of odd-A nuclei as single quasiparticle states.

2.3.3 The Quasiparticle Hamiltonian and Its Eigenvalue Equation

The importance of pairing correlations leads to a Hartree-Fock-Bogoljubov (HFB) approach to the Routhian Hamiltonian H' (the HFB cranking approach), where quasi-particle equations in the rotating system are obtained. Therefore, the quasiparticle HFBC Routhian Hamiltonian can be written as:

$$h'_{q.p.} = h'_{s.p.} + \Delta(\hat{P}^{\dagger} + \hat{P}) - \lambda \hat{N} \qquad (2.3.2)$$

where the single-particle Routhian Hamiltonian [Ne76] is

$$h'_{s.p.} = h_{s.p.}(\epsilon) - \omega \hat{j}_x \quad . \qquad (2.3.3)$$

The single-particle Hamiltonian, $h_{s.p.}(\varepsilon)$, is the modified harmonic oscillator [An76] with a dependence on the deformation parameter $(\varepsilon_2, \varepsilon_4)$, and $\hat{j}_x$ operation yields the single-particle angular momentum projection on the x axis.

The $\hat{p}^\dagger$ and $\hat{p}$ terms are the annhilation and creation operators for the pair field, and Δ is the gap parameter relating paired and unpaired ground states. The λ term is a Lagrange multiplier (also called the chemical potential or Fermi surface), and N is the particle number.

A more convenient representation of $h'_{q.p.}$ can be obtained by expanding the terms of Equation (2.3.2) into

$$h'_{q.p.} = \sum_{\alpha i i'} [(e_i - \lambda)\delta_{i i'} - \omega \hat{j}_{x_{i\alpha,i'\alpha}}]\hat{c}^\dagger_{i\alpha}\hat{c}_{i'\alpha} + (1/2)\Delta \sum_{i\alpha} (\hat{c}^\dagger_{i\alpha}\hat{c}^\dagger_{i\alpha} + \hat{c}_{\overline{i\alpha}}\hat{c}_{\overline{i\alpha}}) ,$$

$$(2.3.4)$$

where the particle motion in the cranked (deformed) potential is described in the first term while the second term describes the scattering of particles into holes and vice versa (quasiparticles) under the pairing field [Fr81a]. The term e_i stands for the single-particle energy, while the $\hat{c}^\dagger$ and $\hat{c}$ represent the quasiparticle creation and annhilation operators. The label i stands for a set of particle quantum numbers $(n\rho j)$ and $\overline{i\alpha}$ indicates time-reversed $i\alpha$. The label α is a symmetry quantum number that depends on the particle number (it is also called the signature of the quasiparticle state).

A state wave function of the Bardeen, Cooper and Schrieffer (BCS) type can be used to describe the lowest-energy quasiparticle state as well as other states. The wave function $|$ BCS$>$ does not describe a state with a fixed number of nucleons but rather it is an admixture of states with different numbers of nucleons. This is achieved by assuming that the pair state $(\mu\alpha, \overline{\mu\alpha})$ is occupied with probability $V^2_{\mu\alpha}$, and is empty with probability $U^2_{\mu\alpha}$. To find this energy minimum, the mean particle number has to be equal to N, namely,

$$<BCS \mid \hat{N} \mid BCS> = N \quad \text{where} \quad \hat{N} = \sum_{i\alpha} \hat{c}^{\dagger}_{i\alpha} \hat{c}_{i\alpha} \ .$$

Therefore, by adjusting $V_{\mu\alpha}$ and $U_{\mu\alpha}$, the expectation value of $<BCS \mid h'_{q.p.} \mid BCS>$ is minimized.

In introducing the quasiparticle operators (Bogoljubov transformation),

$$\hat{b}^{\dagger}_{\mu\alpha} = \sum_i (U^{\mu}_{i\alpha} \hat{c}^{\dagger}_{i\alpha} + V^{\mu}_{i\alpha} \hat{c}_{i\alpha}) \ , \tag{2.3.5}$$

$h'_{q.p}$ becomes diagonalized, and Equation (2.3.4) is simplified to

$$h'_{q.p.} = (1/2) \sum_{\mu\alpha} E'_{\mu\alpha} \hat{b}^{\dagger}_{\mu\alpha} \hat{b}_{\mu\alpha} + (1/2) \sum_{i\alpha} (\epsilon_i - \lambda - \omega \hat{j}_{x_{i\alpha,i\alpha}}), \tag{2.3.6}$$

representing a system of independent quasiparticles. Note that the Bogoljubov transformation is unitary. The set of operators $\hat{b}_{\mu\alpha}$ has twice the dimension of the single-particle space. Therefore, a new set of quasiparticle operators, $\hat{a}_{\nu\alpha}$, is restricted to the appropriate dimension. These new operators obey the commutation relations.

The quasiparticle vacuum can now be defined by

$$\hat{a}_{\nu\alpha} \mid BCS >_{vac} = 0 \qquad\qquad (2.3.7)$$

Any other state is an excitation with respect to the quasiparticle vacuum and can be described by the operators $\hat{a}^{\dagger}_{\nu\alpha}$. Then the quasiparticle Routhian Hamiltonian, Equation (2.3.6), can be further transformed to

$$h'_{q.p.} = \sum_{\nu\alpha} E'_{\nu\alpha}\hat{a}^{\dagger}_{\nu\alpha}\hat{a}_{\nu\alpha} + \sum_{\nu\alpha}(\epsilon_i - \lambda - \omega\hat{j}_{x_{i\alpha},i\alpha}) - (1/2)\sum_{\nu\alpha} E'_{\nu\alpha} \cdot \qquad (2.3.8)$$

The last term is a constant that describes a reference state like the quasiparticle vacuum (the ground state). The quasiparticle spectrum is built by states of the type

$$\hat{a}^{\dagger}_{\nu\alpha} \mid BCS>_{vac}, \quad \hat{a}^{\dagger}_{\nu\alpha}\hat{a}^{\dagger}_{\nu'\alpha} \mid BCS>_{vac}, \quad \ldots,$$

also called one-, two-, ... quasiparticle states. Accordingly, the energy of a quasiparticle configuration will be the sum of the individual quasiparticle energies. The lowest eigenstate of $h'_{q.p.}$ corresponds to an yrast[1] state and the yrast line is the sequence of these yrast states with increasing ω.

By using Equation (2.3.6) accordingly, some of the parameters described above can be explicitly evaluated [Og71], [Pr75]:

$$\left.\begin{array}{c} U^2_{i\alpha} \\ V^2_{i\alpha} \end{array}\right\} = (1/2)\ (1 \pm \frac{\epsilon_{s.p.} - \lambda}{E'_{q.p.}}) \qquad (2.3.9)$$

---

[1] An yrast state of a nucleus is the level of least energy at a given angular momentum; Grover [Gr67] suggested the term because there is no graceful English language equivalent in expressing the adjective for rotation in its superlative form. The original Swedish adjective is "yr", meaning "dizzy", and its superlative "yrast" can be literally translated as "dizziest".

where $\quad E'_{q.p.} = [(\varepsilon_{s.p.} - \lambda)^2 + \Delta^2)]^{1/2}$, $\qquad$ (2.3.10)

and Δ can be calculated as a first approximation by [Ni69]

$$\Delta = \frac{12}{A^{1/2}} \text{ MeV} \qquad (2.3.11)$$

Also, the systematic mass difference between even and odd neighboring isotopes (associated with the pairing field) can be used to calculate Δ [Bo75]. The mean number of particles, N, can be calculated by

$$N = \sum_{ii'} (1 - \frac{\varepsilon_{s.p.} - \lambda}{E'_{q.p.}}) \; . \qquad (2.3.12)$$

The above calculations are time-consuming and long, since most of them have to be repeated for different ω, hence, computer codes are used as described in the next section.

2.3.4 Important Quantities and Properties

In order to better understand the important quantities and properties associated with the Cranking Shell (CS) model, a quasiparticle Routhian diagram is drawn in Figure 2.2 for ^{168}Yb. The quasiparticle Routhians were calculated by solving the quasiparticle equations discussed in the previous section. A computer code, referred to here as the "CSM Code" [CS78] was used to obtain numerical solutions for the quasiparticle Routhians, e', as a function of $\hbar\omega$. Also included in the figure are the Nilsson quantum numbers [Ni55] at $\hbar\omega = 0$ MeV as additional labels. The $\varepsilon_2, \varepsilon_4$ deformation parameters were calculated
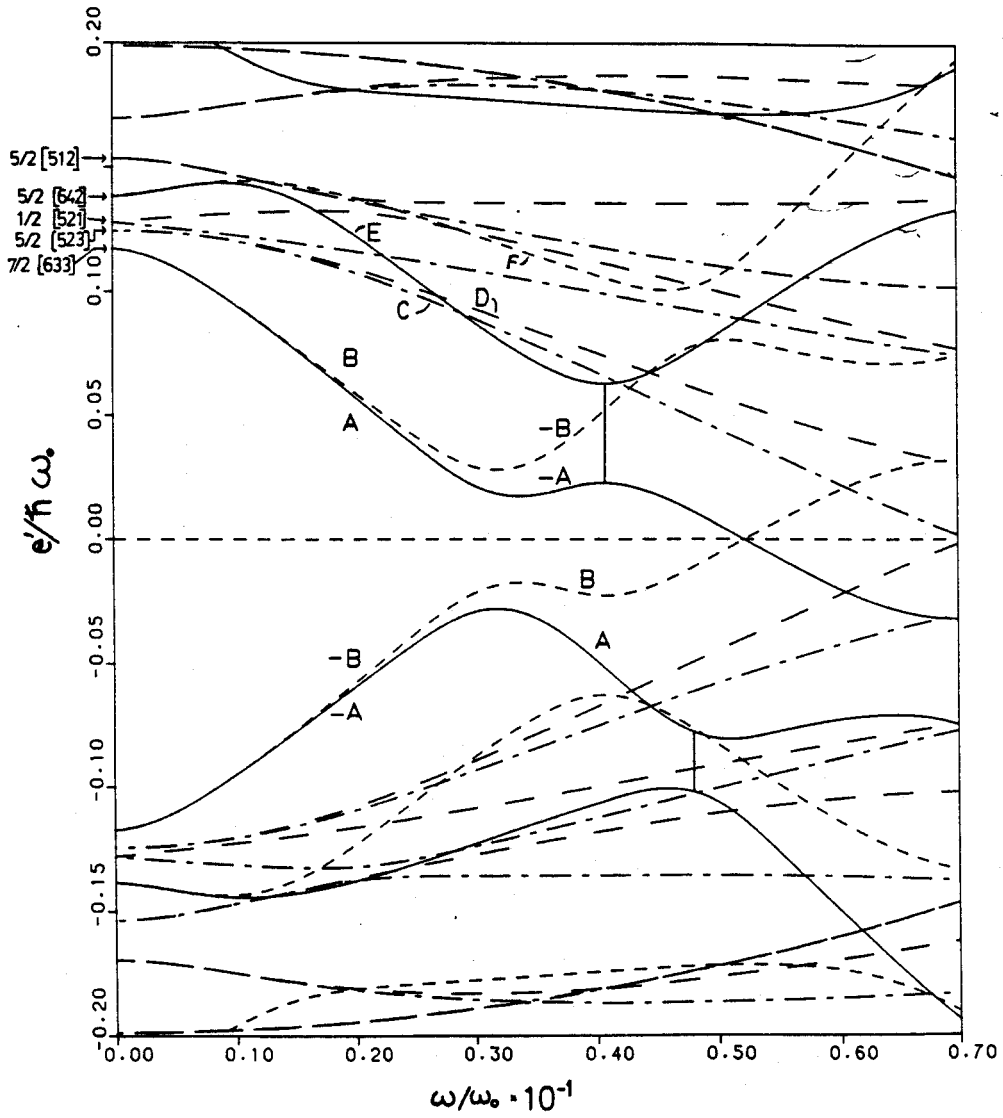
Figure 2.2 Theoretical Routhian e' versus ħω diagram for [168]Yb.

according to the Strutinsky method [Ni69], and are the ones used [CS78] in systematic calculations throughout the region.

In Figure 2.2, the quasiparticle energies and frequencies are in units of $\hbar\omega_0$ ($\hbar\omega_0 = 41/A^{1/3}$ MeV) and the following convention is used for the quasiparticle orbits:

$$\underline{\alpha^\pi}$$

solid lines: $+1/2^+$

small dashed lines: $-1/2^+$

long dashed lines: $-1/2^-$

dashed-dotted lines: $+1/2^-$.

The important quantities in this model are discussed below:

i) The signature, α:

The Hamiltonian Routhian h' is assumed to be invariant with a 180° rotation around the x axis (see Equation 2.2.8):

$$\mathscr{R}_x \, h' \, \mathscr{R}_x^{-1} = h' \, , \qquad (2.3.13)$$

where
$$\mathscr{R}_x = e^{-i\pi j_x} \, . \qquad (2.3.14)$$

The rotation symmetry is therefore applicable to the quasiparticle states $| \nu\alpha \rangle$:

$$\mathscr{R}_x | \nu\alpha \rangle = e^{-i\pi\alpha} | \nu\alpha \rangle \, , \qquad (2.3.15)$$

with values of $\pm 1/2$ for α, the signature.

ii) The parity, π:

Assuming that the deformed potential is axially symmetric around the x axis, then

$$\mathscr{P} h' \mathscr{P}^{-1} = h' . \qquad (2.3.16)$$

This relation implies that the potential is invariant to the space inversion, $\mathscr{P}$, and that the parity, π, is a good quantum number with values of + or - [Go74], [Fr81a].

iii) The (relative) aligned angular momentum, i:

For an even-even nucleus (like ^{168}Yb and ^{128}Ce), the increase of rotation will cause paired valence nucleons in time-reversed orbits to uncouple and to align their angular momenta along the rotational axis (Coriolis Anti-Pairing Effect). This excited state will have a corresponding gain in alignment, that is

$$\frac{-dE'_{\nu\alpha}}{d\omega} = \langle j_x \rangle , \qquad (2.3.17)$$

where $\langle j_x \rangle$ is the angular momentum "aligned" along the x-axis.

In keeping ω fixed in the calculations, the constraint

$$\langle j_x \rangle = I_x \qquad (2.3.18)$$

is fulfilled [Be79a]. By using a reference state (such as the quasi-particle vaccum), the (relative) aligned angular momentum, i, will be

$$i(\omega) = I_x(\omega) - I_{x,ref}(\omega) . \qquad (2.3.19)$$

The gain in alignment for an excited state composed of several quasiparticles can now be simply stated as to be equal to the sum of the individual valence's angular momentum.

Some important properties are:

i) Additivity:

By using a reference state like the quasiparticle vacuum, all quasiparticle quantities are additive, e.g., excitation energy, angular momentum and signature.

ii) Conjugate orbits:

If a quasiparticle orbit is occupied, its conjugate partner is unoccupied. This is pointed out pictorially in Figure 2.2 as the orbits -A and A, respectively.

iii) The reference configuration:

In order to use relative quantities, a reference configuration is needed. The reference configuration, also called the g-configuration if the ground state is used, corresponds (in Figure 2.2) to having all levels below zero occupied at low ω, and therefore the vacuum and g-configurations are identical [Be79a].

iv) The parity of an excited configuration is the product of the parities of the quasiparticle configurations involved in the excitation. Also, the g-configuration of an even-even nucleus has $\pi = +$, a property of the parity operator [Fr81b].

2.3.5 The Experimental Routhians and Related Quantities

One of the keys of the CS model is the additivity of energy and other quantities for the excited states in the quasiparticle spectrum; namely, a certain quasiparticle excitation (and the rotational band

based on it) is obtained by adding up the contributions of the different quasiparticles involved. For example, a two-quasiparticle state is formed by adding two single-quasiparticle states.

In order to calculate the experimental Routhians, the rotational frequency, ω, is determined by the canonical relation [Fr81b]:

$$\omega_x = \frac{dE(I)}{dI_x} \, , \qquad (2.3.20)$$

which is approximated by ($\omega_x = \omega$ is used for simplicity),

$$\omega(I) = \frac{E(I+1)-E(I-1)}{I_x(I+1)-I_x(I-1)} \, . \qquad (2.3.21)$$

The I_x represents the total angular momentum projection on the x axis. Therefore, the expectation value of $\hat{I}_x^2$ will be:

$$\langle \hat{I}_x^2 \rangle = I(I+1) - K^2 \qquad (2.2.22)$$

and

$$\langle \hat{I}_x^2 \rangle = I_x^2 \, . \qquad (2.3.23)$$

Since physical nuclear rotors are three-dimensional [Bo77], the magnitude of the total angular momentum can be approximated, through a Taylor series expansion, to the following

$$[I(I+1)]^{1/2} \simeq (I+1/2) \text{ for large } I. \qquad (2.3.24)$$

Substituting Equations (2.3.24) and (2.3.22) into (2.3.23), we have:

$$I_x = [(I+1/2)^2 - K^2]^{1/2} \, . \qquad (2.3.25)$$

Since only $\Delta I = 2$ transitions are considered due to symmetry properties (signatures), a more precise definition of $\omega(I)$ is prescribed as an average value of the two frequencies related to the levels I+1 and I-1. Graphically, $\omega(I)$ is an interpolation between the discrete values of $\omega(I+1)$ and $\omega(I-1)$.

As pointed out previously, one of the keys of the CS model is its additivity property; thus, an excitation configuration is related to a g-configuration (or quasiparticle vacuum). The angular momentum of an excited band is referred to the g-configuration as

$$i(\omega) = I_x(\omega) - I_{xg}(\omega) , \qquad (2.3.26)$$

where I_{xg} is the core's angular momentum (also called R). Then one must find the reference $I_{xg}(\omega)$. Because the g-configuration changes since there is a gradual destruction of pairing among all members with increasing rotation, a variable moment of inertia (VMI) approach [Ma69] is used as a reference instead:

$$I_{xg}(\omega) = \Im \omega \qquad (2.3.27)$$

or

$$I_{xg}(\omega) = (\Im_0 + \Im_1 \omega^2)\omega . \qquad (2.3.28)$$

After rearranging and taking the derivative in relation to the frequency,

$$\frac{dI_{xg}(\omega)}{d\omega} = \Im_0 + 3\Im_1\omega^2 . \qquad (2.3.29)$$

Equations (2.3.28) and (2.3.27) are equal if the nucleus behaves like a rigid rotor but usually it does not. Therefore, one must estimate

$\mathfrak{J}$ (Equation 2.3.27) in the best way possible using an appropriate reference configuration which can be the g-configuration or the s-configuration (the s-band is an aligned quasiparticle band that crosses the ground state band and becomes the continuation of the yrast band). Experimentally, a reasonable estimate of the moment of inertia for a g- or s-band is obtained by

$$\frac{\Delta I_x}{\Delta \omega} = \mathfrak{J}_0 + 3 \mathfrak{J}_1 \omega^2 \quad , \qquad (2.3.30)$$

from two consecutive $\Delta I = 2$ transitions . For the g-band, I_x/ω can also be used because it will give the same $\mathfrak{J}_0$ and $\mathfrak{J}_1$ as in Equation (2.3.30). Because ω is an interpolation, as pointed out in Equation (2.3.21), one way to extract ω^2 more accurately is by using:

$$\omega^2 = \frac{1}{4} [\omega(I) + \omega(I-2)]^2 \quad . \qquad (2.3.31)$$

Finally, the eigenvalues for the Routhian Hamiltonian, also called the Routhians, are defined as

$$e'(\omega) = E'(\omega) - E'_g(\omega) \quad , \qquad (2.3.32)$$

where, experimentally,

$$E'(\omega) = \frac{1}{2} [E(I+1) + E(I-1)] - \omega I_x \qquad (2.3.33)$$

and

$$E'_g(\omega) = - \int I_{xg}(\omega)d\omega = -\frac{1}{2} (\mathfrak{J}_0\omega^2) - \frac{1}{4} (\mathfrak{J}_1\omega^4) + (\hbar^2/8\mathfrak{J}_0). \qquad (2.3.34)$$

The information obtained from using the above equations is discussed in the next section.

2.3.6 Interaction and Crossing of Bands

Discontinuity in the smooth trend of rotational spectra with increasing angular momentum has been termed "backbending" [Jo72] due to the fact that, in the graphical representation of $2\mathfrak{J}/\hbar^2$ (moment of inertia) vs. $\hbar^2\omega^2$, a bending backwards of the plotted curve is seen. In Figure 2.3 the backbending effect is observed to occur between spins 12^+ and 14^+ for ^{160}Yb [Ri80].

In the rare-earth region this backbending phenomenon has been explained microscopically with a quasiparticle-plus-rotor model. That is, backbending occurs as a result of a crossing between a ground state rotational band and a quasiparticle band. Since the quasiparticle band has a larger aligned angular momentum, the yrast line displays a change in the effective moment of inertia. In this model, high-j quasiparticles are needed for effective band crossing at low frequencies, such as $i_{13/2}$ and $h_{9/2}$ quasineutrons and $h_{11/2}$ and $h_{9/2}$ quasiprotons.

The occurrence of the backbending effect is not common to all nuclides in the deformed regions. For example, consider the case of the N=98 isotones where there is a small upbend, as opposed to backbend, indicating that there is a crossing with large mixing between the ground state and the quasiparticle bands. Therefore, it is more appropriate phenomenologically to interpret backbending or no-backbending by the amount of interaction between two bands. For strong "backbenders", there is a small interaction, while for "non-backbenders", large interaction.
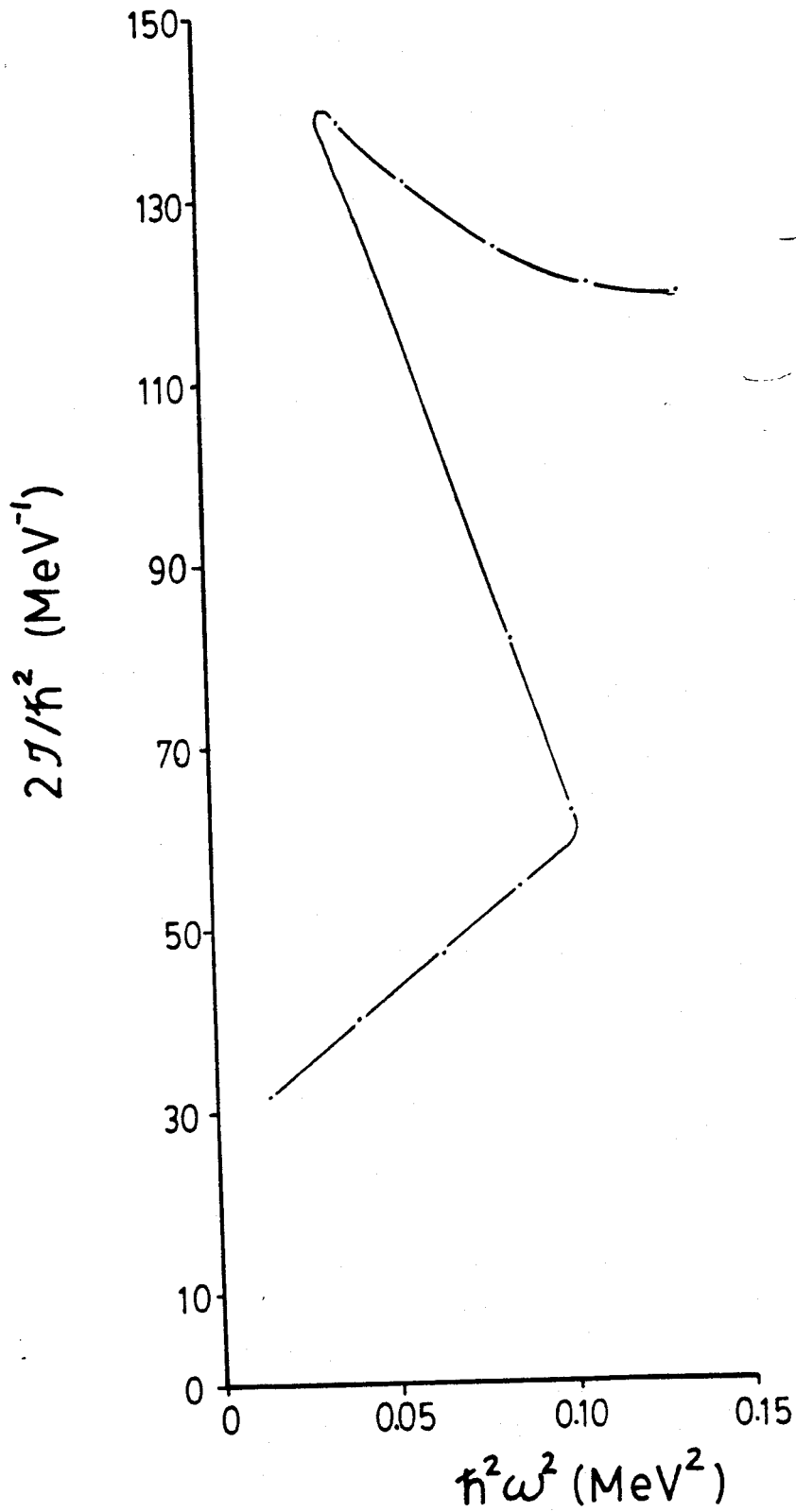
Figure 2.3   Backbending plot for ^{160}Yb.

In the cranking quasiparticle-plus-rotor approach, the valence nucleons form quasiparticle orbits that can interact to a greater or lesser extent. The magnitude of these interactions is measured by the $\Delta e'$ of closest proximity between the quasiparticle orbits, as noted out in Figure 2.2 by the vertical connecting lines. For large $\Delta e'$, an upbend behavior will be observed. For those small interactions that cause an unoccupied quasiparticle orbit to dip below $e'=0$ (see Figure 2.2), a sharp change in the rotational sequence of the band should occur (backbending). In a simplistic picture, a nucleon associated with a quasiparticle orbit slowly gains more alignment as the nucleus rotates faster until its excitation energy no longer allows it to stay in the same quasiparticle space; suddenly, it changes to a different, previously unoccupied orbit which has a certain amount of angular momentum alignment. In other words, there exist even at relatively low ω highly aligned two-quasiparticle bands, but they are not yrast. Only at ω_c (crossing frequency) does this two-quasiparticle band become yrast; i.e., the gain in energy due to the Coriolis alignment overcomes the loss in energy due to exciting the two-quasiparticle band. With the alignment gain in angular momentum, there is a corresponding change in moment of inertia, and, depending on the magnitude of $\Delta e'$, there will be backbending or not.

CHAPTER III

YTTERBIUM-168 EXPERIMENTAL DETERMINATIONS

3.1 Gamma-Gamma Coincidences

In order to obtain ^{168}Yb nuclei, oxide targets of enriched (98.5%) ^{166}Er were bombarded with 27-MeV alpha-particles producing the reaction ^{166}Er(α,2n)^{168}Yb. These oxide targets were made by weighing small amounts (1.0-1.5 mg) of the enriched erbium, mixing with distilled water, depositing them on a thin layer of Formvar and letting the targets dry overnight in a desiccator. The resulting targets were about 3 mg/cm^2 and were able to withstand up to two days of bombardment without breaking apart.

The Michigan State University (MSU) sector-focused isochronous cyclotron was used to produce the alpha-particle beams in the K=50 energy mode, and the RF signal was used for timing purposes. As a preliminary guideline, the optimum bombarding energy for different (α,xn) reaction channels was calculated theoretically by using the computer code CS8N [Sik]. Also, the systematics of the reactions to produce neighboring Yb isotopes was used. A qualitative measurement of the excitation functions was performed and the bombarding energy of 27 MeV was chosen to minimize contaminant γ rays. One prominent

interfering reaction channel was (α,n) and several γ rays coming from ^{169}Yb appeared in the singles spectrum. The beam current averaged about 3 nanoamperes.

The detectors used were a large-volume (90 cc) closed-end detector with 16 percent efficiency and a high-purity planar detector with a resolution of 650 eV FWHM at 122 keV. They were placed at 90° to the beam direction and as close as possible (8 cm) to the reaction chamber, as shown in Figure 3.1. The planar detector was especially useful in resolving low-energy γ rays between 80 and 300 keV. Thin foils of copper (0.1 mm thick) and lead (0.5 mm thick) were used in front of the detectors to reduce x rays coming mostly from the erbium target.

The deexcitation of ^{168}Yb nuclei causes a cascade of γ rays and those which are in coincidence were recorded on a magnetic tape as γ_1-γ_2-time using the computer program IIEVENT [Au72]. Some 18 million events were recorded and, in the off-line analysis, were sorted out by restricting two parameters using digital gates and projecting the third parameter either as energy or as time spectra. This sorting was done by the computer code KKRECOVERY [Mo75], where up to sixty 4096-channel spectra could be obtained in a single sorting. Total events spectra were obtained by placing a gate on the prompt peak of the TAC spectrum and an open gate on the energy spectrum of one of the solid-state detectors. The projected energy spectrum contains essentially all γ rays observed in the experiment, as shown in
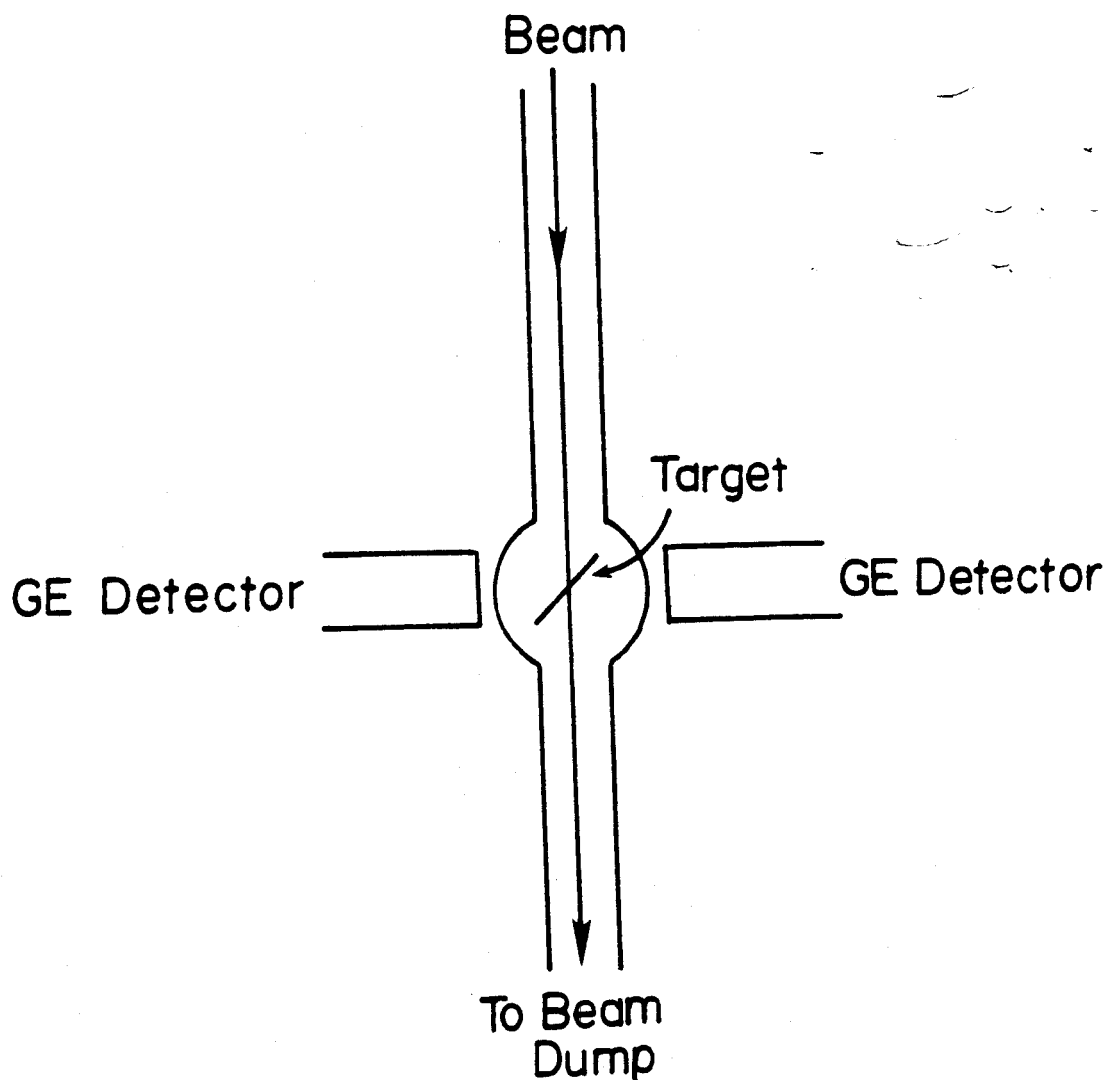
Figure 3.1   Experimental setup for the ^{166}Er(α,2n)^{168}Yb reaction.

Figure 3.2. From such a spectrum, it was possible, through repeated sortings, to make some 300 digital gates for both detectors. Some important gates are shown in Appendix A. Compton background subtraction was done by choosing low and high energy regions near the gated peak where there would be no peaks, and which therefore would be representative of the background in that section of the spectrum.

In order to make energy and intensity calibrations, a standard spectrum for each detector was taken during bombardment by measuring the γ rays emitted by ^{152}Eu and ^{133}Ba. Through internal comparison with the standard sources, the ^{168}Yb cascade γ rays were calibrated. To analyze these spectra efficiently, a computer code called SAMPO [Ro69] was used by first fitting the most intense standard γ-ray peaks with Gaussian curves and varying exponential tails. The resulting standard "shape" parameters were used to fit Gaussians to the γ-ray peaks on all gated spectra. This code was especially useful in resolving up to six neighboring peaks (approximate channels for the centroids are manually put in, and the code maximizes the fitting procedure through an algorithm that involves the "shape" parameters and the centroids). A list of all γ rays above 80 keV identified in this experiment is in Table 3.1. The energies and the relative intensities of the transitions, as well as the angular distribution coefficients and the transition assignments, are listed also and will be discussed in later sections.
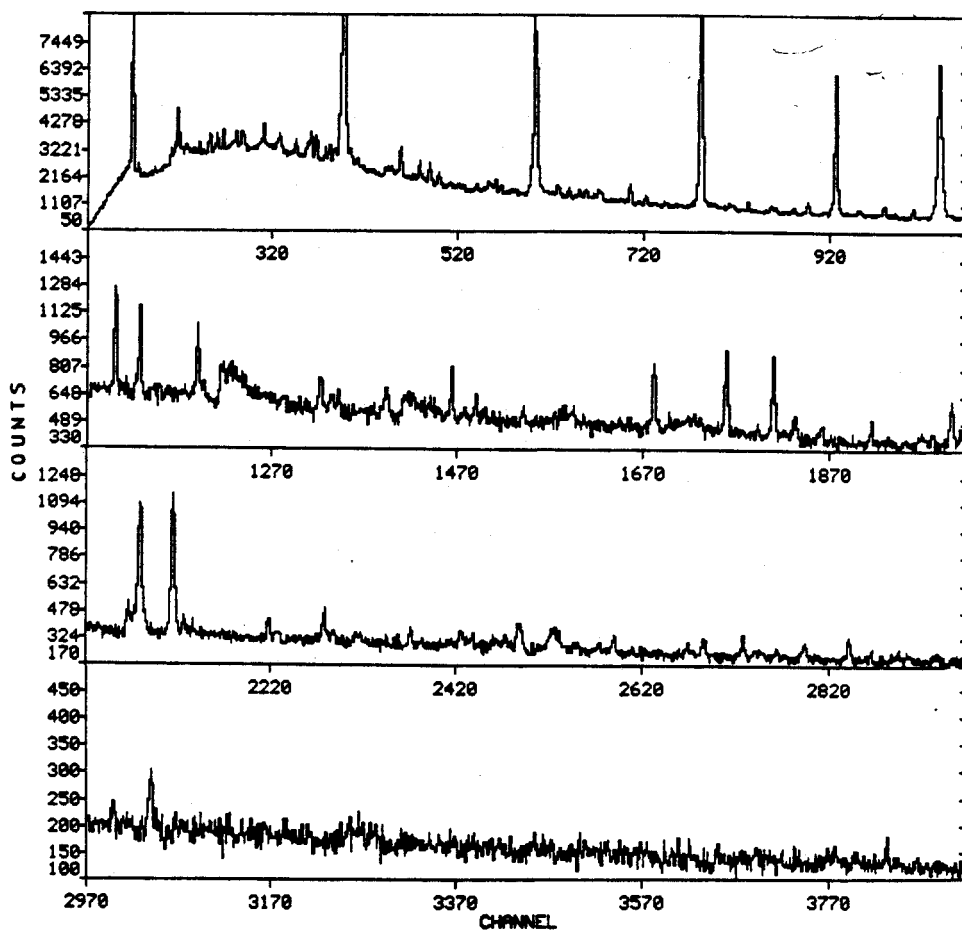
Figure 3.2   Projected total events spectrum for the large Ge(Li) detector in the ^{168}Yb coincidence experiment.

TABLE 3.1

Energies (E_γ), Intensities (I_γ), Angular Distribution Coefficients and Spin Assignments for Electromagnetic Transitions in ^{168}Yb

$E_\gamma{}^a$ (keV)	I_γ (rel. int.)	Angular Distribution Coefficient^b			Assignment^h
		A_2/A_0	A_4/A_0		
83.2^c					$3^+_\gamma \rightarrow 2^+_\gamma$
87.8	134.2(2.7)	0.11(4)	$-0.036(6)$	E2	$2^+_g \rightarrow 0^+_g$
99.6^c		0.46(12)		M1,E2	$4^+3 \rightarrow 3^+3$
111.5	31.9(2.2)	$-0.76(5)$	0.12(9)	M1,E2	$6^-5 \rightarrow 5^-5$
112.4	10.0(2.1)	0.54(16)	$-0.32(42)$	E2	$[(2222) \rightarrow 6^-5]$
123.0	5.7(7)	0.33(6)	$-0.083(93)$	M1,E2	$5^+3 \rightarrow 4^+3$

TABLE 3.1 (cont'd.)

<div align="center">34</div>

E_γ[a] (keV)	I_γ (rel. int.)	Angular Distribution Coefficient[b]		Assignment[h]
		A_2/A_0	A_4/A_0	
128.5	14.6(7)	-0.84(7)	0.062(120)	M1,E2 $7^-_5 \to 6^-_5$
145.0 }d	6.0(1.2)			M1,E2 $6^+_3 \to 5^+_3$
145.9 }	7.7(1.3)	-0.63(16)	0.42(30)	$8^-_5 \to 7^-_5$
157.0	17.8(7)[e]			$[5^-_5 \to (5,6)^-(1842)]$
164.1 }	6.0(1.2)[f]			$9^-_5 \to 8^-_5$
166.0 }	6.7(1.2)[e,f]			$7^+_3 \to 6^+_3$
173.9[c]	11.9(7)			$8^+_\gamma \to 7^+_\gamma$
179.8[d] }	12.7(9)[f]			$5^-_5 \to 6^+_3$
181.9[d] }	21.5(8)[f]			$10^-_5 \to 9^-_5$

TABLE 3.1 (cont'd.)

$E_\gamma{}^a$ (keV)	I_γ (rel. int.)	Angular Distribution Coefficient[b]		Assignment[h]
		A_2/A_0	A_4/A_0	
184.4	19.8(9)^g	0.18(2)	−0.017(24)	E2
189.4^c				8$^+$3 → 7$^+$3
193.6		0.29(5)	−0.093(76)	E2
198.0^c				11$^-$5 → 10$^-$5
199.0	1000(10)	0.27(1)	−0.053(9)	E2 4^+_g → 2^+_g
200.7^{c,f}				10$^+_\gamma$ → 9$^+_\gamma$
206.0	3.7(7)	0.20(10)	0.074(160)	E2
209.9^c				9$^+_\gamma$ → 8$^+_\gamma$
222.7^e	4.9(1.2)			5$^+$3 → 3$^+$3

Table 3.1 (cont'd.)

E_γ[a] (keV)	I_γ (rel. int.)	Angular Distribution Coefficient[b]		Mult.	Assignment[h]
		A_2/A_0	A_4/A_0		
223.9[c,f]	6.7(1.2)				[(5,6)⁻(1842) → 7⁺_γ]
224.0[c,f]					[(2222) → 5⁻5]
228.7	22.6(1.3)	-0.055(30)	-0.024(41)	M1,E2	[5⁻5 → 5⁻(1771)]
240.1	16.6(1.0)	0.23(2)	-0.024(23)	E2	7⁻5 → 5⁻5
248.4	10.4(1.0)	0.25(5)	-0.130(60)	E2	
268.0	6.3(1.2)	0.18(8)	-0.034(92)	E2	6⁺3 → 4⁺3
274.3[d]	11.7(1.1)	-0.21(2)[e]	0.094(34)[e]		(8⁻5 → 6⁻5
274.6					6⁺_γ → 4⁺_γ
277.6	13.8(1.2)	0.21(7)	0.091(110)	E2	

Table 3.1 (cont'd.)

E_γ[a] (keV)	I_γ (rel. int.)	Angular Distribution Coefficient[b]		Assignment[h]
		A_2/A_0	A_4/A_0		
298.7	877.1(9.2)	0.34(13)[e]	-0.18(21)[e]	E2	$4^+_g \to 2^+_g$
309.9	9.8(2.4)	0.37(17)[f]	-0.10(24)[f]	E2	$9^-5 \to 7^-5$
311.0	8.7(1.7)	0.20(1)[f]	-0.047(2)[f]	E2	$7^+3 \to 5^+3$
316.4	12.0(7)	0.26(6)	-0.29(7)	E2	$7^+_\gamma \to 5^+_\gamma$
321.9	11.2(9)[g]	0.32(7)	-0.021(100)	E2	
325.3	12.6(8)	0.18(9)	0.024(130)	E2	
331.6	12.9(1.0)	0.38(6)	-0.025(80)	E2	

Table 3.1 (cont'd.)

E_γ [a] (keV)	I_γ (rel. int.)	Angular Distribution Coefficient [b]		Assignment [h]
		A_2/A_0	A_4/A_0	
345.6[d]				$10^-5 \to 8^-5$
347.9[c]	25.6(1.1)			$8^+_\gamma \to 6^+_\gamma$
348.1[c]				$(1650) \to 5^+_\gamma$
348.9[c]				$5^-5 \to (1650)$
383.4[c]				$9^+_\gamma \to 7^+_\gamma$
384.7	607.5(9.8)	0.43(2)	−0.20(3)	E2 $8^+_g \to 6^+_g$
384.8[c]				$3^+3 \to 3^+2$
401.0	6.4(9)	−0.16(11)	−0.24(12)	M1,E2 [$5^-5 \to (4,3)^-(1598)$]

Table 3.1 (cont'd.)

E_γ[a] (keV)	I_γ (rel. int.)	Angular Distribution Coefficient[b]		Assignment[h]
		A_2/A_0	A_4/A_0	
410.0	11.9(9)	0.33(1)	-0.024(6)	E2 $\quad 10^+_\gamma \rightarrow 8^+_\gamma$
440.3	20.4(1.0)	0.35(5)	-0.14(6)	E2 $\quad 11^+_\gamma \rightarrow 9^+_\gamma$
455.2	294.8(3.5)	0.35(2)	-0.10(3)	E2 $\quad 10^+_\gamma \rightarrow 8^+_\gamma$
481.2	22.8(1.1)	-0.16(5)	-0.056(69)	M1,E2
487.5	6.3(3)	0.31(1)	-0.068(24)	E2
(510.5)				$12^+_g \rightarrow 10^+_g$
539.9	40.8(1.2)	-0.22(2)	-0.015(34)	E1 $\quad [(5,6)^-(1842) \rightarrow 5^+_\gamma]$
552.7	32.0(1.4)	0.40(6)	-0.21(10)	E2 $\quad 14^+_g \rightarrow 12^+_g$

Table 3.1 (cont'd.)

$E_\gamma{}^a$ (keV)	I_γ (rel. int.)	Angular Distribution Coefficient[b]		Assignment[h]
		A_2/A_0	A_4/A_0	
583.4	30.0(1.4)	0.081(120)	0.07(8)	E2 $\quad$ [(1650) $\rightarrow$ 3^+_γ]
584.0[c]				[(2404) $\rightarrow$ 6^+3]
648.4	18.4(1.4)	0.06(27)		M1,E2 $\quad$ $7^+_\gamma \rightarrow 8^+_g$
716.8	24.0(1.2)	-0.050(40)	0.018(59)	M1,E2 $\quad$ $5^+_\gamma \rightarrow 6^+_g$
729.3	12.4(9)	-0.25(27)		[(2404) $\rightarrow$ 5^+3]
777.7[c]				$10^+_\gamma \rightarrow 10^+_g$
780.6	9.3(9)			$3^+_\gamma \rightarrow 4^+_g$
822.4	37.8(1.4)	-0.35(4)	-0.13(7)	M1,E2 $\quad$ $8^+_\gamma \rightarrow 8^+_g$
859.6	52.7(1.5)	-0.17(4)	-0.20(7)	M1,E2 $\quad$ $6^+_\gamma \rightarrow 6^+_g$

Table 3.1 (cont'd.)

41

E_γ[a] (keV)	I_γ (rel. int.)	Angular Distribution Coefficient[b]		Assignment[h]	
		A_2/A_0	A_4/A_0		
884.0	51.5(7)	-0.15(4)	-0.13(6)	M1,E2	$4^+_\gamma \rightarrow 4^+_g$
884.1[c]					$[(2310) \rightarrow 10^+_g]$
895.6	11.4(2)				$2^+_\gamma \rightarrow 2^+_g$
978.8	26.4(1.6)	-0.030(200)		M1,E2	$3^+_\gamma \rightarrow 2^+_g$
1012.9[c]					$[(1598) \rightarrow 6^+_g]$
1014.3[g]	95.7(5.2)	-0.059(43)	-0.51(7)	M1,E2	
1015.5		-0.025(190)		M1,E2	$5^+_\gamma \rightarrow 4^+_g$
1032.0	107.3(3.1)	-0.19(18)	0.22(24)	M1,E2	$9^+_\gamma \rightarrow 8^+_g$
1032.9					$7^+_\gamma \rightarrow 6^+_g$

Table 3.1 (cont'd.)

E_γ[a] (keV)	I_γ (rel. int.)	Angular Distribution Coefficient[b]		Assignment[h]
		A_2/A_0	A_4/A_0	
1082.8[c]	13.7(1.4)			$4^+_\gamma \rightarrow 2^+_g$
1112.0	24.1(1.4)			$[(2082) \rightarrow 8^+_g]$
1158.1	15.0(8)	0.40(16)	−0.41(26)	E2 $6^+_\gamma \rightarrow 4^+_g$
1185.3[c]	11.3(1.3)			$[5^-(1771) \rightarrow 6^+_g]$
1189.5	10.3(1.1)			$(2160) \rightarrow 8^+_g$
1206.3[c]		−0.40(29)		M1,E2 $8^+_\gamma \rightarrow 6^+_g$
1232.5[f,g]	17.8(1.6)	−0.30(1)	−0.58(2)	M1,E2 $10^+_\gamma \rightarrow 10^+_g$
1234.5	11.5(1.5)			$6^+_3 \rightarrow 6^+_g$
1265.2	15.5(1.4)	−0.21(31)		M1,E2 $4^+_3 \rightarrow 4^+_g$

Table 3.1 (cont'd.)

E_γ [a] (keV)	I_γ (rel. int.)	Angular Distribution Coefficient[b]		Assignment[h]
		A_2/A_0	A_4/A_0	
1309.5	15.9(1.6)	-0.13(17)		M1,E2
1364.5[c]	14.8(1.4)	-0.12(12)		M1,E2 $3^+_3 \rightarrow 2^+_g$
1385.6	23.2(1.5)	-0.028(82)		M1,E2 $5^+_3 \rightarrow 4^+_g$
1483.8	22.4(1.2)	-0.30(6)		E1 $[5^-(1771) \rightarrow 4^+_g]$

[a] The uncertainty in the energy calibration is 0.5 keV.
[b] For no A_4/A_0 listed, the angular distribution calculation was performed with $A_4/A_0 = 0$.
[c] Observed in gated spectrum.
[d] Doublet/multiplet better resolved using off-prompt spectra.
[e] Masked by ^{19}F, ^{27}Al, ^{169}Yb or oxide matrix contaminant line.
[f] Doublet/multiplet causing unreliable angular distribution results.
[g] ^{19}F, ^{27}Al, ^{169}Yb or oxide matrix contaminant line.
[h] For those levels without a spin and a parity assignment, the energy is given in parenthesis.

From these coincidence gates it was possible to construct most of the level scheme that is drawn in Figure 3.3. The $K^{\pi}=2^+$ band is strongly populated, and another band based on the $K^{\pi}=3^+$ bandhead was observed. One of the most interesting features of the level scheme is the $K^{\pi}=5^-$ isomer band. Since its intraband transitions are weak and low in energy, it is difficult to ascertain their existence from the coincidence gates alone. These transitions were better observed by making use of γ_1-γ_2-t spectra which will be discussed in the next section.

3.2 Gamma-Gamma-Time Spectra

One feature of the pulsed-beam experiment is its timing content and it can be useful in determining γ rays that are not prompt in the time limits imposed by the electronics and the detectors used. The time between each beam burst (0.5 ns wide) was 63.8 ± 0.2 ns, and an experimental timing resolution of 10 ns FWHM was obtained from the TAC spectrum (Figure 3.4). Pictorially, one can describe the two off-prompt regions of a TAC spectrum as either "early" or "delayed", that is, corresponding to the γ rays "growing" in or decaying out of the isomer, respectively. Therefore, by taking time-slices from the TAC spectrum and an open gate on one of the energy spectra, it is possible to see which γ rays are "growing" in or decaying out of an isomer as a function of time. Figure 3.5 shows the 111-, 112-, 128-, 146-, 164-, 182-, 198-, 224-, 240-, 274-, 310-, and 346-keV peaks growing in, and Figure 3.6 shows the 157-, 180-, 229-, 325-, 349, and 401-keV peaks
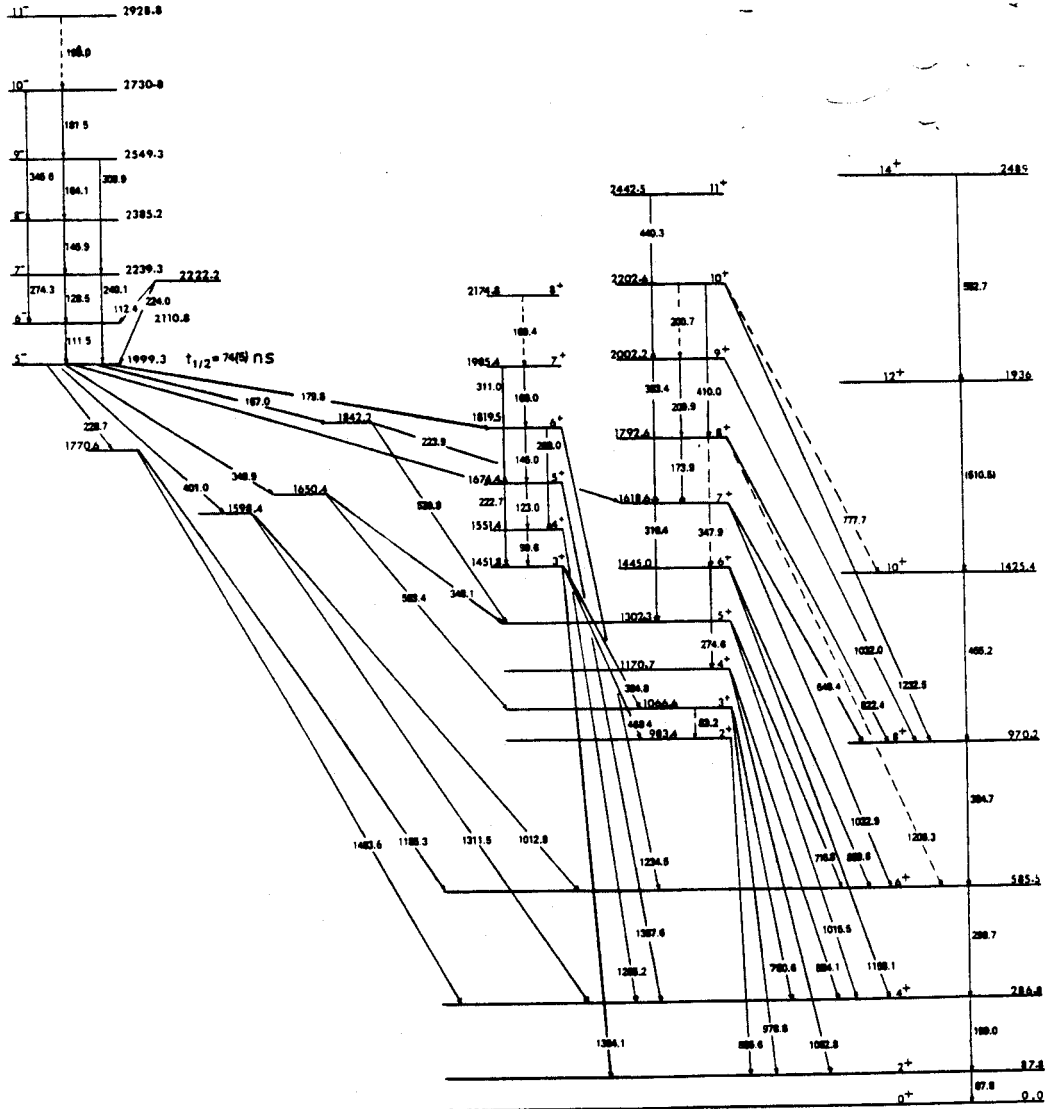
Figure 3.3 Level scheme for ^{168}Yb.
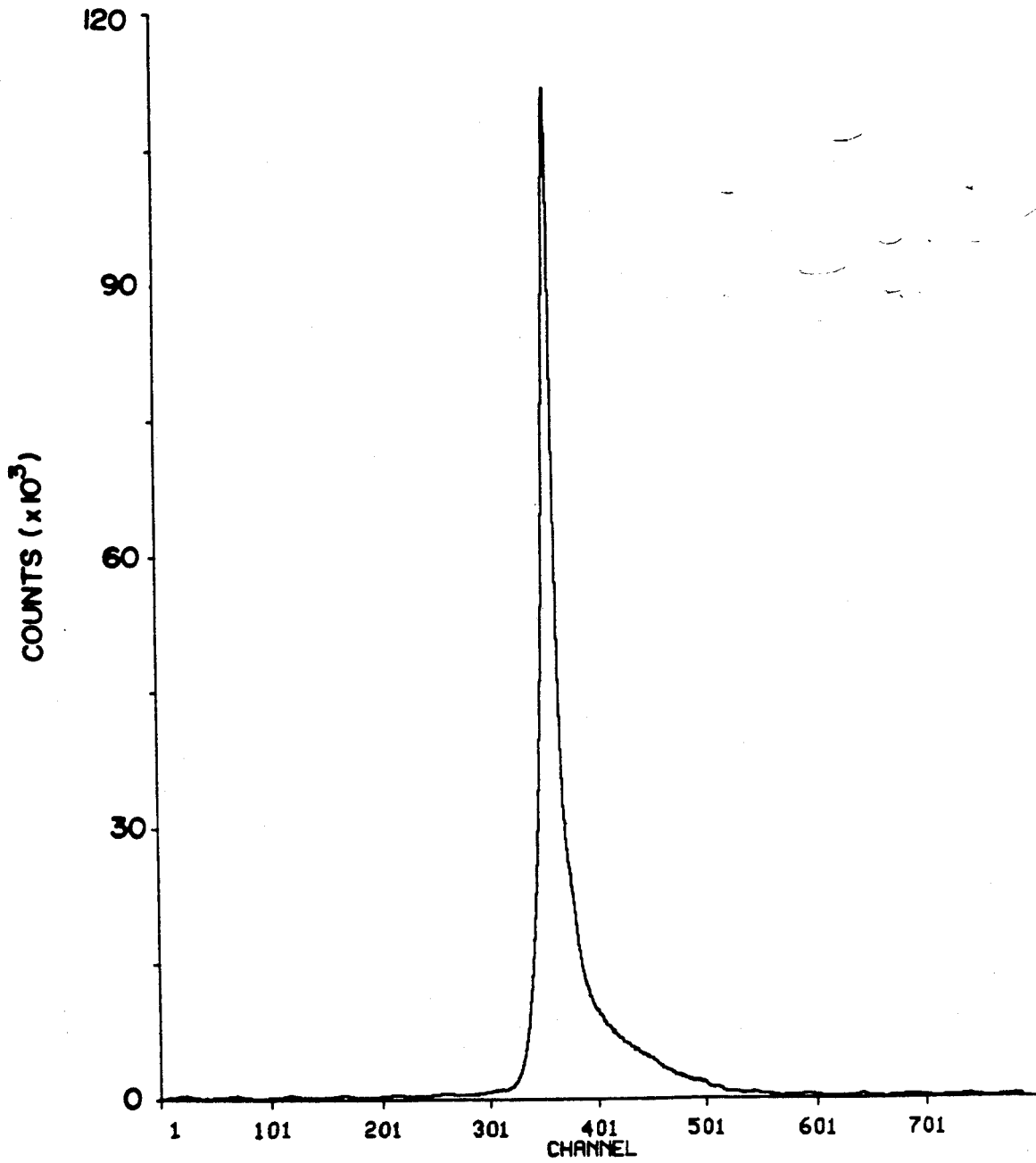
Figure 3.4   TAC spectrum for the ^{168}Yb coincidence experiments.
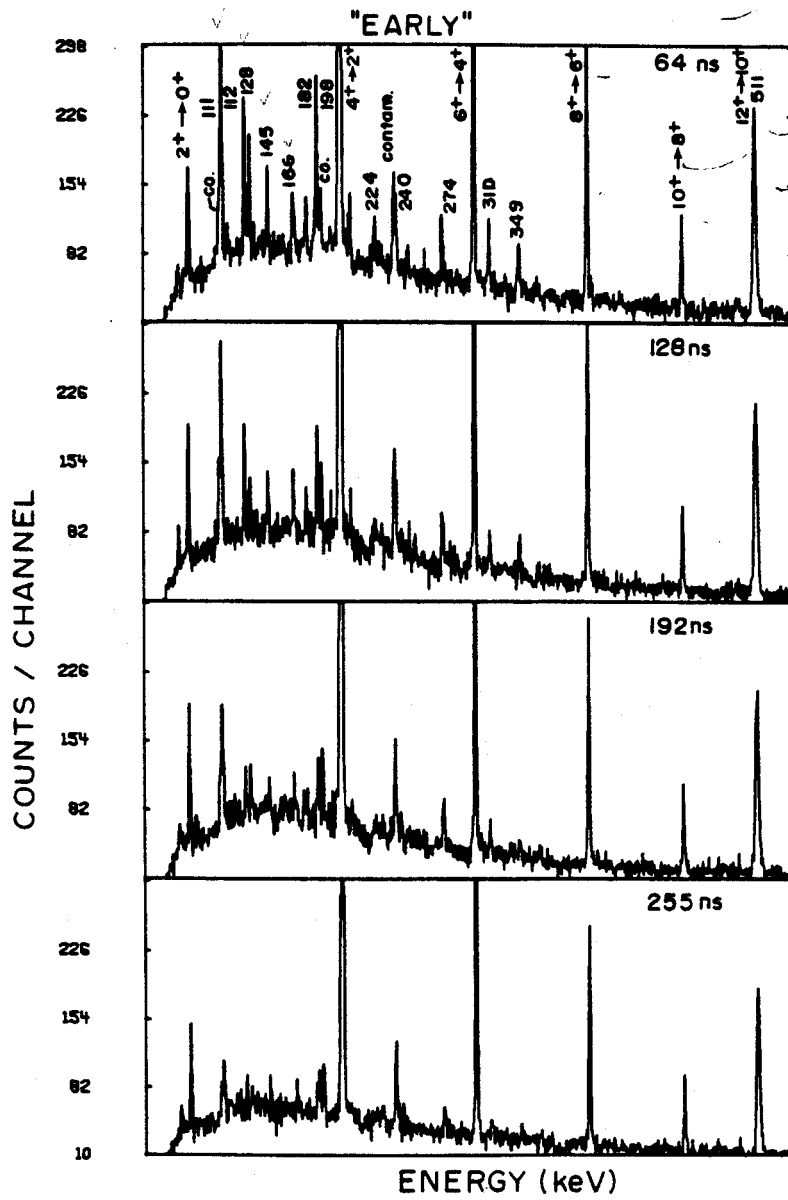
Figure 3.5 "Early" TAC time slices for the [168]Yb timing experiments.

48
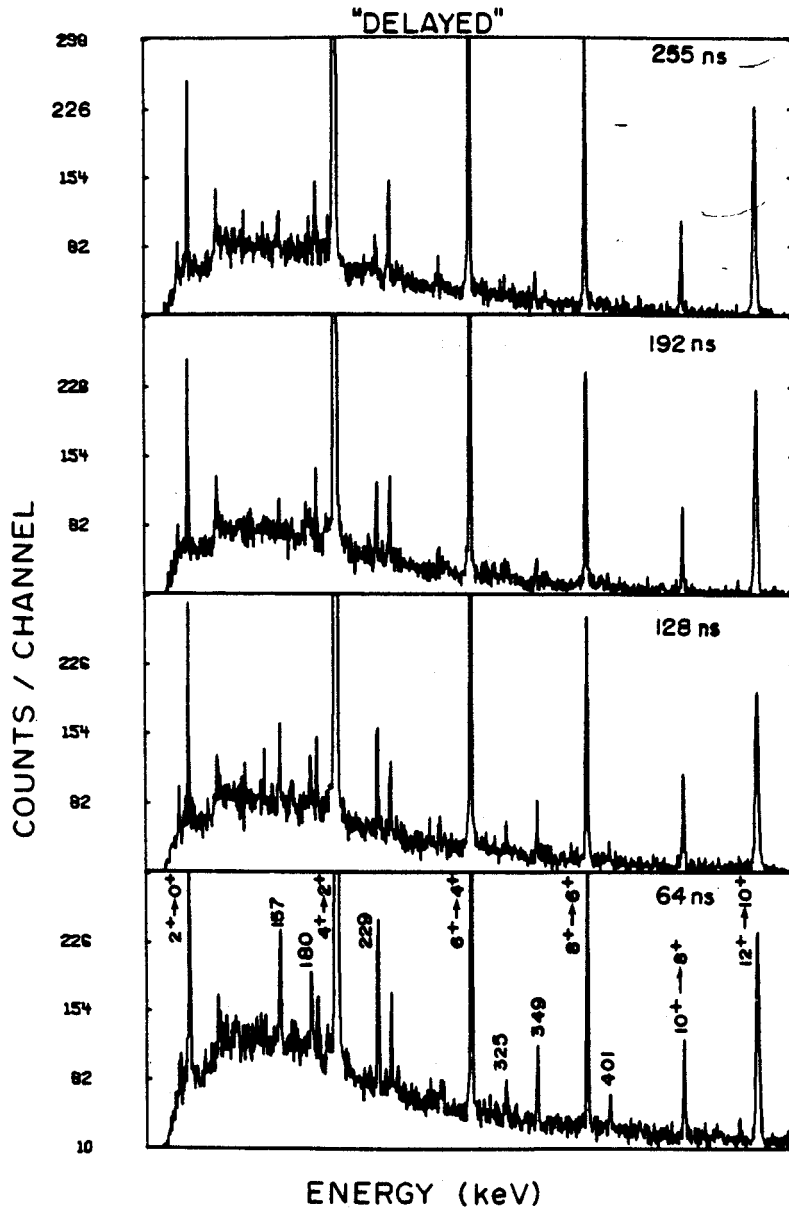
Figure 3.6   "Delayed" TAC time time slices for the ^{168}Yb timing
experiments.

decaying out of the 5⁻ isomer. By taking the area under a γ-ray peak and plotting it against time, a typical radioactive growth or decay curve is obtained (Figures 3.7 and 3.8) and its half-life (the standard deviation is obtained from weighted least-squares fit) can be determined. For the "early" region, all γ rays with the same half-life indicate that they are members of the same isomer band, and for the "delayed" region it would indicate that they are coming from the same isomer bandhead.

It is also possible to obtain a time spectrum for each γ ray by placing a gate on its energy, in coincidence with an open gate for the other detector, and the projected time spectrum gives a prompt peak as well as two off-prompt regions where a decay curve indicates the existence of an isomer. In Figure 3.9, the time spectra for some of the $\Delta I = 1$ transitions of the $K^\pi = 5^-$ isomer are shown. They clearly show a long decay and the slope is equal to the $t_{1/2}$ of the isomer. Similarly, in Figure 3.10, some of the transitions coming out of the $K^\pi = 5^-$ isomer are plotted, and the "decay" slope in the "positive" time is equal to the $t_{1/2}$ of the isomer. The "negative" time region in Figure 3.10 suggests another isomer. A TAC spectrum was obtained by gating on two relatively prompt transitions like the $2^+_g \rightarrow 0^+_g$ versus the $4^+_g \rightarrow 2^+_g$ where a similar behavior was displayed indicating that the effect is due to the long time taken for charge collection in the large Ge detector. A list of the half-lives obtained by these two methods is in Table 3.2. By using the above information, as well as
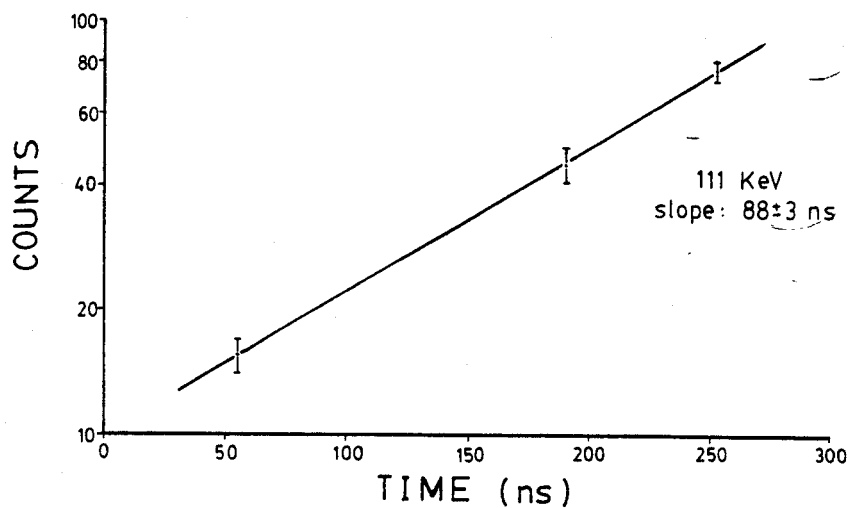
Figure 3.7 Radioactive "growth" curve for the 111-keV transition in the $K^{\pi}=5^-$ isomer band in ^{168}Yb.
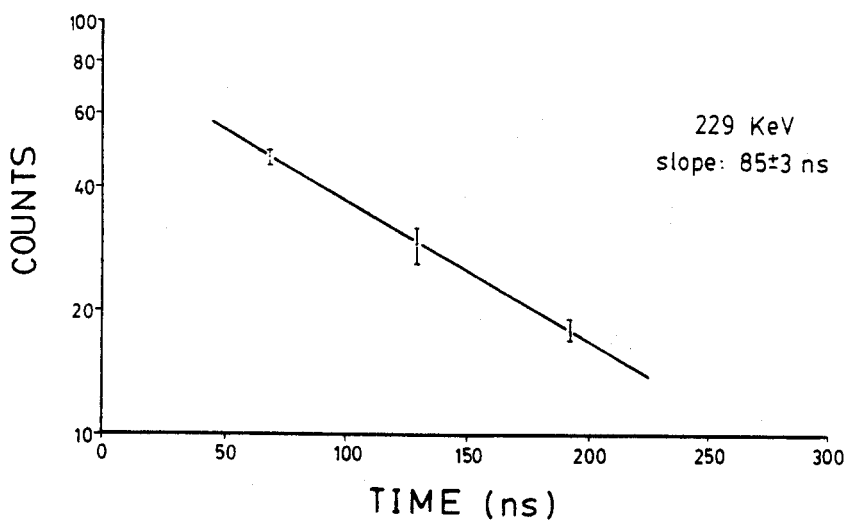
Figure 3.8 Radioactive "decay" curve for the 229-keV transition out of the $K^{\pi}=5^-$ isomer bandhead.
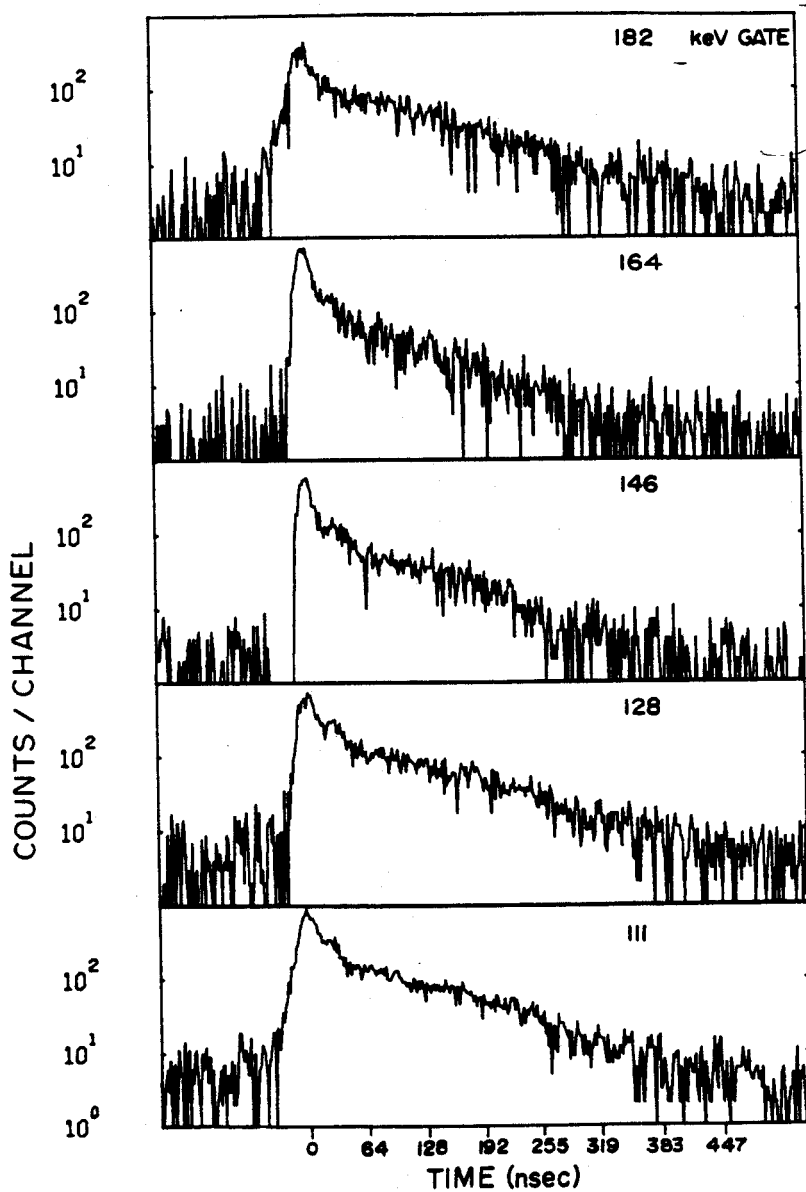
Figure 3.9 Time spectra for some important $\Delta\ell=1$ transitions for the $K^\pi=5^-$ isomer in ^{168}Yb.
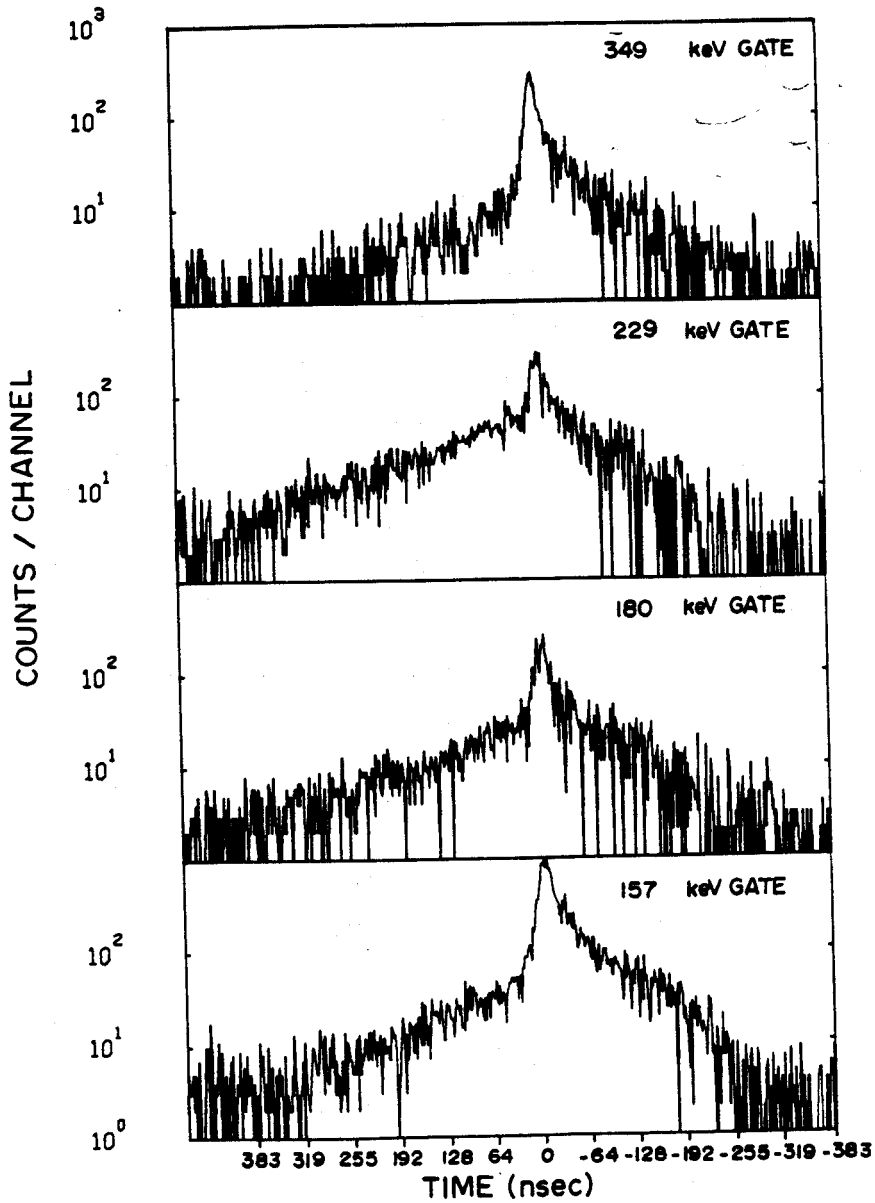
Figure 3.10   Time spectra for some important transitions out of the $K^\pi=5^-$ isomer bandhead in ^{168}Yb. The decay slope in the "positive" time region is equal to $t_{1/2}$ of the isomer.

TABLE 3.2

Half-lives for the $K^\pi = 5^-$ isomer obtained by two different methods described in the text.

$I_i^\pi K \rightarrow I_f^\pi K$	E_γ (keV)	$t_{1/2}(1)$ (ns)	$t_{1/2}(2)$ (ns)
$6^-5 \rightarrow 5^-5$	111.5	88 ± 3	76 ± 2
$7^-5 \rightarrow 6^-5$	128.5	a	70 ± 2
$8^-5 \rightarrow 7^-5$	145.9	a	67 ± 3
$9^-5 \rightarrow 8^-5$	164.1	-	65 ± 4
$10^-5 \rightarrow 9^-5$	181.5	a	68 ± 4
$7^-5 \rightarrow 5^-5$	240.1	75 ± 7	-
$8^-5 \rightarrow 6^-5$	274.3	a	-
$5^-5 \rightarrow 6^+$	157.0	76 ± 5	68 ± 6
$5-5 \rightarrow (1770)^b$	228.7	85 ± 3	79 ± 4

a ^{19}F or oxide matrix contaminant lines are present.
b Neither spin nor parity have been assigned; energy level is given in parenthesis.
NOTE: Standard deviations on the half-life are derived from fitting errors from SAMPO.

the coincidence results, the $K^\pi=5^-$ isomer band was constructed up to spin 11^- and its half-life was calculated to be 74 ± 5 ns. More detailed discussion about the $K^\pi=5^-$ isomer band is left to Chapter IV.

3.3 Angular-Distribution Measurements

In (HI,xn) reactions, the resulting compound nuclei will have their spins highly aligned along the plane perpendicular to the beam axis [Di66]. The initial spin alignment of such compound nuclei will remain essentially the same, even after the evaporation process is over, since the exiting neutrons carry little angular momentum. Therefore, the γ rays depopulating the discrete states of the "cold" residual nuclei will be anisotropic, and the angular distribution of the radiation field will depend on the initial and final states as well as on the multipolarity of the γ rays emitted. By experimentally determining the distribution curve shape, it is possible to confirm the placement of the γ rays in the level scheme previously done using the coincidence experiments.

To measure these intensities, the coaxial Ge(Li) detector (main detector) was placed on the movable arm of the MSU goniometer at 25 cm away from the target. Singles spectra were taken at 90°, 105°, 115°, 125°, 135°, and 145° with respect to the beam direction and were normalized against the x rays emitted isotropically by the erbium target nuclei. During these measurements, an additional fixed detector was used as a backup normalization method. A pulser was also used

to monitor dead-time corrections, but these and the solid-angle corrections were less than two percent, according to the tables of solid-angle corrections of Camp et al. [Ca69].

The γ-ray yields at each energy were fitted by the normalized angular distribution function

$$W(\theta) = 1 + A_2 P_2(\cos \theta) + A_4 P_4(\cos \theta) , \qquad (3.1)$$

where A_i is the angular distribution coefficient and $P_i(\cos \theta)$ is the Legendre polynomials. A more in-depth discussion of the angular distribution equation is left for Chapter V, Section 2.

From the fitted curves, the angular distribution coefficients were extracted. In a general way, for the ^{168}Yb decay scheme obtained, positive A_2 indicated $\Delta\ell=2$ multipolarity while negative A_2 indicated $\Delta\ell=1,2$. Whenever large negative A_2 were obtained, mixed multipolarity (M1,E2) was assumed according to the tables of der Mateosian et al. [de74] and Yamazaki [Ya67]. In Table 3.1, the angular distribution coefficients measured are listed. The large error bars in some of the coefficients are due to poor peak fitting done by SAMPO because these transitions were weak.

CHAPTER IV

YTTERBIUM-168 EXPERIMENTAL RESULTS

4.1 The Ground State Rotational Band

In the deformed rare-earth region (α,xn) reactions can be used to populate the ground state rotational band (g.s.b.) up to a spin of about 16^+, and they can be favorably used to study side bands up to 14^+ [Tj68]. Accordingly, in the $^{168}Er(\alpha,2n)$ experiments performed here, it was possible to construct the g.s.b. of ^{168}Yb up to 14^+. Also, the angular distribution coefficients measured for the g.s.b. are in good agreement with previously reported results elsewhere [Jo72], as shown in Table 4.1.

The N=98 isotones are "non-backbenders" (large interaction between the g- and s-bands), as exemplified by ^{168}Yb in a plot of I_x versus $\hbar\omega$ (Figure 4.1). Therefore, the moment of inertia to be used in the experimental calculations of the different properties involved in the Cranking Shell Model calculations for the side bands can be extracted from the g-band as pointed out in Chapter II, Section 3.5. Usually, the s-band is used as a reference configuration because it fulfills the two criteria representative of the quasiparticle vacuum: i) it should be yrast or close yrast; and ii) it should vary smoothly and

TABLE 4.1

Angular distribution coefficients for the ground state rotational band

Transition	Energy (keV)	Angular Distribution Coefficients			
		A_2/A_0	A_4/A_0	A_2/A_0	A_4/A_0
		(this work)		(reference)	
$2^+ \rightarrow 0^+$	87.8	0.011(40)	-0.036(6)	0.012(5)	-0.10(4)
$4^+ \rightarrow 2^+$	199.0	0.27(1)	-0.053(9)	0.25(4)	-0.02(3)
$6^+ \rightarrow 4^+$	298.7	0.34(13)	-0.18(21)	0.28(4)	-0.03(3)
$8^+ \rightarrow 6^+$	384.7	0.43(2)[b]	-0.20(3)	0.30(4)	-0.05(3)
$10^+ \rightarrow 8^+$	455.2	0.35(2)	-0.10(3)	0.32(4)	-0.04(3)
$12^+ \rightarrow 10^+$	510.5[a]				
$14^+ \rightarrow 12^+$	552.7	0.40(6)	-0.21(10)	0.31(4)	-0.12(3)

[a] Contains contributions from the annihilation radiation.

[b] Contains contributions from multiplet.
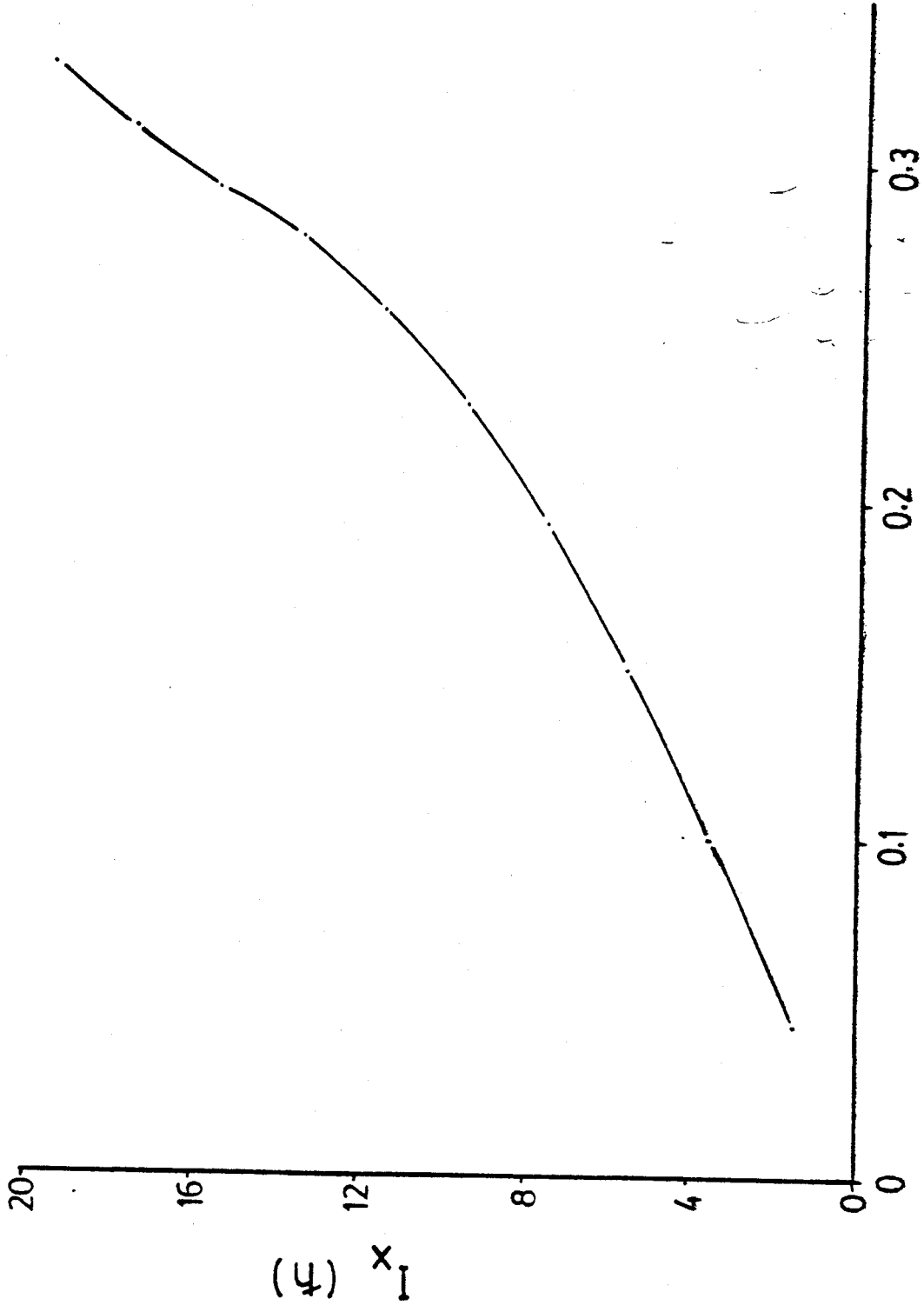
Figure 4.1 Plot of I_x versus $\hbar\omega$ for ^{168}Yb.

slowly with the rotational frequency. For the former, the reference state is assured to exist as an individual state and it is usually known very well for being in the yrast region (therefore, easily accessible by different reactions). For the latter, a sudden change of the reference at certain rotational frequency is readily observed as an irregularity (like the backbending) at the same frequency for all excitations.

For ^{168}Yb, a "non-backbender", the s-band is not useful as a reference state because the mixing between the g- and s-bands is large and stretches over several spins in the s-band. Therefore, it becomes difficult to use the extrapolation technique described in Chapter II, Section 3 (Equation 2.3.30) because the s-band is not "pure" up to the measured spins. Then, the extrapolated $\mathfrak{I}_0$ and $\mathfrak{I}_1$ values for the s-band will reflect this mixing and will be transferred into the functions of e' and i of the excited configurations (these are relative functions obtained by using a reference state) whose absolute E' and I_x functions are regular. To avoid this difficulty, the g-band is used as a reference because the lower spin states of this band are not so strongly affected by the mixing as the s-band is, and so better $\mathfrak{I}_0$ and $\mathfrak{I}_1$ values can be obtained. In Figure 4.2 a plot of measured $\Delta I_x/\Delta\omega$ versus $\hbar^2\omega^2$ for the g-band of ^{168}Yb is shown, and the extracted values for $\mathfrak{I}_0$ and $\mathfrak{I}_1$ are 33.6 $\hbar$MeV^{-1} and 146 $\hbar^3$MeV^{-3}, respectively. It can also be seen in this figure that above $\hbar^2\omega^2 = 0.03$ MeV the mixing starts to strongly affect the g-band so that the upper spin states deviate from the extrapolated $\mathfrak{I}_0$ and $\mathfrak{I}_1$ values.
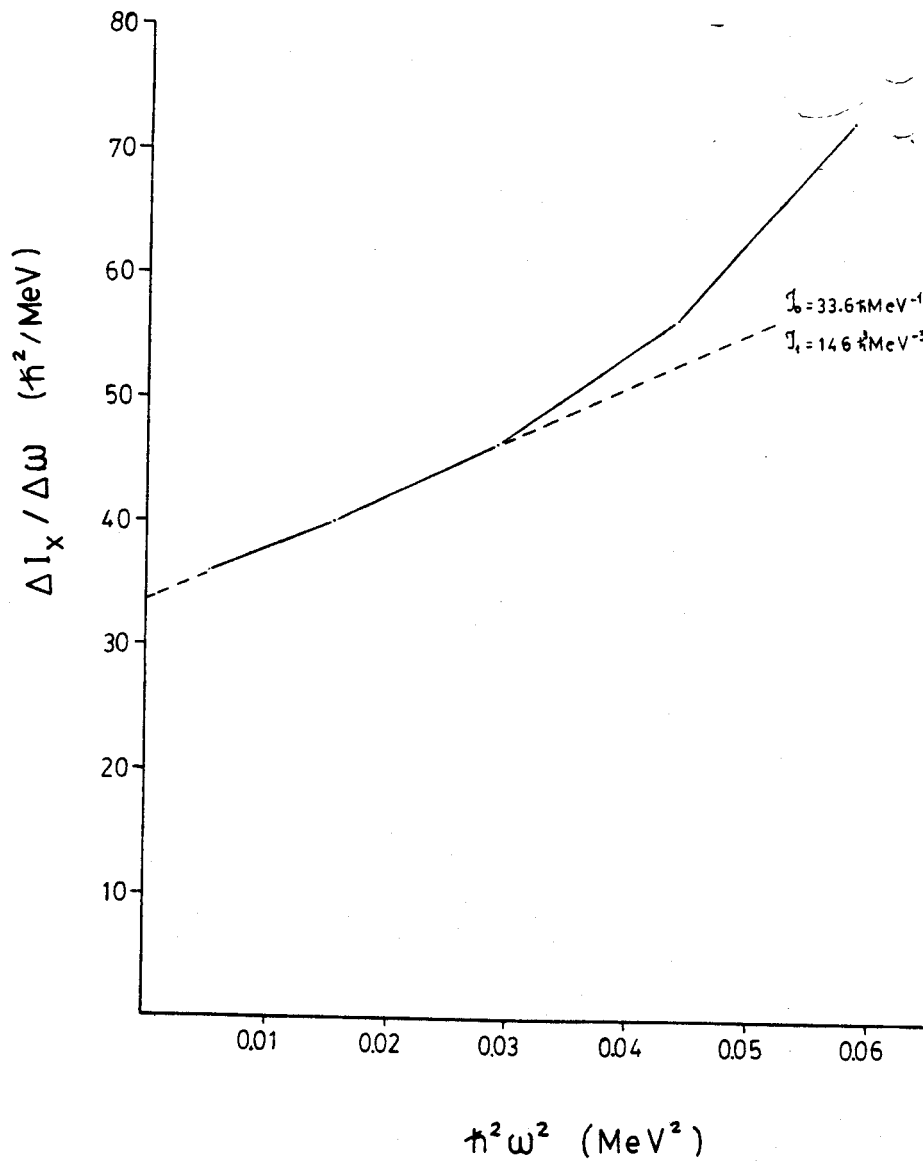
Figure 4.2 Plot of $\Delta I/\Delta\omega$ versus $\hbar^2\omega^2$ for the g-band in ^{168}Yb.

4.2 The γ-Vibrational Band

A band that was strongly populated in this experiment is believed to be the γ-vibrational band. Previously, the spins up to 6+ [Ch70], and possibly 7+ [Je70] were identified. In both experiments the data were obtained by using (α,5n), (p,2n) and (d,3n) reactions, and the multipolarity of the interband transitions as well as the band parity were determined.

In this work it was possible to firmly establish the spin 7+ state and to extend the band up to spin 11+. The intraband transitions observed were mostly ΔI = 2 crossover and a few ΔI = 1 cascade transitions could be seen. Virtually no intraband activity was observed for the lower members of the band. This latter behavior can be explained by the fact that interband sidefeeding into the ground-state rotational band (g.s.b.) was strongly favored at high spins, greatly decreasing the population of the lower members of the band. These lower levels could only be observed because of the sidefeeding to the lower spins of the γ-band by other bands of higher energy.

One interesting characteristic that is seen in this band relates to the sidefeeding pattern where a preference of the transitions between like-spins, e.g. $4_\gamma^+ \rightarrow 4_g^+$ (M1,E2 transition) as opposed to $4_\gamma^+ \rightarrow 2_g^+$ (pure E2 transition), was observed. These data, together with the angular distribution results, can be used for a comparison with the sidefeeding pattern predicted by the simple rotational model. The idea is to obtain a ratio of the photon transition probability

example, the $4^+_\gamma \rightarrow 4^+_g$ over the $4^+_\gamma \rightarrow 2^+_g$, and compare to the theoretical values. Deviations that occur can be due to some perturbation like band mixing with the ground state rotational band.

In this model the transition probability for emission of a photon of energy E_γ is proportional to (for E2 transitions):

$$T(E2\mu, I_i \rightarrow I_f) \propto E_\gamma^5 \, B(E2, I_i \rightarrow I_f) \qquad (4.2.1)$$

where

$$B(E2, I_i \rightarrow I_f) = (2I_i + 1)^{-1} \sum_{M_f, M_i} \left| \langle K' I_f M_f | Q_2 | K I_i M_i \rangle \right|^2 \qquad (4.2.2)$$

is the reduced transition probability for E2 transitions. Similar equations can be obtained for M1 transitions. Experimentally, the transition probability ratio between $\left(I_i \rightarrow I_f\right)_{mixed}$ and $\left[I_i \rightarrow (I-2)_f\right]_{pure}$ can be expressed as a transition intensity ratio, namely,

$$\frac{I_{\gamma,m}}{I_{\gamma,p}} = \left(\frac{T(E2)_m + T(M1)_m}{T(E2)_p} \right) \qquad (4.2.3)$$

where p and m subscripts are used to simplify the equations.

For a mixed M1,E2 transition, one can obtain a ratio of T(E2) over T(M1) that is equal to the mixing ratio δ of the transition, i.e.,

$$\delta = [T(E2)/T(M1)]^{1/2} . \qquad (4.2.4)$$

By substituting equation (4.2.4) into (4.2.3), the following is obtained:

$$\frac{I_{\gamma,m}}{I_{\gamma,p}} = \left(\frac{T(E2)_m + T(E2)_m/\delta^2}{T(E2)_p} \right) \tag{4.2.4}$$

where the mixing ratios can be obtained from the angular distribution results and the tables in reference [de74].

Equation (4.2.5) is further simplified by substituting $T(E2)$ using equation (4.2.1):

$$\frac{I_{\gamma,m}}{I_{\gamma,p}} = \left(\frac{B(E2)_m \; E_{\gamma,m}^5}{B(E2)_p \; E_{\gamma,p}^5} \right) \left(1 + \frac{1}{\delta^2} \right) \tag{4.2.5}$$

Rearranging the equation, the following is obtained:

$$\frac{B(E2)_m}{B(E2)_p} = \left(\frac{E_{\gamma,p}}{E_{\gamma,m}} \right)^5 \left(\frac{I_{\gamma,m}}{I_{\gamma,p}} \right) \left(\frac{\delta^2}{1 + \delta^2} \right) \tag{4.2.6}$$

Therefore, the experimental ratio between $B(E2)_{mixed}$ and $B(E2)_{pure}$ is obtained from the intensities of the mixed M1,E2 and the pure E2 of the $I_i \rightarrow I_f$ transitions between γ-band and the g.s.b.. The theoretical ratios are obtained from the matrix elements (see equation 4.2.2), namely,

$$\frac{B(E2)_m}{B(E2)_p} = \left(\frac{M(E2)_m}{M(E2)_p} \right)^2 \tag{4.2.7}$$

The matrix elements $M(E2)$ are obtained from Clebsch-Gordan coefficients.

In Table 4.2 a list of the experimental and theoretical, mixed/pure B(E2) values using the simple rotational model are shown. The experimental values are in near agreement, considering the error bars. The larger deviation corresponding to the spin 6^+ could imply that some effect is perturbing the band behavior as discussed below.

Also, another interesting feature is the deviation from the rotational I(I+1) dependence. This is readily observed in a plot of $(E_I - E_{I-I})/2I$ versus I^2 as shown in Figure 4.3. It can be seen that the even members are depressed in energy in relation to the odd members, and are said to be "favored".

One possible explanation for the two features above is that they result from the non-adiabatic coupling of the intrinsic and rotational motions of the nucleus. This is, from the mixing of the γ-vibrational band with the g.s.b. as a first-order effect. The simple rotational model [Bo53] assumes that the nucleus is an axially-symmetric rotor, and that the rotational and intrinsic motions do not perturb each other. But for bands with good K quantum number, it is possible to have strong coupling through non-adiabatic interaction between the rotational and intrinsic motions. This non-adiatic coupling mixes the wave function for the rotational and vibrational bands and leads to deviations on the B(E2) values. The deviations are reflected on both intensity and ener-values for the interband transitions between the γ-vibrational and ground state rotational bands [Ri69]. The exact form of this coupling might be understood in terms of the Coriolis forces. That is, the

TABLE 4.2

List of experimental and theoretical B(E2) ratios for $I_i \rightarrow I_f$ transitions between the γ-band and the ground state rotational band

I_i^π	Experimental $B(E2)_{mixed}/B(E2)_{pure}$	Theoretical $B(E2)_{mixed}/B(E2)_{pure}$
4^+	3.67 ± 1.21	2.94
6^+	7.69 ± 3.10	3.74

Note: Values for other spins could not be obtained because of unreliable angular distribution values coming from resolved multiplets.
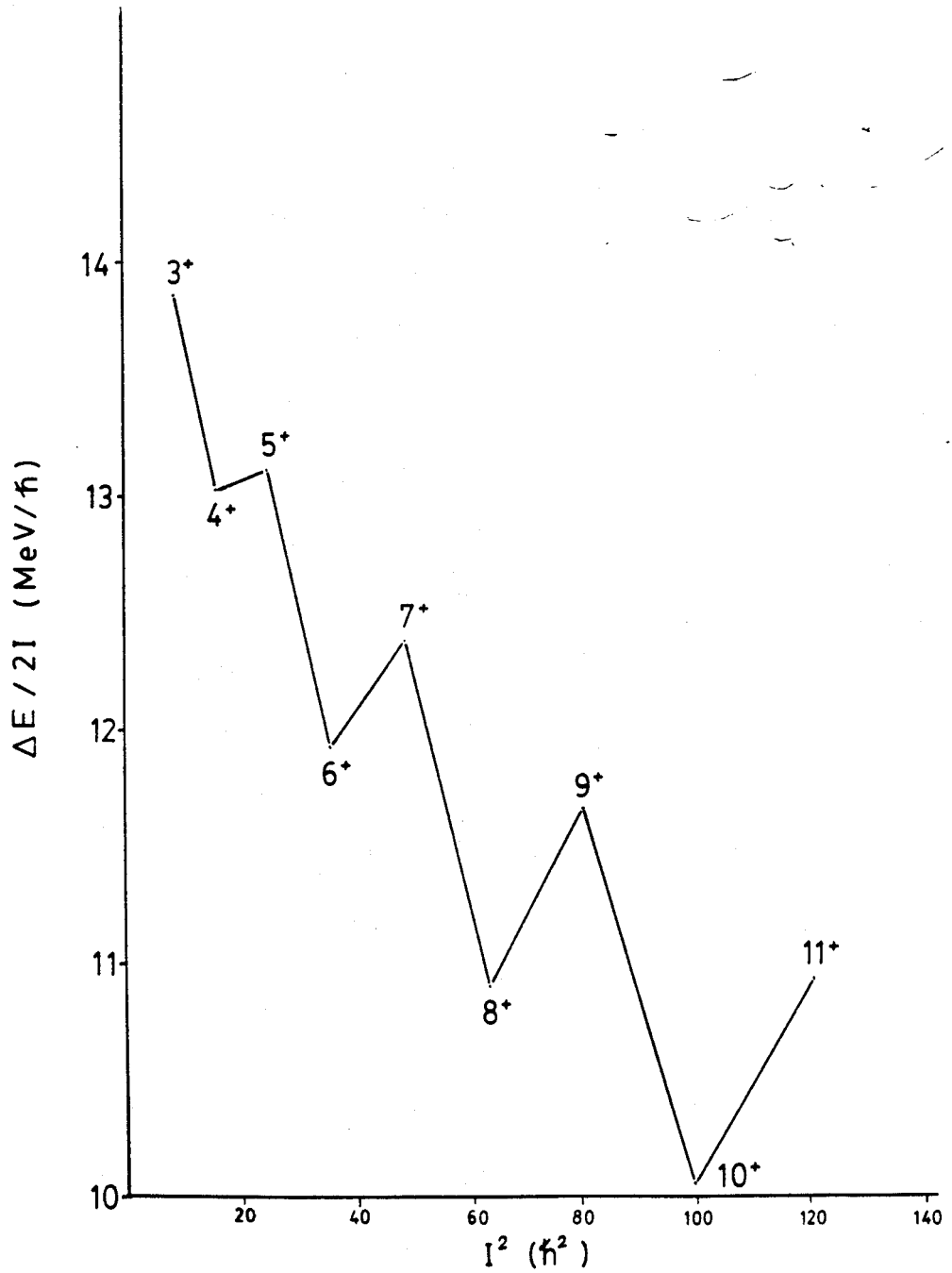
Figure 4.3 Plot of $\Delta E/2I$ versus I^2 for the γ-band in ^{168}Yb.

Coriolis forces have a tendency to align the core's angular momentum along the rotational axis, and this implies a tendency of the nucleus to break away from axial symmetry. This will cause a coupling between the rotational motion to the collective vibrations around the axial symmetry, hence, a coupling between the γ-vibrational and ground state rotational bands [Bo75]. Also, this perturbation can be further observed experimentally as a compression of the level spacing in the γ-band (Figure 4.3) because the band mixing propagates through the even spin members of the vibrational band since both the ground state and the β-vibrational bands have even spins only.

4.3   The $K^{\pi} = 3^+$ Band

The $K = 3^+$ band was previously known up to 5^+ and possibly to 6^+ [Ch72], and it was assumed to be an even-parity rotational band built on the 3^+, 1451.8-keV level. Also, in reference [Ch70], the ratio of the reduced transition probability from the 4^+ level at 1551.4 keV to the g.s.b., namely, the $B(E2,I K \rightarrow 2^+0)/B(E2,I^{\pi}K \rightarrow 4^+0)$, was calculated to be equal to 0.31(6). Together with the intraband transitions, it was suggested this level be assigned to the $K^{\pi} = 3^+$ band. Although the existence of intraband transitions was mentioned in [Ch72], no intensity values were reported.

It was possible to confirm these levels in the present work, and firmly place the 6^+ level at 1819.5 keV, the 7^+ level at 1985.4 keV, and possibly the 8^+ level at 2174.8 keV. Information on the

quasiparticle structure of the band may be obtained from an analysis of the mixing ratios, δ, for cascade and crossover transitions within the band, using the Nilsson [Kh73] and rotational models. The mixing ratios can be obtained from the branching ratios of the $^{166}Er(\alpha,2n)$ coincidence and angular distribution experiments. For the former,

$$\delta^2/(1+\delta^2) = [2\lambda K^2(2I-1)/(I+1)(I-1+K)(I-1-K)].[E_{I\to-1}/E_{I\to I-2}]^5 \quad (4.3.1)$$

where $\lambda = I_\gamma(I\to I-2)/I_\gamma(I\to I-1)$. The sign of δ is obtained from the angular distribution experiments [de74]. According to the rotational model the g-factor in a rotational band, g_K (gyromagnetic ratio for a K^π band) is constant in relation to the core g-factor, g_R. That is, the difference g_K-g_R is constant for all the rotational states in an unperturbed (not mixed) band. The gyromagnetic ratio difference can be calculated according to

$$(g_K-g_R) = 0.93 \ (E_{I\to I-1})Q_0/\delta(I^2-1)^{1/2} \quad (4.3.2)$$

where the energies are given in MeV, the quadrupole moment Q_0 is approximately equal to 7.4 barns [Lo70], and g_R is equal to 0.32 [Kr68]. Since the δ value is very sensitive to the transition intensities, the peak areas obtained from the planar detector were used in the intensity calculations because of the detector's resolution at low γ-ray energy. In Table 4.3 the calculated δ's are listed as well as the (g_K-g_R) values. The relative constancy of the (g_K-g_R) values affirm the placement of the levels in a single rotational band. The average value for (g_K-g_R) is taken to be 0.57(6), and, therefore, the

TABLE 4.3

Mixing ratios and (g_K-g_R) values for $K^\pi = 3^+$ band in ^{168}Yb using the planar detector intensity results

$I^\pi_i - I^\pi_f$	Energy (keV)	I_γ	δ	$(g_K - g_R)$
$5^+ \to 4^+$	0.1230	51.6(4.1)	0.38(4)	0.46(5)
$5^+ \to 3^+$	0.2227	32.8(4.3)		
$6^+ \to 5^+$	0.1450	48.8(3.4)	0.30(4)	0.56(6)
$6^+ \to 4^+$	0.2680	48.9(6.4)		
$7^+ \to 6^+$	0.1660	41.8(4.2)	0.29(5)	0.58(6)
$7^+ \to 5^+$	0.3110	67.1(7.4)		

value for g_K is +0.85(9). In general, for a singlet two-quasiparticle state, the g_K values are:

$$g_K = 0 \text{ for neutrons}$$

and

$$g_K = 1 \text{ for protons.}$$

Hence, the calculated g_K value above indicates that this band has predominantly a two-quasiproton structure with about 15% neutron admixture. The possible configuration for the 3^+ band is $\{7/2^+[404]_p, 1/2^+[411]_p\}$ as it will be discussed below.

This result contrasts with the corresponding band in ^{172}Yb with a $g_K = 0.2$ [Wa80] where the dominating (80%) $\{5/2^-[512]_n, 1/2^-[521]_n\}$, two-quasineutron structure is also evident from particle transfer [Bu67] experiments. The contrasting features of the band structure for these two isotopes is further highlighted by the angular distribution coefficients having different signs indicating different quasiparticle structure domination. For this deformed mass region it is possible to obtain several two-quasiparticle configurations that could give origin to the observed $K^{\pi} = 3^+$ bands. In calculations performed by Walker, Carvalho and Bernthal [Wal] it is shown that the lowest K^{π} two-quasiparticle configuration are all of the singlet type (intrinsic spin projections cancel) for the 98<N<104, 68<Z<72 region. They were also able to show that the neutron character for the 3^+ bands changes in this region as shown in Figure 4.4 for the 4^+3 states. The difference between the experimental and the theoretical

Figure 4.4 $K^\pi = 3^+$ levels in the A ∼ 170 region. The thick horizontal bars represent the experimental I = 4 levels; below each is given its energy in keV, and above is given the cross section at 125° (in μb/sr) from 12 MeV deuteron inelastic scattering. Calculated two-quasiparticle energies are shown by the thin horizontal bars, for the $\{7/2^+ [404]_p, 1/2^+[411]_p\}$ (p1), $\{5/2^+[402]_p, 1/2^+[411]_p\}$ (p2), $\{5/2^-[512]_n, 1/2^-[512]_n\}$ (n1) and $\{7/2^-[514]_n, 1/2^-[521]_n\}$ (n2) singlet configurations.

Figure 4.4 $K\pi = 3^+$ levels in the A ~ 170 region. The thick horizontal bars represent the experimental I = 4 levels; below each is given its energy in keV, and above is given the cross section at 125° (in μb/sr) from 12 MeV deuteron inelastic scattering. Calculated two-quasi-particle energies are shown by the thin horizontal bars, for the {7/2+ [404]ₚ, 1/2+[411]ₚ} (p1), {5/2+[402]ₚ, 1/2+[411]ₚ} (p2), {5/2−[512]ₙ, 1/2−[512]ₙ} (n1) and {7/2−[514]ₙ, 1/2−[521]ₙ} (n2) singlet configurations.

energy trends for the different configurations and in part be explained phenomenologically as a result of the proton-neutron admixture where the participation of the neutron in the band structure generally lowers the band energies.

It is known that inelastic deuteron scattering will preferentially excite collective states, and in [Bu67] the 4^+ state of the 3^+ band was observed in several Yb isotopes. This would indicate that a certain amount of collectivity is present in the 4^+3 level. Therefore, some interaction between the collective and two-quasiparticle degrees of freedom should be present in order to account for both experimental results described above. The possible collective motion that could be associated with the low-lying $K^\pi = 3^+$ bands would be the hexadecapole vibration. That is, in the A ~ 170 region, there are several low-lying two-quasiparticle configuration with the same K^π that would favor the K = 3 hexadecapole vibration.

In this deformed region other vibrational modes usually are low-lying in energy but are incompatible with a K = 3 band assignment as in the case of the β-vibration (zero unit of angular momentum along the symmetry axis) with a K = 0 and the γ-vibration (two units of angular momentum along the symmery axis) with a K = 2. The octupole vibration (zero to three units of angular momentum along the symmetry axis) is an odd-parity excitation, hence incompatible with the $K^\pi = 3^+$ band. Additionally, the K = 3 hexadecapole vibration would be expected

in this mass region since the pair of quasiparticles that contribute to the low-lying $K^\pi = 3^+$ bands have asymptotic quantum members so that $\Delta n_z = 1$ (favors the hexadecapole vibration).

In summary, the $K^\pi = 3^+$ band has a predominantly (85%) { $7/2^+$ [404]$_p$, $1/2^+$ [411]$_p$ }, two-quasiproton structure in contrast with the corresponding $K^\pi = 3^+$ band in ^{172}Yb which has a predominantly (80%) { $5/2^-$ [512]$_n$, $1/2^-$ [521]$_n$ }, two-quasineutron configuration. In addition, the band is strongly excited by inelastic deuteron scattering implying some interaction between intrinsic motion and vibrational hexadecapole oscillations.

4.4   The $K^\pi = 5^-$ band

The level at 1999.3 keV has been tentatively assigned as a $K^\pi = 5^-$ bandhead [Ch70] and as having a half-life of 81.7 ± 4.5 ns [Ch73]. The level at 2110.8 keV was established as a 6^- rotational state of the isomer [Ch72]. The long half-life indicates a large hindrance for the transitions depopulating this level and, therefore, a large K value would be expected for the band. This isomer has been assigned a Nilsson configuration { $7/2^-$ [523]$_p$, $1/2^+$ [411]$_p$ } by [Ch72] based on similar trends in ^{164}Er and β^+-decay of the { $7/2^+$ [404]$_p$, $5/2^-$ [523]$_n$ }, the ground-state of ^{168}Lu.

In the present ^{166}Er(α,2n) experiments, it was possible to extend the band up to 10^- and possibly 11^- spin. Crossover and cascade

intra-band transitions were observed more clearly in the delayed $\gamma\gamma$-coincidence analysis. Angular distribution results were also used to confirm these placements. Some sidefeeding from another band into the isomer band was observed. The deexcitation of this band occurs through six transitions including those to the $K^\pi_- = 3^+$ band but none to the g.s.b. (K=0) or to the γ-vibrational band (K=2), indicating a large K value for the isomer band. All the decay branches have been seen previously [Ch70] in the radioactive decay of ^{168}Lu.

The rotational structure of the band built on the 5^- level is reasonably regular as shown in Figure 4.5 where $2\mathcal{J}/\hbar^2$ versus $\hbar^2\omega^2$ is plotted. Also plotted are the long-lived isomers, based on 4^- (360 ns) for ^{170}Yb [Wa79] and 6^- (3.6 μs) for ^{172}Yb [Wa80]. Their suggested structures are $\{ 7/2^+ [633]_n, 1/2^- [521]_n \}$ and $\{ 7/2^+ [633]_n, 5/2^- [512]_n \}$ respectively. It can be seen that the 5^- isomer displays one of the general features of the other two isomers, namely, a much higher $2\mathcal{J}/\hbar^2\omega^2$ value than the g.s.b. (only the g.s.b. of the ^{168}Yb has been plotted in order to simplify the picture but the g.s.b. for ^{170,172}Yb behave nearly the same as that of ^{168}Yb at low spins). This indicates similarities in the band structure for the isomers. It has been demonstrated for the isomers in the neighboring Yb isotopes, [Wa79] and [Wa80], that this feature results from the Coriolis effects on an $i_{13/2}$ neutron. The Coriolis forces tend to decouple a nucleon pair in a high-j orbital and align their angular momentum with the rotation of the core [St75]. Therefore, a high

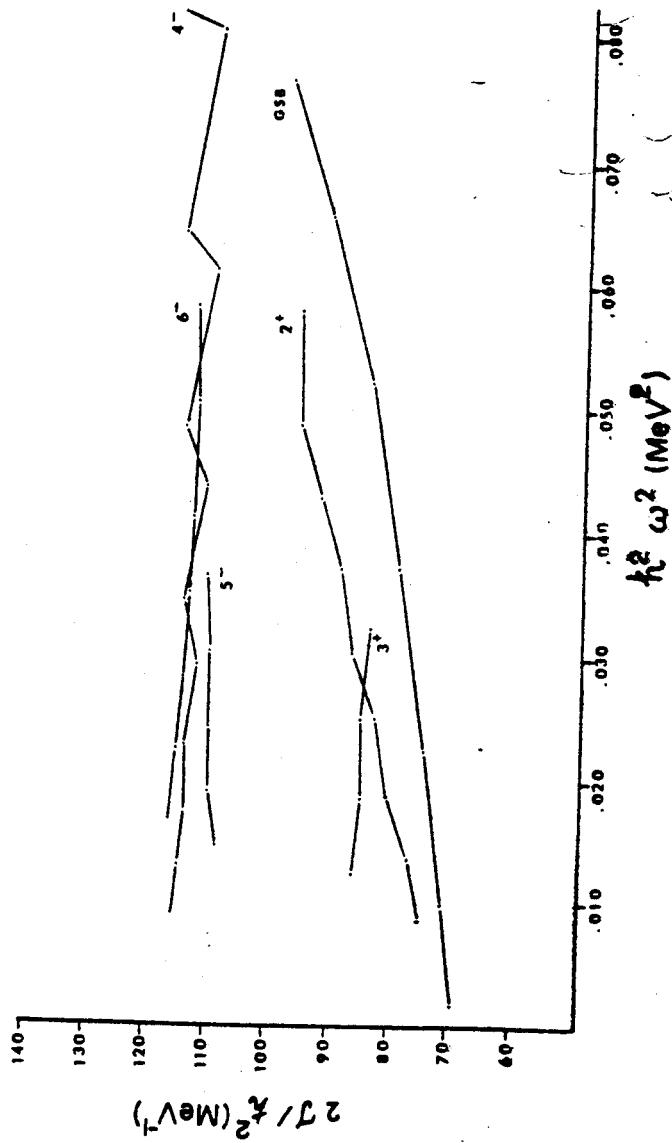Figure 4.5 Plot of $2 \mathcal{J}/\hbar^2$ vs. $\hbar^2\omega^2$ for the 5^- isomer and the ground state rotational bands for ^{168}Yb; the 4^- isomer for ^{170}Yb and the 6^- isomer for ^{172}Yb are also plotted.

effective moment of inertia (109 MeV^{-1} for ^{168}Yb) results from such alignment contributions. This behavior indicates the presence of an $i_{13/2}$ neutron in the band structure of the 5$^-$ isomer.

Mixing of the isomer band with other suitable, nearby bands can be reflected in a compression of the isomer band-levels as seen in Figure 4.5 for the 4$^-$ isomer in ^{170}Yb. This is not the case for the 5$^-$ isomer in ^{168}Yb since it has a fairly constant effective moment of inertia as compared to the 4$^-$ isomer in ^{170}Yb. Observation of transitions between the isomer band and other bands might indicate the presence of such bands available for mixing, but no such bands were observed.

Using the branching ratios, it is possible to calculate the $|g_K-g_R|$ value, as pointed out previously, with the sign determined by the angular distribution coefficients for the cascades in the band. In Table 4.4 the $|g_K-g_R|$ values are listed using both coincidence and TAC results. Using the most consistent set of results, a value of $|g_K-g_R|$ was calculated to be equal to 0.27(5). With the angular distribution results and g_R = 0.32 [Kr68], the value of g_K obtained is equal to +0.05(5). This implies that this band has predominantly a two-quasineutron structure with a small proton admixture. Using the Nilsson level diagram (Figure 2.1) in Chapter II, the lowest possible configuration consistent with the K^π = 5$^-$ band head is { 5/2$^+$ [642]$_n$, 5/2$^-$ [523]$_n$ }. There are two possible two-quasiproton band structures that could be used for band mixing, namely, the

TABLE 4.4

Calculated $\left| g_K - g_R \right|$ values for the $K^\pi = 5^-$ isomeric band of ^{168}Yb.

I	$\left\| g_K - g_R \right\|$		
	Coincidence	TAC(1)	TAC(2)
7	0.29(3)	0.26(3)	0.26(3)
8	0.28(4)	0.27(3)	0.28(3)
9	0.34(6)	0.31(5)	0.34(5)

Note: Two sets of TAC results(different time slices) were used in order to obtain a more statistically significant average.

{ $9/2^-$ [514]$_p$, $1/2^+$ [411]$_p$ } and the { $7/2^-$ [523]$_p$, $3/2^+$ [411]$_p$ }.

The former band configuration is energetically more favorable than the latter since it involves valence nucleons and Nilsson orbitals near the Fermi surface. For the latter configuration the Nilsson orbitals are well below the Fermi surface and, therefore, it would require much energy in order to have the correct two-quasiproton excitation. This conclusion is in contrast with the suggestion of Charvet et al. [Ch72], namely, { $7/2^-$ [523]$_p$, $1/2^+$ [411]$_p$ }. This suggested configuration gives a band of only K=4, and not the necessary K=5 assignment for the isomer.

The half-lives reported previously for this isomer are 53^{+38}_{-15} ns [Dr77] and 81.7 ± 4.5 ns [Ch73], and in the ^{166}Er(α,2n) delayed coincidence experiments the half-life obtained was 74 ± 5 ns as calculated in Chapter III, Section 3. This relatively long half-life can be explained in terms of K-forbiddenness (transitions with $\Delta K > \lambda$ multipolarity are hindered) which requires comparable K values for the bands to which the isomer decays. This is the case for $K^\pi = 5^-$ isomer where all the decay branches go to bands with K < 3. Besides the known $K^\pi = 3^+$ band, the other decay branches of the isomer seem to populate some members of what appears to be $K^\pi = 0^-$ and 2^- octupole bands according to previously measured reduced transition probabilities [Ch70] for the band members.

4.5 The Cranking Shell Model Calculations

In the deformed rare-earth even-even mass region the yrast spectrum is predominantly of collective nature at low angular momentum. At around I = 12-14 $\hbar$ and $\hbar\omega$ = 0.25 - 0.27 MeV, the yrast structure changes, and an excited quasiparticle band becomes yrast. This is the so-called backbending effect. Additionally, these are other quasiparticle excitations near the yrast line (on which rotational bands are built on) that are of much interest because they represent the breaking up of nucleon pairs which can affect the nuclear motion and shape. Studies on these quasiparticle bands leads of a better understanding of the nuclear dynamics at high excitation energy and angular momentum. The Cranking Shell Model has been quite successful in the theoretical analysis of both the yrast and near-yrast rotational spectra by using the idea that these quasiparticle excitations (and the corresponding rotational bands) can be decribed by the motion of a particle in a cranked deformed Nilsson potential. Such calculations are used in this section to describe the 5$^-$ isomer band. .

In order to simplify the description of a quasiparticle band it is useful to label the rotational configurations by the conserved quantum numbers, namely, the parity π and the signature α (the parity of a multi-quasiparticle state is the product of the parity of all participant quasiparticles, and α is the sum of all the participant α's). Therefore, the ground state rotational band has a $(\pi,\alpha)=(+,0)$ quasiparticle configuration. Consider the case of the three recently observed [Ro81] one-quasineutron bands in the neighboring odd-A ^{167}Yb.

The ^{167}Yb ground state rotational band has the $(-,1/2)$ quasineutron configuration, and it corresponds to the Nilsson 5/2$^-$ [523] single-particle configuration at $\hbar\omega=0$ MeV. The other two bands, $(+,1/2)$ and $(+,-1/2)$, correspond to the decoupled Nilsson 5/2$^+$ [642] single particle bands at $\hbar\omega=0$ MeV. A two-quasineutron band configuration can be obtained by coupling these two bands as $[(-,1/2), (+,\pm 1/2)]$, that is, $[(-,1/2)\times(+,1/2)] = (-,1)$ and $[(-,1/2)\times(+,-1/2)] = (-,0)$. These two-quasineutron configurations are the two lowest possible configurations for the 5$^-$ isomer in ^{168}Yb as discussed later in this section. In terms of the usual Routhian e' versus $\hbar\omega$ diagram as in Figure 2.2, a two-quasiparticle band is formed, for example, by placing one quasiparticle in the orbital A and another in the orbital C. The band configuration would be $(-,1)$. Since A is an $i_{13/2}$ orbital, Coriolis forces should strongly align it with the increased rotation of the core and, consequently, lowering it in energy. This is immediately observed by the sharpness of slope along the orbitals in the e' versus $\hbar\omega$ diagram because the amount of alignment, i, is equal to $-de'/d\omega$.

Using Figure 2.2 two of the possible lowest quasiparticle configurations for the 5$^-$ isomer band in ^{168}Yb are $(-,0)$ and $(-,1)$ as mentioned before. There are two reasons for the choice: 1) correct band parity (negative); and 2) both quasiparticle configurations, $(-,0)$ and $(-,1)$, contain an $i_{13/2}$ quasiparticle that is necessary in order to explain some of the band features like high alignment gain as pointed out previously in this Chapter.

In order to survey the general behavior of the observed quasi-neutron rotational bands in ^{167,168}Yb, it is useful to plot E' (level energies in the rotating frame) versus $\hbar\omega$ as in Figure 4.6. It is readily seen in such a plot that the bands (-,0) and (-,1) are on the average 1.8 MeV above the (+,0), the g.s.b. for ^{168}Yb. As discussed in Chapter II, E' can be further transformed into a relative quantity by using the appropriate reference state, and a relative excitation (e') is obtained more readily. A comparison between the experimental and the theoretical results obtained by the Cranking Shell Model can be performed more easily. In Chapter IV, Section 1, the choice of the reference state, the g-band, was discussed and the values obtained for $\mathfrak{J}_0$ and $\mathfrak{J}_1$ are 33.6 $\hbar\text{MeV}^{-1}$ and 146 $\hbar^3\text{MeV}^{-3}$, respectively. By plotting the experimental Routhian e' versus $\hbar\omega$, as in Figure 4.7, the quasiparticle excitation energy of the rotational bands at different frequencies is easily obtained. By comparing with the theoretical Routhian e' versus $\hbar\omega$ for neutrons (Figure 2.2), it can be seen that all three one-quasiparticle bands are in close agreement with the predicted e' values. Using the additivity rules, the sum of the experimental Routhian e' of the (-,1/2) with the (+, 1/2) bands are approximately equal to the experimental Routhian e' of either the (-,0) or the (-,1) bands. In Table 4.5, the above results are listed according to rotational frequencies. It should be pointed out that the theoretical e' values (from the CSM) lie generally lower than the experimental e' values since the former are calculated with a pair potential, Δ, that is about 20% lower than the full value of Δ obtained from the even-odd mass difference that is used in the
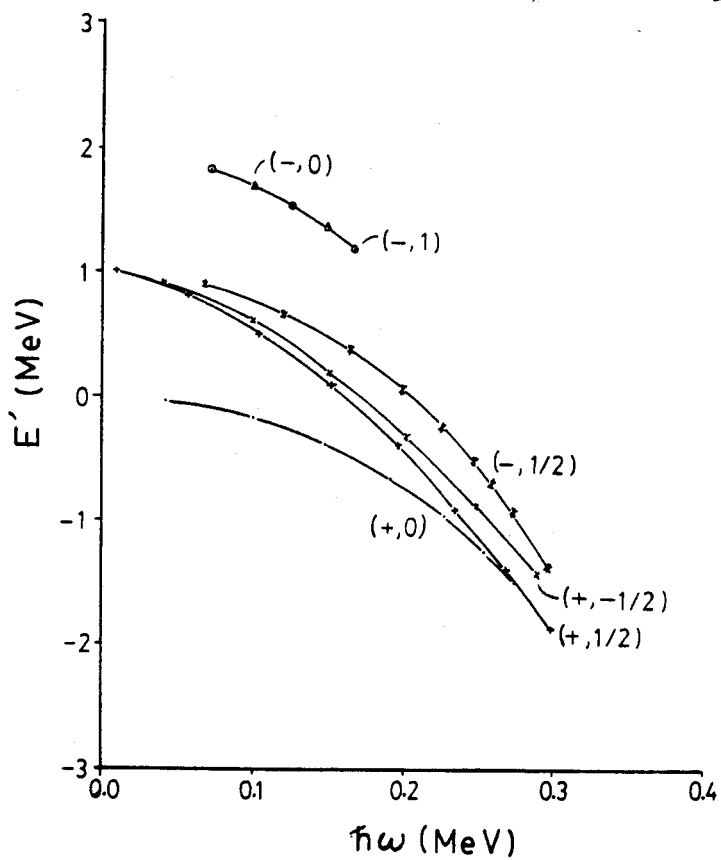
Figure 4.6   Plot of E' (level energies in the rotating frame) versus
ħω for some of the quasiparticle bands related to the
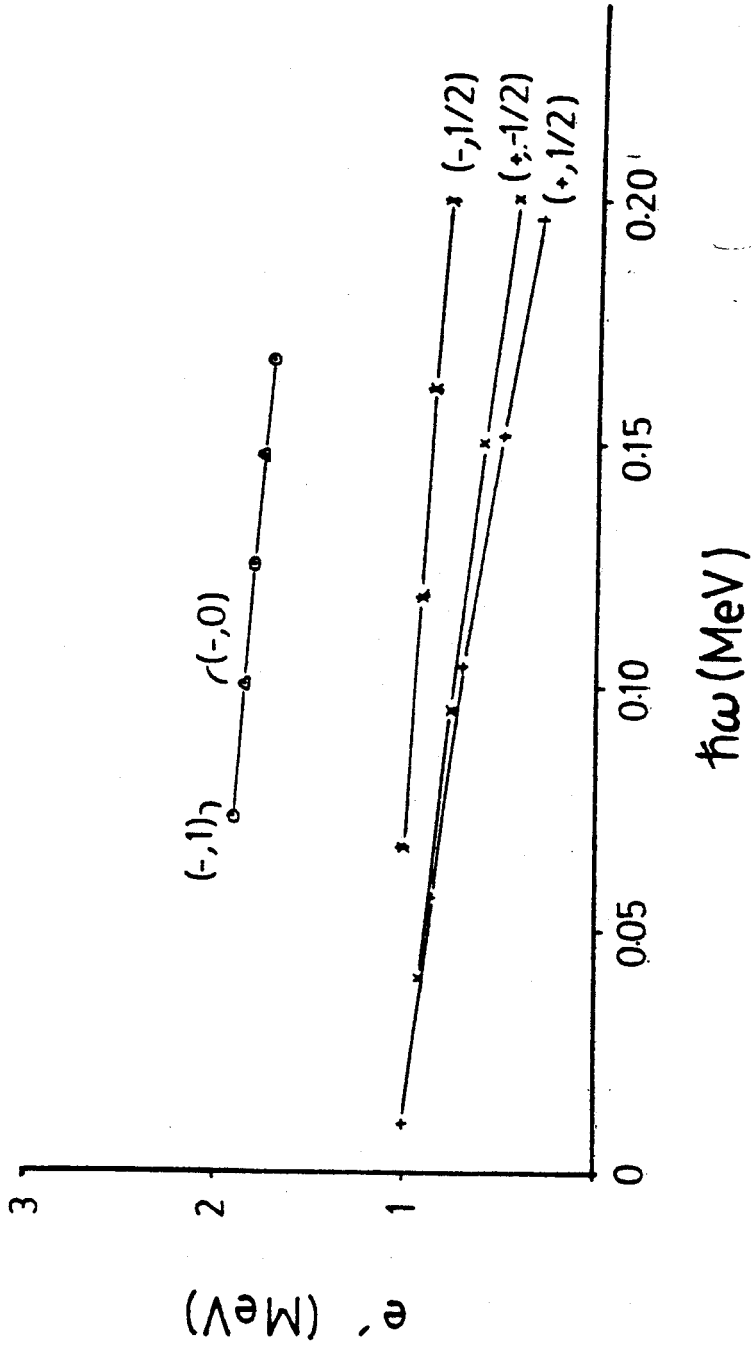observed quasineutron bands in ^{168}Yb.

Figure 4.7   Experimental Routhian e' versus ℏω for observed
quasineutron bands in 168Yb.

TABLE 4.5

Experimental Routhian e' values for the 5⁻ isomer band
in ¹⁶⁸Yb at different rotational frequencies (see Figure
4.7) compared to summed Routhians from ¹⁶⁷Yb.

Quasiparticle Configuration	e' (MeV) at $\hbar\omega$ (MeV)				
	0.08	0.10	0.12	0.14	0.16
[(-,1/2),(+,1/2)]	1.72	1.62	1.52	1.41	1.32
(-,1)	1.88	1.85	1.81	1.76	1.70
[(-,1/2),(+,-1/2)]	1.74	1.65	1.57	1.48	1.40
(-,0)	1.88	1.85	1.81	1.78	--

experimental calculations.

Also, useful information can be obtained by plotting I_x (angular momentum along the rotational axis) versus $\hbar\omega$ (Figure 4.8) since the energy of rotation is ωI_x. It is assumed that the excited rotational quasiparticle bands and the g-band do not differ significantly in collective moment of inertia but in angular momentum at a certain rotational frequency. This difference is called the aligned angular momentum i of the excited band relative to the g-band (Chapter II, Section 3.4). In Figure 4.9, i versus $\hbar\omega$ is plotted for some of the observed quasiparticle bands in ^{167,168}Yb. It is also seen that for both (-,1) and (-,0) bands, the aligned angular momentum i of the two-quasineutron band is much smaller than the value for either [(-,1/2), (+,1/2)] or [(-,1/2), (+,-1/2)] combination at different frequencies (Table 4.6).

The above results indicate then that the theoretical calculations for the Routhian e' are close to the experimental Routhians (Table 4.7) but there is a certain discrepancy for the alignment gain (Table 4.8). It has been pointed out [Rie] that CSM calculations with high-K bands (K > 4) have not been quite effective in predicting the observed band behavior in the rare-earth deformed region, and that more theoretical development is needed in this direction. Additionally, the 5^- isomer band is not a pure quasineutron band, having a small proton admixing. This admixing could be affecting the alignment gain considerably. Unfortunately, proton-neutron admixing has not yet been considered in the literature impeding more reasonable conclusions
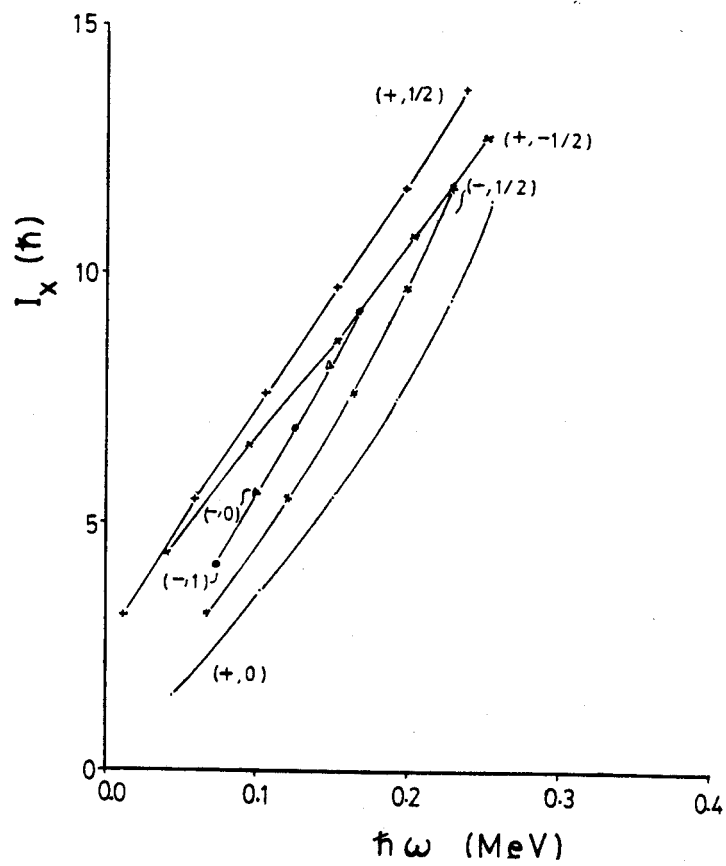
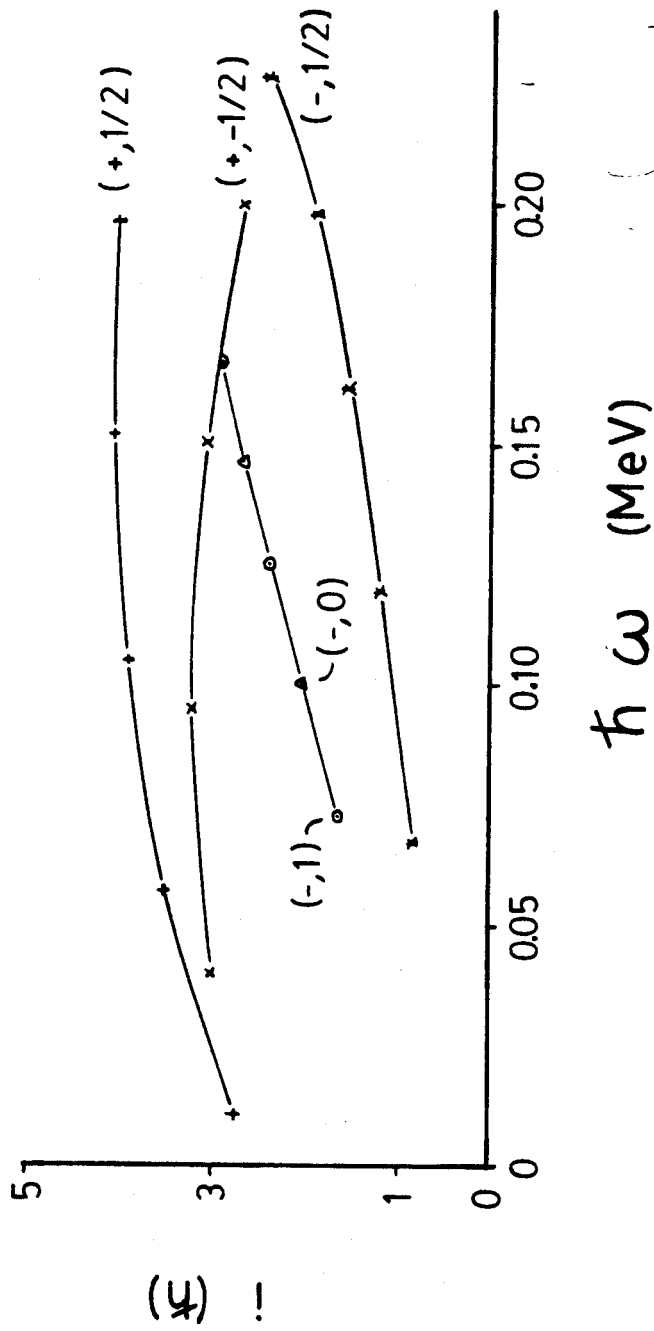Figure 4.8 Plot of I_x versus $\hbar\omega$ for the observed quasineutron bands in ^{168}Yb.

Figure 4.9 Plot of i versus ℏω for the observed quasineutron bands in ^{168}Yb.

TABLE 4.6

Experimental i values for the 5⁻ isomer band in [168]Yb at different rotational frequencies (see Figure 4.8) compared to summed values for [167]Yb.

Quasiparticle Configuration	i ($\hbar$)				
	at $\hbar\omega$ (MeV)				
	0.08	0.10	0.12	0.14	0.16
[(-,1/2),(+,1/2)]	4.62	4.91	5.17	5.39	5.58
(-,1)	1.77	2.05	2.35	2.63	2.90
[(-,1/2),(+,-1/2)]	4.08	4.25	4.38	4.48	4.54
(-,0)	1.77	2.05	2.35	2.63	2.90

TABLE 4.7

Comparison between experimental and theoretical
calculations for Routhian e' (in MeV) as a function
of rotational frequency $\hbar\omega$ for the 5^- isomer in
^{168}Yb.

Quasiparticle Configuration	e' (MeV) at $\hbar\omega$ (MeV)		
	0.074	0.111	0.149
$(-,1)_{theoretical}$	1.89	1.78	1.51
$(-,1)_{experimental}$	1.90	1.83	1.74
$(-,0)_{theoretical}$	1.89	1.79	1.53
$(-,0)_{experimental}$	1.90	1.83	1.75

Note: The theoretical $(-,1)$ and $(-,0)$ results for
^{168}Yb are obtained from the coupling of corresponding
one-quasineutron in ^{167}Yb.

TABLE 4.8

Comparison between experimental and theoretical
calculations for alignment gain i as a function of
rotational frequency $\hbar\omega$ for the 5$^-$ isomer in ^{168}Yb.

Quasiparticle configuration	i ($\hbar$) at $\hbar\omega$ (MeV)		
	0.074	0.111	0.149
(-,1)theoretical	4.23	5.05	5.58
(-,1)experimental	1.66	2.21	2.69
(-,0)theoretical	4.19	4.90	5.26
(-,0)experimental	1.66	2.21	2.68

Obs. The theoretical (-,1) and (-,0) results for
^{168}Yb are obtained from the coupling of corresponding
one-quasineutron bands in ^{167}Yb.

about how it influences alignment gain.

There is hardly any distinction between the (-,0) and (-,1) bands because of the very small signature splitting between (+,1/2) and (+,-1/2) at the measured low frequencies. The (-,1) configuration would seem to be favored because of the lower Routhian of the (+,1/2) component but not enough high spins were observed to make a more definite conclusion.

In summary, the (-,0) and (-,1) two quasineutron configurations are reasonable choices for the 5^- isomer band configuration. The experimental Routhians e' are in close agreement with the calculated theoretical values at low frequencies but the measured i differ somewhat. This deviation is probably due to proton admixing (CSM theoretical calculations for proton admixing have not been considered yet in the literature).

CHAPTER V

CERIUM-128 EXPERIMENTAL DETERMINATIONS

5.1 Gamma-Gamma Coincidences

In order to populate high-spin levels of ^{128}Ce, the Oak Ridge

Isochronous Cyclotron (ORIC) was used to provide beams of ^{20}Ne (6+ charge

state) at about 103 MeV bombarding energy. The reaction used was

^{112}Cd$(^{20}$Ne,4n$)^{128}$Ce, and enriched (98.5%), self-supporting foil targets

of 1.0-1.3 mg/cm^2 thickness were employed.

A preliminary bombarding energy was chosen by making calculations

with the statistical model ORNL computer codes ALICE [P177] and PACE

[Ga80]. The excitation functions obtained from ALICE for the different

reaction channels are shown in Figure 5.1. Similar reactions performed

in this nuclear region by the ORNL Nuclear Structure Group were also

used as a general guideline. The final bombarding energy was chosen by

measuring the excitation functions with a series of nickel degrader

foils (added to a final thickness of 25 micrometers corresponding to

about 7.5 MeV energy loss). To avoid beam spreading and decrease of

intensity, the absorber foils were removed, and the beam energy was

changed to 103.2 MeV, corresponding to the maximum yield in the excita-

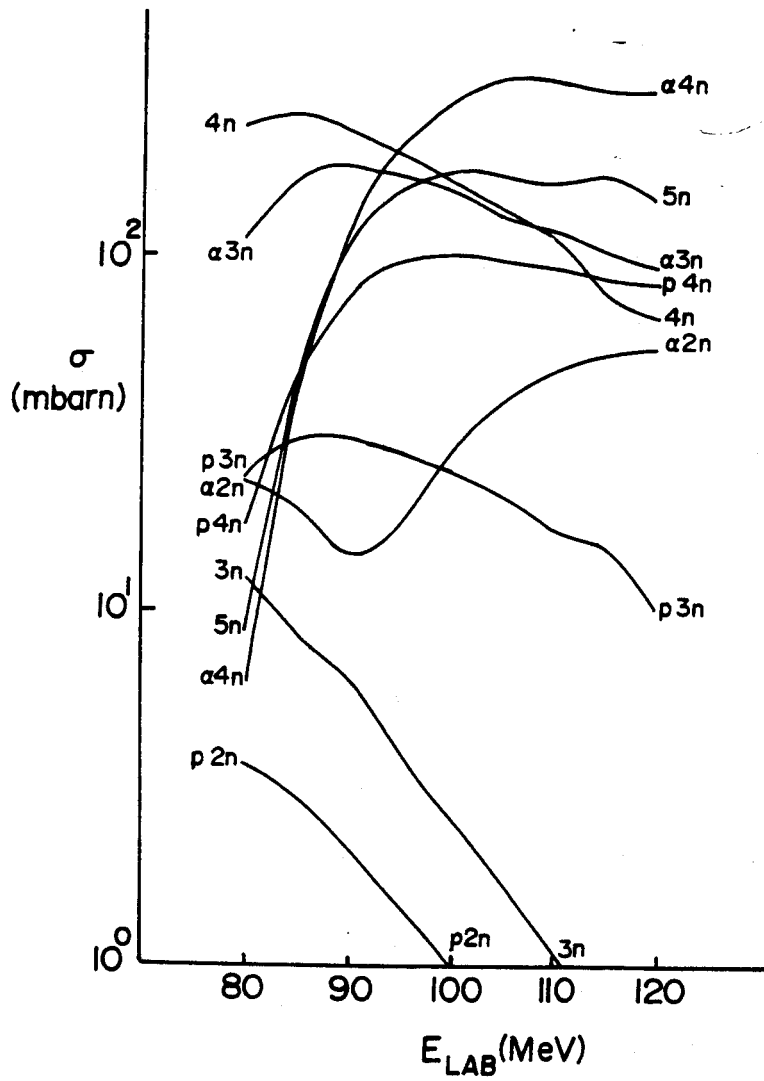tion function. The beam current averaged 4.0 electrical nanoamperes

Figure 5.1   Calculated excitation functions for the bombardment of ^{112}Cd with ^{20}Ne using ALICE.

(namps) and it was fairly constant throughout the experiment.

The difference between the ALICE and the actual experimental values can be expected [Gav] in this region since the optimization of the many input parameters is difficult because both the mass tables used and the Coulomb barrier calculations have been extrapolated for such low masses. The PACE calculations gave even poorer results than ALICE when compared to the bombarding energy of the reactions performed previously in the region.

To make use of the high γ-ray multiplicity [Ri81] of the (Heavy Ion, xn) reactions and to greatly enhance the accumulation rate of coincidence data, seven Ge detectors were placed in the reaction plane (Figure 5.2). Also, two large NaI detectors (25 cm x 25 cm) and (22 cm x 30 cm) were utilized, with one placed above the target and one below to act as a "total (γ ray) energy spectrometer," as explained later in this section. Absorber sheets of lead, tin and copper (23 combinations of sheets, varying in thickness from 102 to 406 micrometers) were placed in front of and around all the detectors to decrease the intensity of x rays, produced by the target material and by the interaction of the evaporated neutrons with the lead beam stopper and absorber foils, and also to decrease the Compton scattering of γ rays between the detectors.

Since the count rate in such an experiment is usually high, considerable care was given in devising a system of analog and digital electronic modules which could handle such counting rates gracefully.
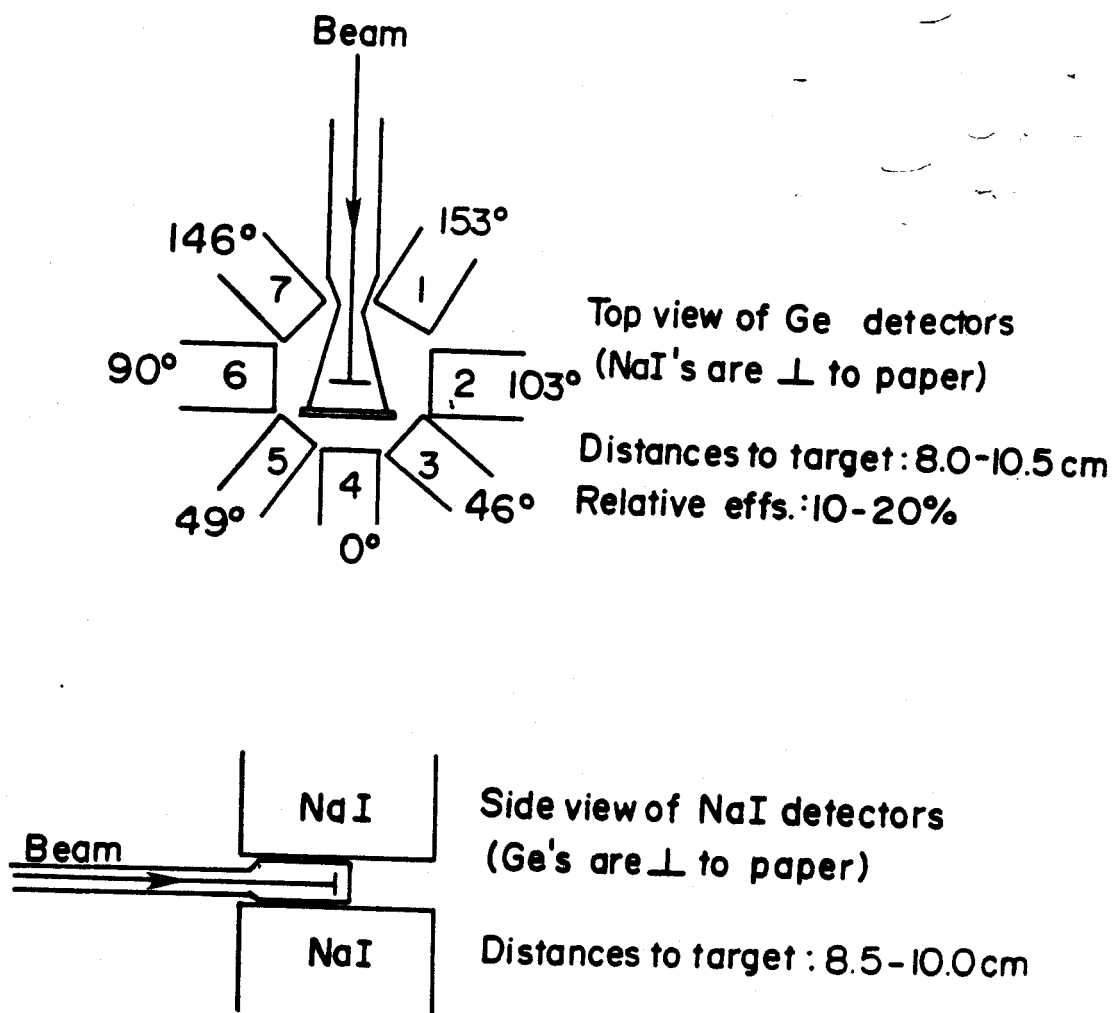
Figure 5.2 Positioning of the Ge and NaI detectors for the bombardment of ^{112}Cd with ^{20}Ne.

A block diagram of the system is shown in Figure 5.3. In general, a coincident event required at least three Ge detectors and one of the two NaI detectors to fire at the same time. The coincident γ rays were required to undergo pulse shaping and timing (about 150 nanosecond windows), multiplicity check (at least four γ rays in a coincident event) and detector "firing" identification (which detectors were "fired"), before they could be fed as an event into a Computer Automated Measurement and Control (CAMAC) crate which passed them along to a Perkin-Elmer 3220 Computer to be recorded on magnetic tapes. One-dimensional projections of energy and time spectra were being accumulated continuously in memory during the experiment and displayed on video monitors, so that problems like changes in amplifier gain and timing could be checked at any time.

More specifically, as far as the data transfer is concerned, the PACE system (which digitized the energy signal of the Ge detectors) sent the data in a digital form to an event handler where event-by-event match (through machine language) of the PACE system to the CAMAC/Perkin-Elmer system could be done. In the Perkin-Elmer 3220 Computer, an Acquisition Task called HAC [Mi81a] continuously read the data, by block (8192 bytes) transfer and wrote them onto magnetic tape for later off-line analysis. Also, a histogramming task called DISMO [Mi81b] was used to display the data on a video terminal during the data acquisition (see block diagram in Figure 5.4).

An important factor was the dead time of the system, which came mainly from the software of the acquisition task HAC because it had to
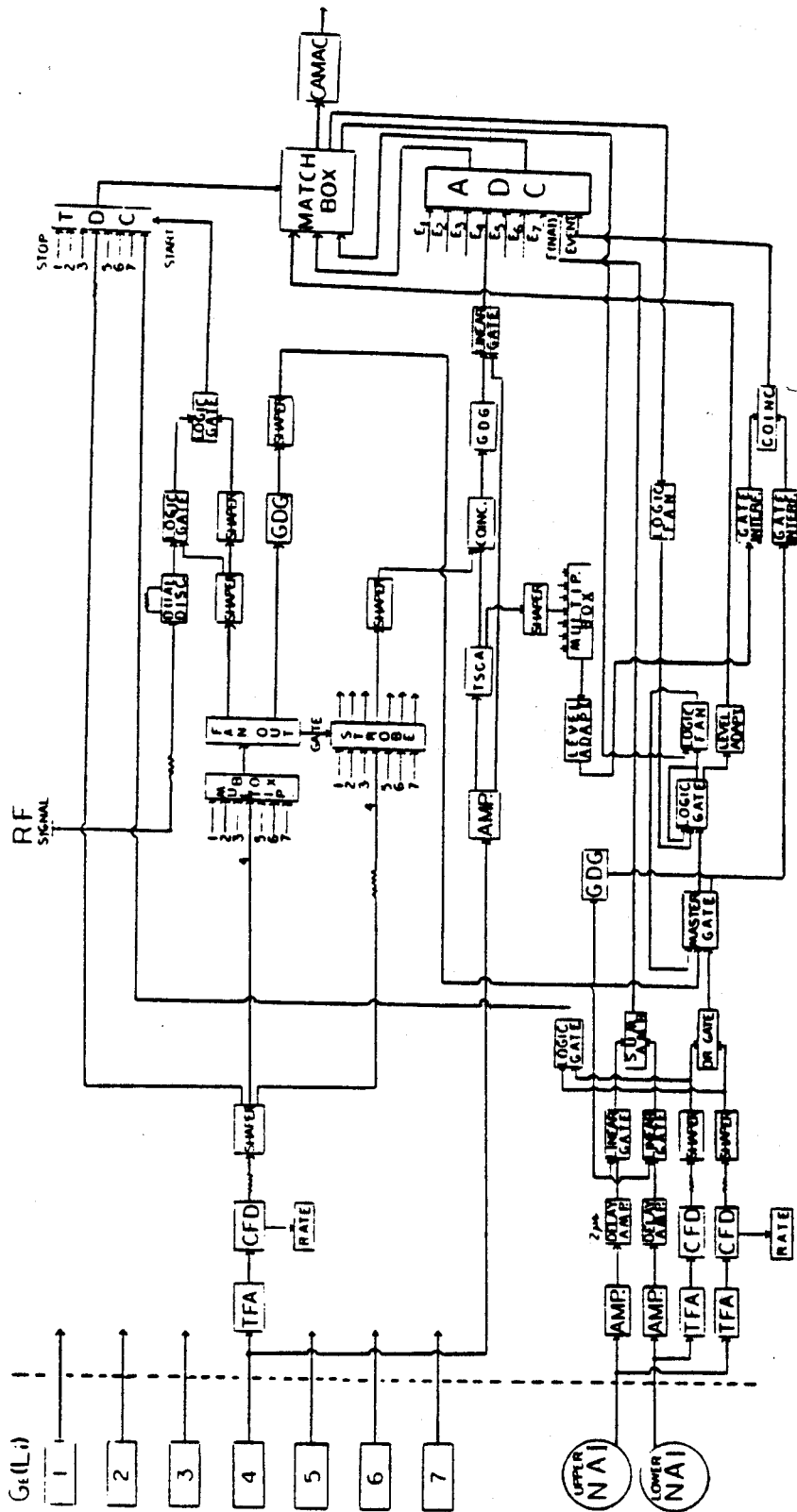
Figure 5.3 Block diagram of the experimental setup for the bombardment of ^{112}Cd with ^{20}Ne.
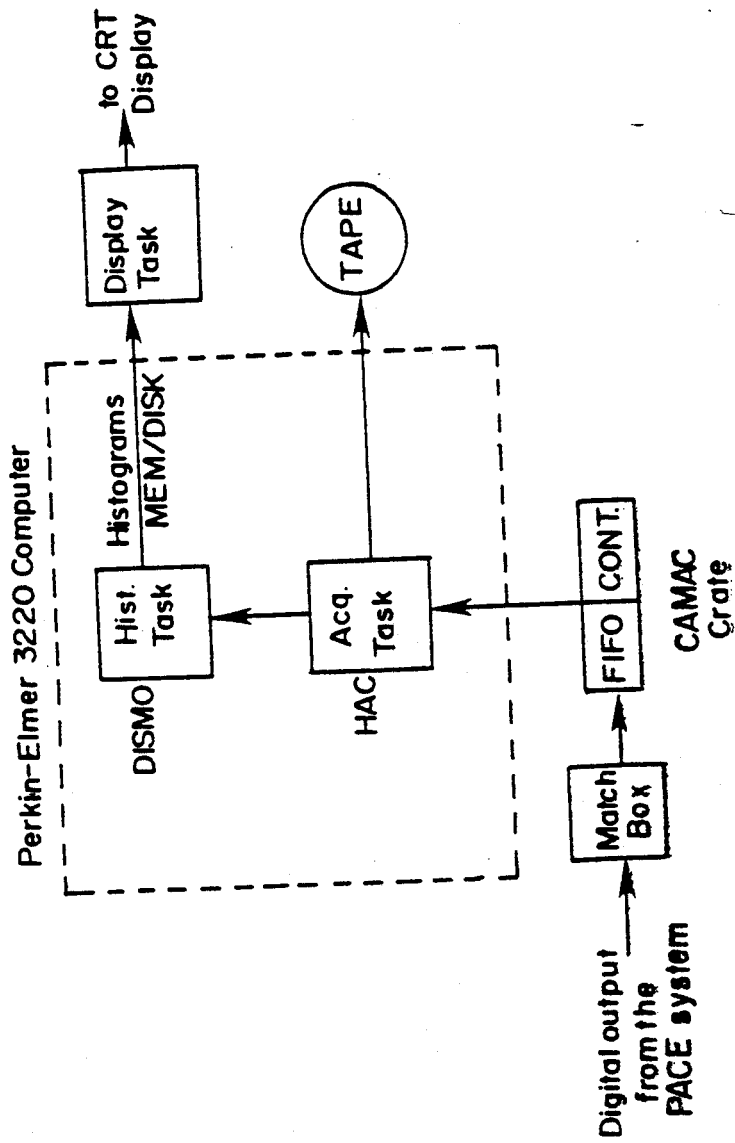
Figure 5.4   Block diagram for the data transfer from the experimental area to the Perkin-Elmer 3220 computer.

delete the extra information recorded by the PACE system that was not needed by the Perkin-Elmer system. The information coming from the PACE system consisted of a string of 24-bit words with each energy parameter corresponding to a word. Each word was composed of the data in bits 1-13, the stretcher (consequently, the detector) ID in bits 14-16, a "No True" flag in bit 17, and zeros in bits 18-24. The "No True" flag indicated if the data in the word were indeed part of the event or not. HAC then identified the flag and placed zeros in the data bits whenever the "No True" flag was set, therefore reducing the number of useful bits to 16 which corresponded to the stretcher (Ge detector) ID and the data. This restructuring of the data set the upper limit on the dead time of the system as a whole. The coincidence event count rate was approximately 2 kHz, while the average count rate for the NaI detectors was around 80 kHz and for the Ge detectors was about 8 kHz.

The total γ ray energy spectrometer is used in order to select the appropriate 4n-reaction channel since the light Ce isotopes are in a mass region that is highly defficient in neutrons, and therefore, the emission of protons and α-particles for the compound nucleus (for the reaction used in this experiment, ^{132}Ce is such compound nucleus) becomes large enough to compete effectively with the 4n-reaction channel. The use of the spectrometer in this experiment can be described as follows. A series of rapidly emitted γ rays causes a pileup in the collection of charges in the NaI detector. The end result is a pulse out of the detector that is proportional to the sum

of the energy of all the γ rays (total γ ray energy) in the series.
The reaction channels had broadened Gaussian distribution that peaked
at different total γ ray energies, and in this experiment, these NaI
detectors were used to discriminate against different reaction
channels. The energy window was set between 2 and 12 MeV. A total
(γ ray) energy spectrum is shown in Figure 5.5, where the range of the
5-, 4- and 3-particle reaction channels is shown approximately. The
broad peak around 3 MeV comes mainly from the 4n reaction channel. In
Table 5.1 are shown all the final reaction products observed.

TABLE 5.1

Final reaction products observed in the bombardment
of ^{112}Cd with a 103.2-MeV ^{20}Ne beam

5-particle	Final product	4-particle	Final product	3-particle	Final product
5n	^{127}Ce[b]	4n	^{128}Ce[a]	3n	^{129}Ce[c]
α4n	^{124}Ba[c]	α3n	^{125}Ba[b]	α2n	^{126}Ba[b]
p4n	^{127}La[a]	p3n	^{128}La[d]	p2n	^{129}La[c]
2p3n	^{127}Ba[c]	2p2n	^{128}Ba[b]	2pn	---

[a] Strong channel
[b] Medium channel
[c] Weak channel
[d] Probably observed
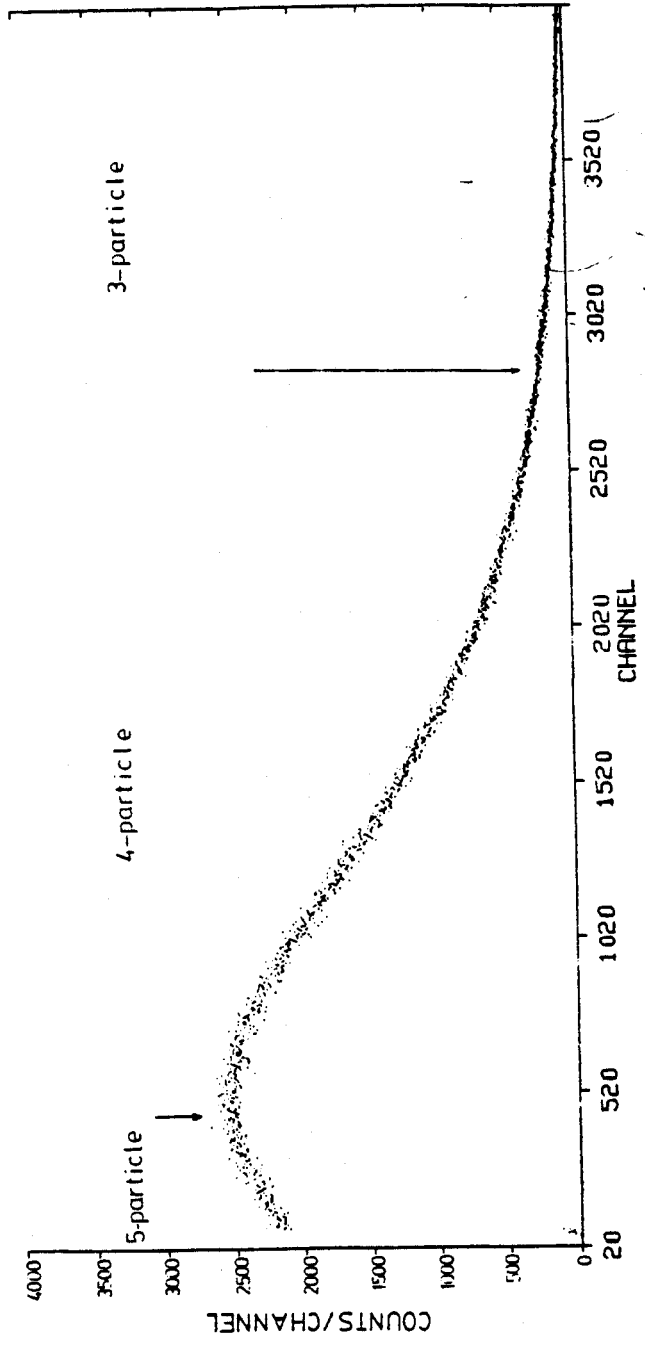Note: Other combinations of particles are not preferred as a reaction
channel.

Figure 5.5   Total (γ ray) energy spectrum for the bombardment of ^{112}Cd with ^{20}Ne.

At the end of the coincidence experiment, 79 magnetic tapes of data were obtained with an average of three million coincidence pair events per tape. In the off-line analysis, one sorting program [Ow81a] was used to "crunch" and perform a preliminary ordering of the recorded data according to the "firing" sequence of the detectors. Also, only prompt events contained in the 4-particle reaction channel slice of the total energy spectrum were sorted out. The "crunching" and preliminary ordering were done by extracting from the event word structure (eighteen 16-bit words corresponding to the energy and time information of the seven Ge detectors and one NaI detector, plus begin- and end-of-event tags) the energy and the ID of the detectors "fired" and by rewriting this information on a new magnetic tape as a 32-bit word with its own ID. These new tapes are called "pre-scanned" tapes, and they can be used in a variety of ways that fall outside the scope of this work.

The coincidence data were translated into a two-dimensional energy matrix by a scanning program [Ow81b] which was used on the "pre-scanned" tapes where each 32-bit word had its energy information extracted and corrected for gain shift. The 2-D matrix is obtained by taking the $[\gamma_1, \gamma_2]$ double-coincidence event and placing it in an E_i vs. E_j energy grid as a b_{12} event. By requiring at least three Ge detectors to "fire" together, the number of double-coincidence events in the matrix is tripled because there are three different combinations of two detectors. Therefore three b_{ij} matrix points are obtained out of one triple-coincidence event. In the classical two-detector

experimental setup only one b_{ij} matrix point is obtained out of one double-coincidence event.

To improve the statistics, the two-dimensional energy matrix was further folded onto itself around the 45-degree axis. By projecting the two-dimensional spectrum on one axis, the total projection spectrum was obtained. This spectrum contains all the counts (or coincident events) that were recorded during and sorted after the experiment. On this total projection spectrum, all energy gates corresponding to the γ rays of interest were determined. By gating on a γ ray along one of the axes of the energy matrix and projecting on the other axis, all γ rays in coincidence with it were obtained in the projected spectrum. For example, an energy gate placed on the γ ray corresponding to the $2^+ \rightarrow 0^+$ transition should show all the γ rays that are in coincidence with it (Figure 5.6).

Of primary importance is the correction of coincidence counts arising from the background lying underneath each gating transition in the total projection spectrum. Each γ-ray peak in the total projection spectrum lies on top of a background made up mostly of Compton scattered quanta coming from high-energy continuum γ rays. Therefore, it is necessary to subtract this continuum contribution from the gated spectra. The technique used involved the construction of a Master Background spectrum which was subtracted from each gated spectrum. This Master Background was obtained by placing gates in different regions of the total projection spectrum, where there are no peaks,
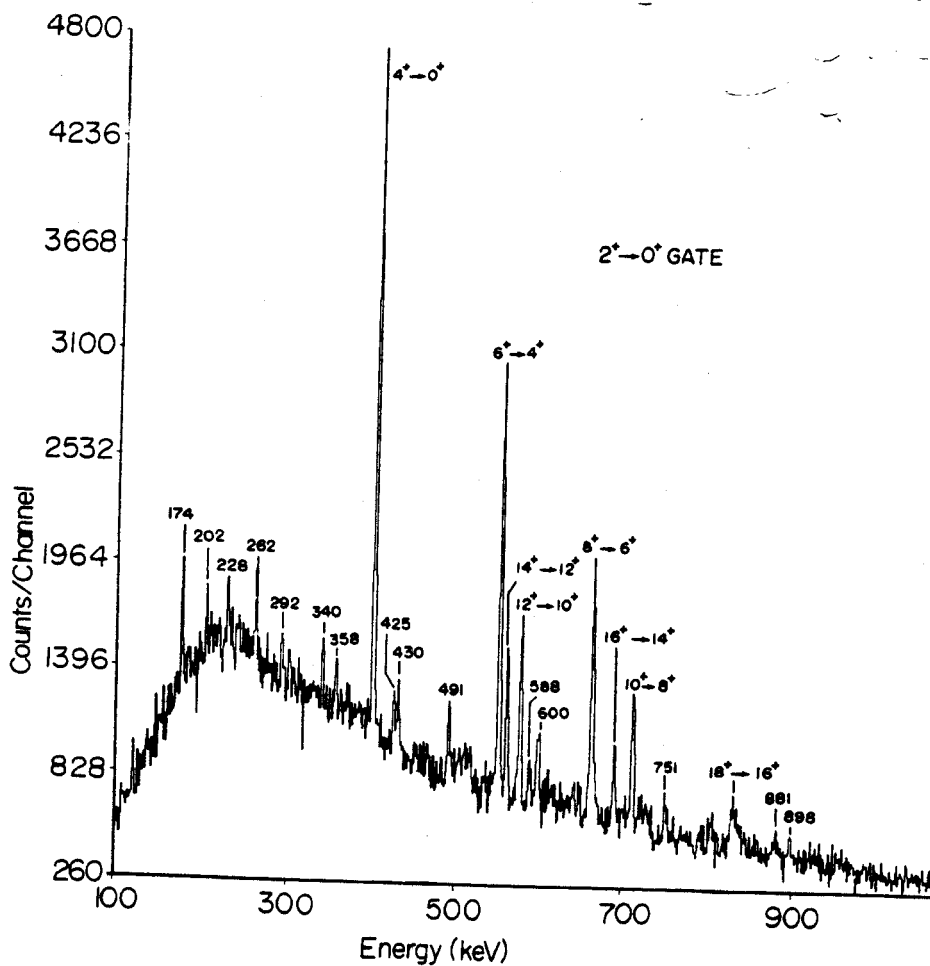
Figure 5.6   The $2^+ \rightarrow 0^+$ gate spectrum for ^{128}Ce obtained in the γ-γ coincidence experiment.

and summing them together. A gated spectrum was obtained by multiplying the Master Background spectrum by a factor that is proportional to the background area underneath the gated peak and subtracting it from the gross gated spectrum.

In the analysis of the gated spectra, the computer code SAMPO was used for energy calibration in a similar manner, as described previously in Chapter III, Section 1, and the interactive computer code SPASM [Mi81c] was used for determining the peak areas. The intensity calculations were done by using the sum of angle-weighted efficiencies of all Ge detectors. The angle correction described in Section 2 of this chapter was used as the weighting factor for the efficiencies. The bulk of the analysis was done with SPASM because its interactive nature made "instant" and quick analysis much easier to perform than the slower SAMPO. The maximum difference in peak areas between SAMPO and SPASM was about five percent. This value is comparable to variations in peak areas caused by small shifts in determining the background level underneath a peak.

5.2 Angular Distributions

The difference in angular distributions of $\Delta \ell = 1,2$ γ-ray transitions can be used, together with the general trends of sideband structure and feeding in this nuclear region, to place the transitions in the decay scheme. Therefore, angular distribution experiments can be very useful in determining the decay scheme and complement the

coincidence results.

The classical experimental setup was described in Chapter III, Section 3, but a slightly different arrangement was used here. This consisted of using the multi-Ge array already in place and taking "singles" spectra in all detectors simultaneously, as opposed to taking "singles" spectra one angle at a time. A major problem encountered was the limited disk memory space of the PACE system. In order to circumvent this, three similar computers located in different areas of the laboratory were used. The Perkin-Elmer computer could not be used because it cannot build histograms at the high rates encountered in this experiment.

In the off-line analysis many problems that were not perceived at the time of the experiment were found to be a hindrance in trying to understand the data. One of the problems was that the "singles" spectra were very complex due to the many reaction channels present in the experiment (Figure 5.7). Also, Doppler shifting and Doppler broadening of the photopeaks were problematic because in some cases they caused overlap of peaks.

Extracting individual peak areas from multiplets is a quite difficult task when there is Doppler broadening of the peaks. This is especially true when there are small peaks (e.g., the uppermost yrast and side-feeding transitions) which lie close to large peaks. These small peaks, which in many instances are the most interesting ones, very often lay underneath multiplet envelopes, giving rise to very
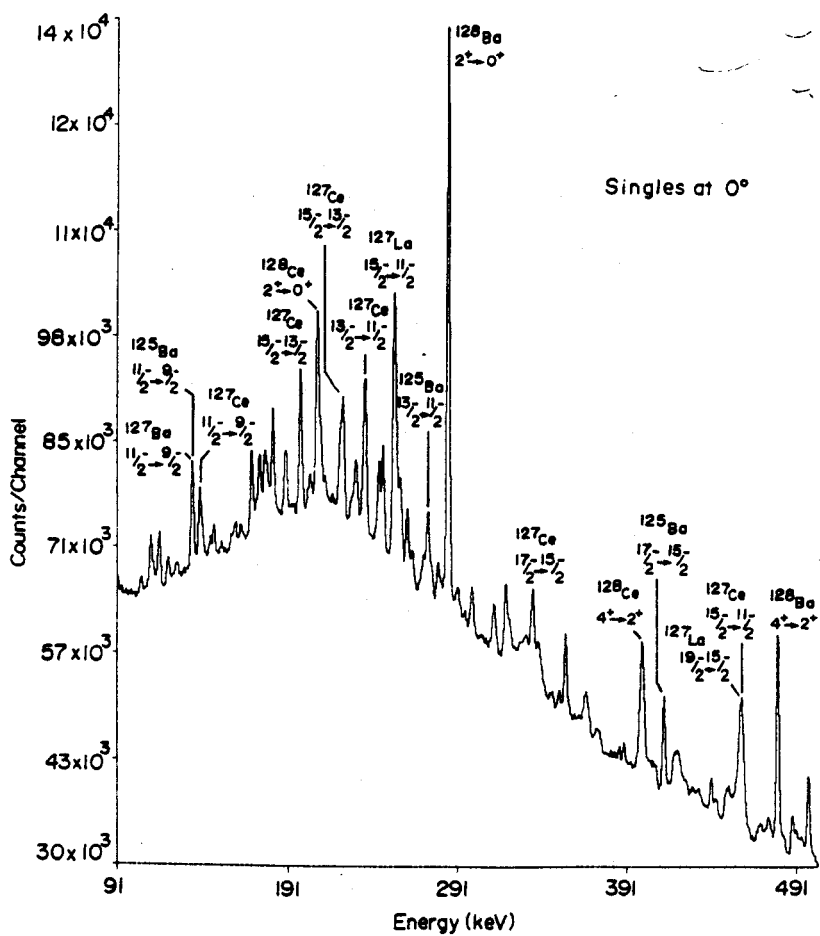
Figure 5.7   "Singles" spectrum of 0° for the bombardment of [112]Cd with [20]Ne.

large errors in the extracted areas. Most of the large peaks observed in the "singles" spectra came from the lower yrast transitions of the 4-particle reaction channel.

Since adequate quantitative results could not be obtained from the "singles" spectra, other analytical paths can be employed. One possible initial way of treating the data consists of using the coincidence data and doing a "one-detector" sorting, i.e., choosing an individual detector and summing up, in an energy spectrum, all events considered coincident with the other detectors. For example, detector 1 might be taken as the individual detector and all events registered in detector 1 which were in coincidence with detector 2 were summed up to the coincident events with detector 3, and so on. The resultant spectrum would be the corresponding "singles" spectrum at the angle of detector 1 and will be referred to as "groupie". This is pictorially shown below.

Individual Detector: 1

                                   Ge Detectors

Coincident events of: 1 ↔ 2

                               + 1 ↔ 3

                               + 1 ↔ 4

                               + 1 ↔ 5

                               + 1 ↔ 6

                               + 1 ↔ 7

                        ————————————

"singles" spectrum at angle 1.

Seven "groupies" were obtained in this manner, corresponding to the angles of the seven detectors. After efficiency corrections, the intensities for the individual γ rays were plotted versus angle to obtain an angular distribution. The angular distribution plots shown in Figure 5.8 correspond to some of the most intense yrast transitions, where it can be seen that the distributions do not have the classical shape for $\Delta \ell = 2$, E2 transitions. The multiplicity of the reaction imposes a complexity on the angular distribution that is difficult to surmount, but this behavior can be possibly explained in the following manner. The 4-fold multiplicity required that three γ rays (corresponding to the Ge detectors) were in approximately the same spatial plane, and therefore an angular correlation among them is implied in a coincident event. Consequently, a triple angular correlation would have to be determined for every coincident event, which is a quite difficult and laborious software problem.

Further corrections are made for the system efficiency, using well-known transitions such as the yrast E2 transitions shown in Figure 5.8. This is done by obtaining an averaged distribution curve over several theoretical E2 transitions and normalizing the experimentally known E2 distributions to it. That is, in the first step the theoretical angular distribution equation for partial alignment is calculated by using the following equation,

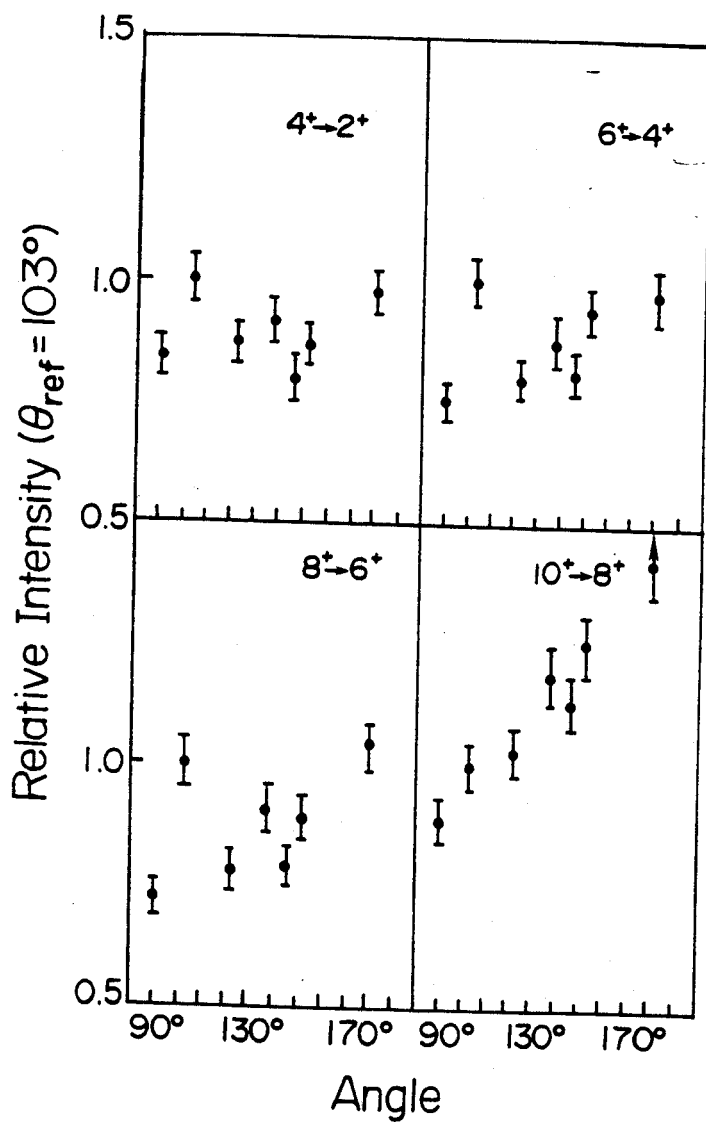$$W(\theta) = 1 + a_2 A_2^{max} P_2(\cos \theta) + a_4 A_4^{max} P_4(\cos \theta) , \quad (5.2.1)$$

Figure 5.8 Angular distribution curves for several ground state rotational band transitions in ^{128}Ce.

where A_i^{max} is the angular distribution coefficient for the total spin alignment. The attenuation coefficients a_i (specifies the amount of alignment of the nuclear states) are averaged over several nuclear states at a constant partial spin alignment, and the angular distribution coefficients for partial alignment are calculated by

$$A_i = a_i A_i^{max} \quad . \quad\quad\quad (5.2.2)$$

The resultant theoretical angular distribution equation becomes

$$W(\theta) = 1 + A_2 P_2 (\cos \theta) + A_4 P_4 (\cos \theta) \quad . \quad\quad (5.2.3)$$

Figure 5.9 shows the theoretical distribution obtained in such a manner. In the next step, an average of the intensities of several yrast transitions was calculated at each angle, and an average experimental angular distribution was obtained. The correction factors were then obtained by dividing, at each angle, the average theoretical over the average experimental value. These correction factors were used on all experimental distributions, and corrected experimental A_2's and A_4's were obtained. The corrected experimental A_2's and A_4's determined in this manner are shown in Table 5.2.

A check on the validity of the method can be carried out by examining the angular distributions of known dipole transitions derived from odd-A nuclei produced in this experiment and by comparing them with the quadrupole transition distributions. They should have different angular distributions (Figure 5.10) and therefore different coefficients.
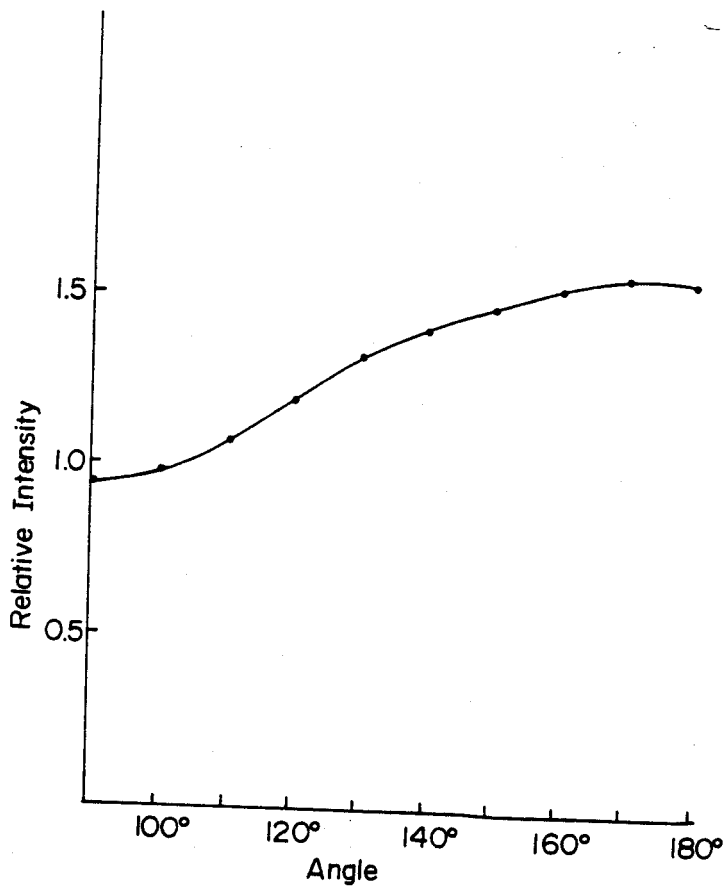
Figure 5.9 Theoretical angular distribution using an average of several theoretical E2 transitions.

TABLE 5.2

Corrected experimental A_2's and A_4's for observed transitions in ^{128}Ce.

E_γ (keV)	Angular Distributions Coefficient		Assignment
	A_2/A_0	A_4/A_0	
400	0.24(4)	-0.11(5)	$4^+_g \rightarrow 2^+_g$
551	0.31(4)	-0.11(5)	$6^+_g \rightarrow 4^+_g$
662	0.34(4)	-0.84(56)	$8^+_g \rightarrow 6^+_g$
711	0.52(6)	-0.14(8)	$10^+_g \rightarrow 8^+_g$
577	0.43(10)	-0.28(14)	$12^+_g \rightarrow 10^+_g$
561	0.46(16)	-0.11(4)	$14^+_g \rightarrow 12^+_g$
202	-0.48(17)	-0.14(15)	a
222	-0.26(10)	-0.20(10)	^{127}Ce
272	-0.61(12)	-0.18(9)	^{125}Ba
355	0.18(10)	-0.08(13)	a
425	-0.25(17)	-0.18(17)	(2245.6 keV) $\rightarrow$ (1820.5 keV)
491	0.54(10)	-0.30(14)	(2736.3 keV) $\rightarrow$ (2245.6 keV)
751	0.20(8)	-0.41(11)	(3766.9 keV) $\rightarrow$ (3678.9 keV)
857	0.58(12)	-0.09(16)	

[a] No level assignment
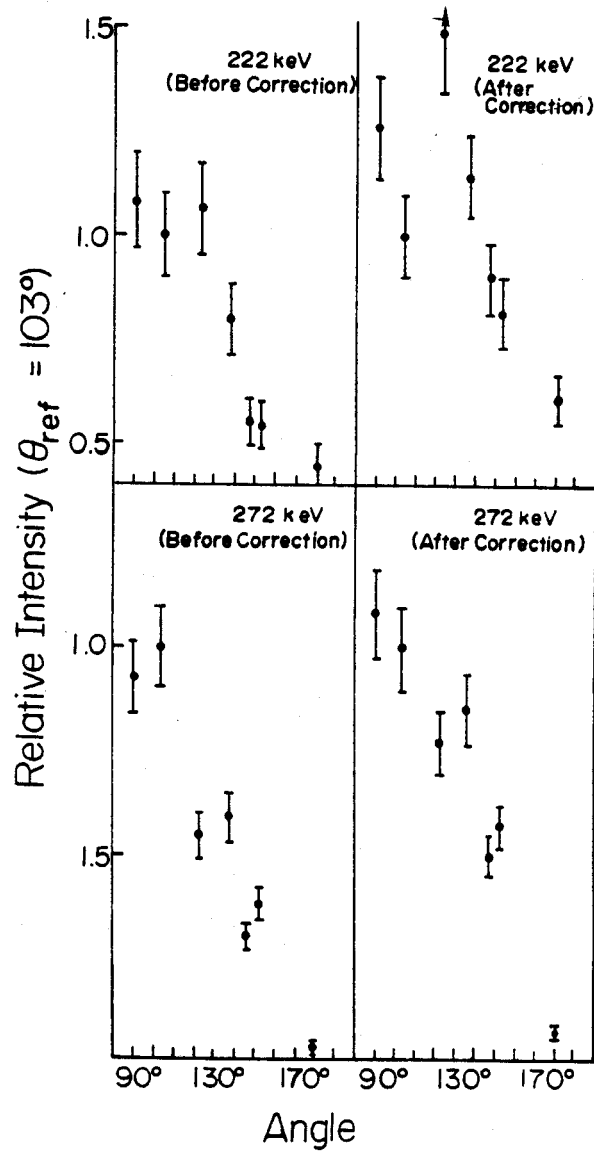
Figure 5.10 Angular distribution curve for some $\Delta\ell = 1,2$ transitions in ^{128}Ce.

The dipole transitions used come from ^{127}Ce (222 keV) and ^{125}Ba (272 keV), and, for the latter, experimental angular distribution coefficients have been determined previously [Gi78]. As shown in Table 5.3, the coefficients obtained in the present experiment are in close agreement with those shown by Gizon.

TABLE 5.3

Angular distribution coefficients for the M1 transition $13/2^- \to 11/2^-$ in ^{125}Ba.

E_γ (keV)	Angular Distribution Coefficient		Reference/ this work
	A_2/A_0	A_4/A_0	
272	-0.742(10)	0.095(6)	[Gi78]
272	-0.61(12)	-0.20(10)	this work

CHAPTER VI

CERIUM-128 EXPERIMENTAL RESULTS

6.1 The Yrast Band

The yrast states of ^{128}Ce have been observed previously [Wa75] up to 16^+, and the first backbend was found to exist in the vicinity of the 10^+ and 12^+ states. In this study, it was possible to extend the yrast band up to spin 22^+ and possibly to 24^+. In addition, two side-bands were also observed (see next sections). A level scheme for ^{128}Ce is drawn in Figure 6.1.

In order to observe such high spin states, it is first necessary to bring enough angular momentum into the compound system to assure population of such states. By using a 103-MeV ^{20}Ne beam, around 45 $\hbar$ of angular momentum is made available to the compound nucleus. Since ^{132}Ce, the compound nucleus, is neutron-deficient and far from the line of beta stability, charged particle emission can compete effectively as a reaction channel. This competition leads to the partitioning of the total cross section among the different reaction channels and consequently decreases the population of the desired reaction product [Mo76]. Using a heavier projectile such as ^{40}Ar to produce the same first reaction product would not necessarily mean that even higher spin yrast states could be populated [Mo76], as
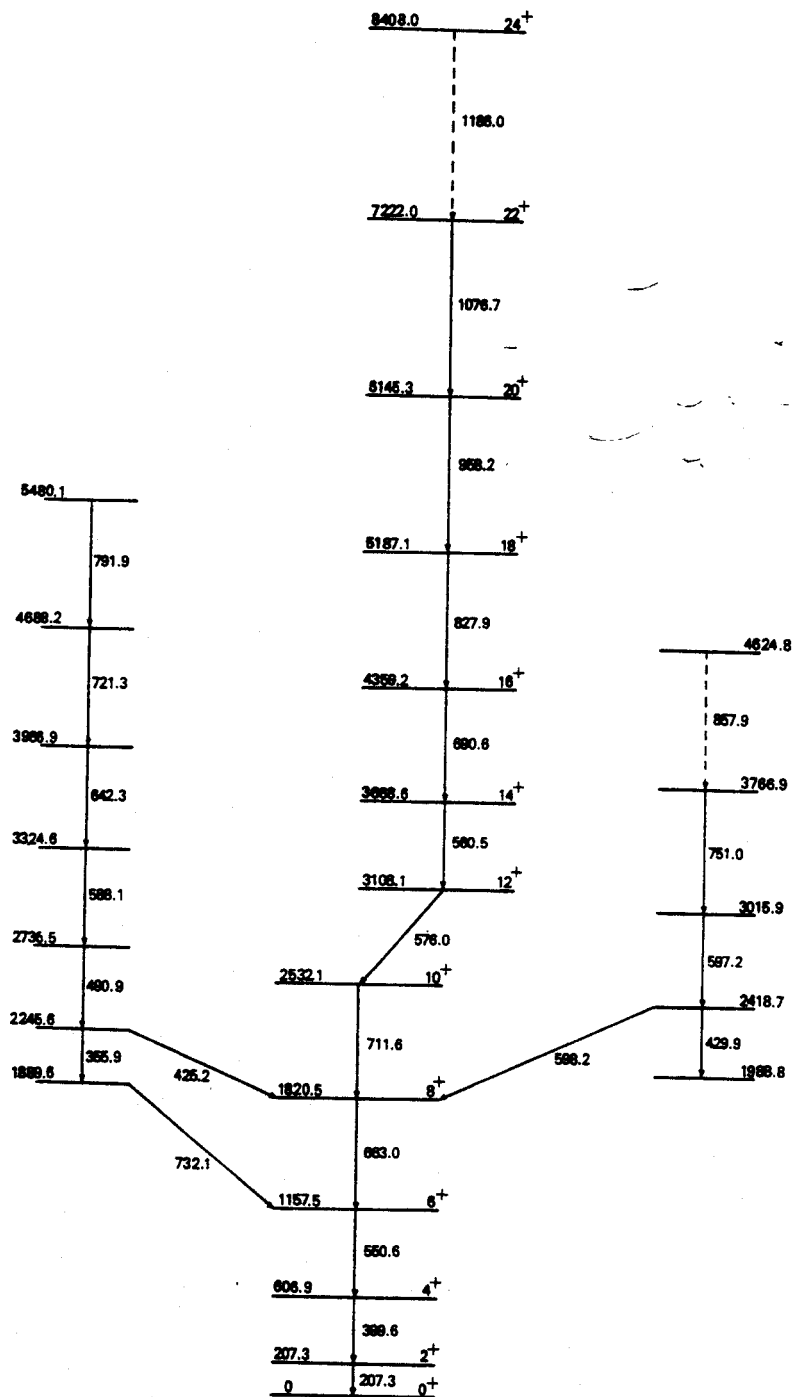
Figure 6.1 Level scheme for ^{128}Ce.

noted previously for ^{128}Ce [Ha81]. The (^{40}Ar,4n) reaction will popu-
late a continuum region different from that produced in the (^{20}Ne,4n)
reaction (about 50 $\hbar$ of maximum input angular momentum for 140-MeV
^{40}Ar beam [Wa67]), but its yrast cascade entrance channels turned out
to be the same as for the ^{20}Ne reaction. This is because some of the
populated excited levels in the continuum tend to decay through a
series of collective bands lying above, but roughly parallel to, the
yrast line via fast I→I-2 E2 transitions, in contrast to the decay
through M1 transitions that will enter the yrast line at higher
spin states [Mo76]. Thus, the competition between the E2 and M1 tran-
sitions along the decay paths in the (^{40}Ar,4n) reaction resulted in a
similar entrance point in the yrast cascade for both ^{20}Ne and ^{40}Ar
projectiles. In Figure 6.2, a schematic decay path from the continuum
to the yrast line is drawn for the ^{112}Cd (^{20}Ne,4n) ^{128}Ce reaction.

By making use of the known yrast transitions [Wa75] and the total
coincidence spectrum (Figure 6.3), appropriate γ-γ coincidence spectra
were selected for a determination of the uppermost yrast transitions.
The "12$^+$-gate" spectrum (the spectrum gated on the 12$^+$ → 10$^+$ transi-
tion), as well as the 14$^+$-gate and the 16$^+$-gate spectra, clearly
showed the γ-ray peak corresponding to the 18$^+$ → 16$^+$ transition
(Figure 6.4). In addition, each of these gates showed a more poorly
defined peak, corresponding to the 20$^+$ → 18$^+$ transition. When the
intensity of the yrast transition versus energy was plotted, the
intensity of the γ-ray peak corresponding to the 18$^+$ → 16$^+$ transition
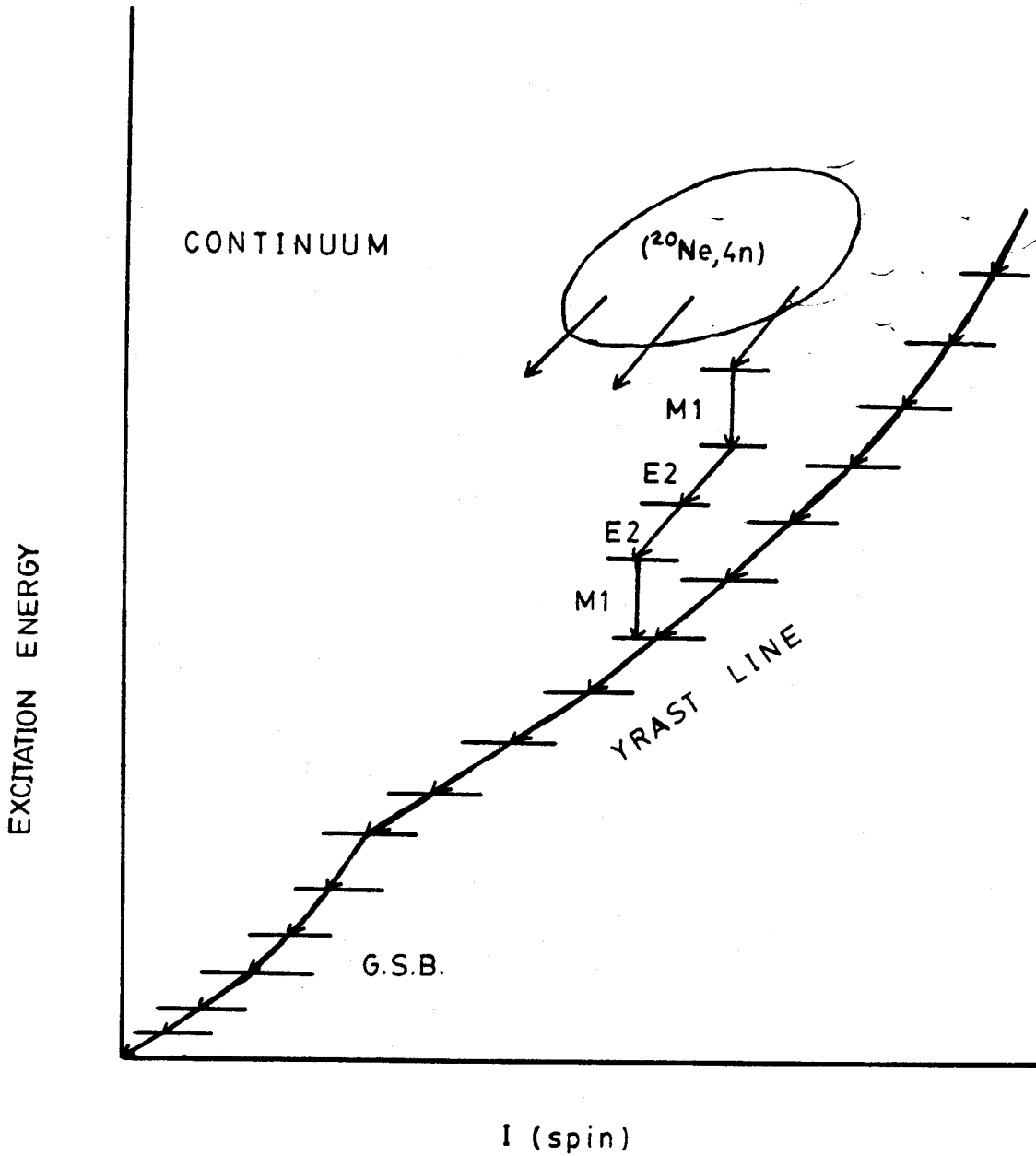followed the general downward trend expected in this coincidence
spectrum.

Figure 6.2   Schematic diagram for one possible decay path
             for the continuum into the yrast line for
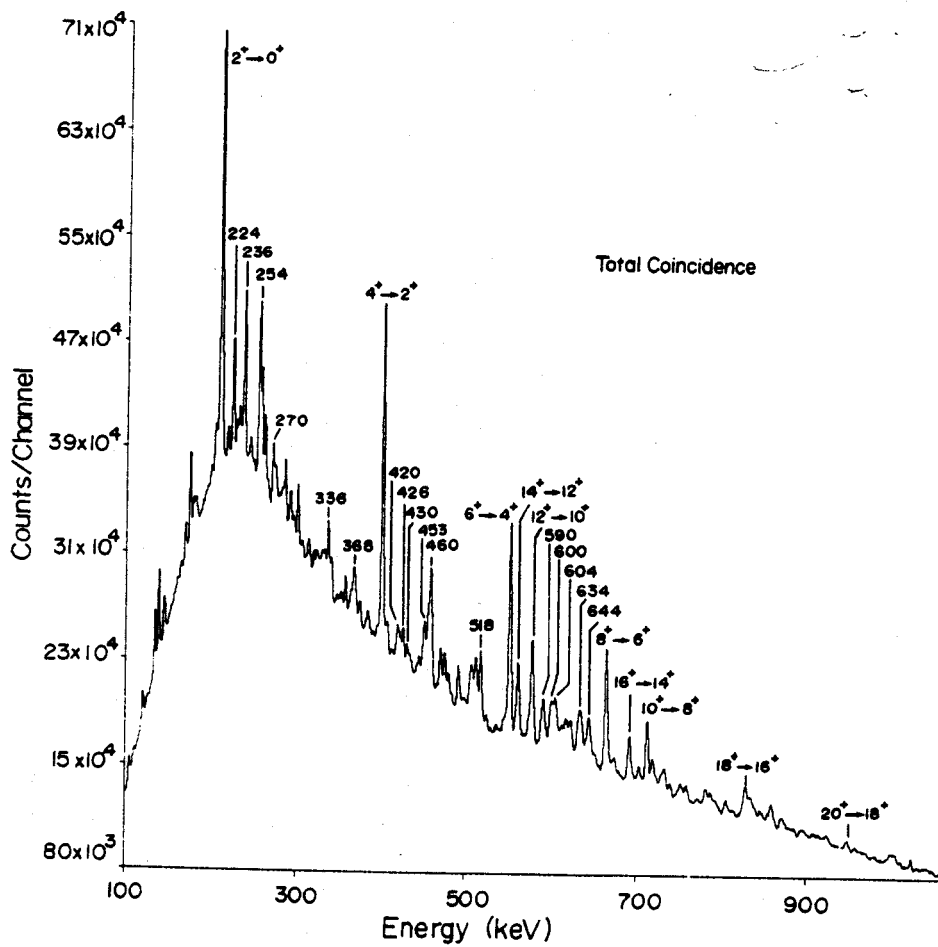   the $^{112}Cd(^{20}Ne,4n)^{128}Ce$ reaction.

Figure 6.3 Total coincidence spectrum for the bombardment of ^{112}Cd with ^{20}Ne using a 4-particle total energy gate.
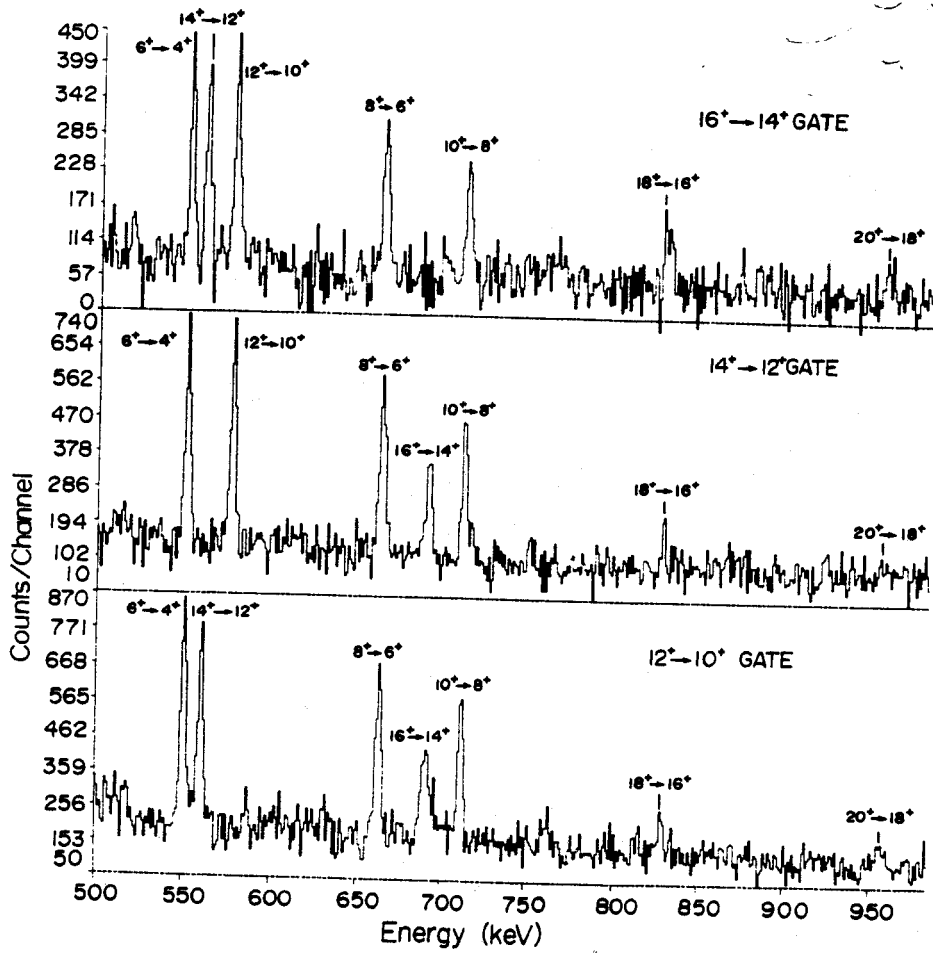
Figure 6.4 The $20^+ \rightarrow 18^+$ and $18^+ \rightarrow 16^+$ transitions observed in some gated spectra in ^{123}Ce.

Another widely used technique is the summing of all the gated spectra of the yrast transitions producing a "sum spectrum" that will enhance all peaks, especially those that appear only weakly in the gated spectra (Figures 6.5 and 6.6). From the "sum spectrum", the intensity of the yrast transitions can be obtained and plotted as a function of spin. In Figure 6.7 such a plot shows that the new transitions fit the general pattern of the yrast cascade intensities as indicated by the smooth downward trend.

Some of the newly observed yrast transitions can be further confirmed by studying the gated spectra of these γ rays. The 18^+-gate clearly shows the yrast transitions, while in the 20^+-gate these transitions are barely seen (Figure 6.8). For the 22^+- and 24^+-gates, the yrast cascade cannot be clearly distinguished from the background. These peaks are on top of a large background and are only two to three percent larger in counts per channel than the background, making the error on the background subtraction comparable to the number of counts in the peaks. The angular distribution for the $18^+ \rightarrow 16^+$ transition, as seen in Figure 6.9, displays a general upward trend indicating the $\Delta \ell = 2$ multipolarity of the transition. The large error bars reflect the rather poor statistics found in the corresponding γ-ray photopeak.

Since there were many reaction products, the existence of doublets, triplets, and even quadruplets was common in the total coincidence spectrum. This created an enormous difficulty in the analysis, since many gates of interest were contaminated with interfering reaction products. Very few of the yrast gates were "clean" of
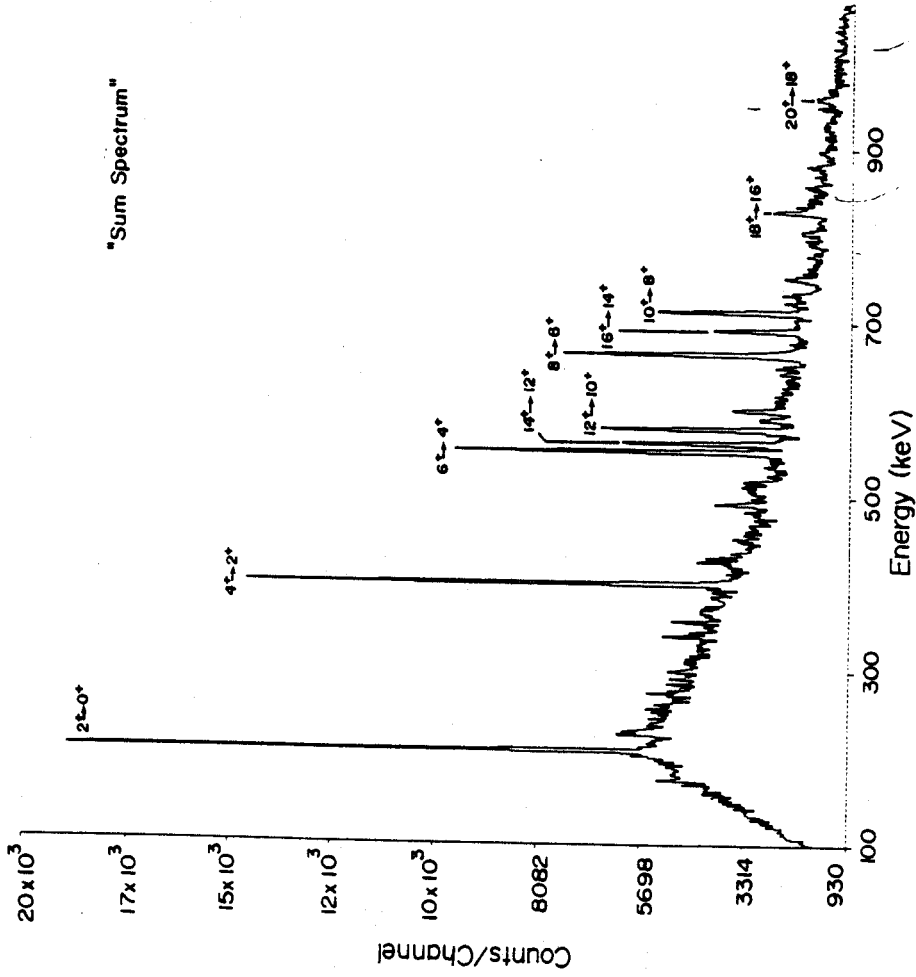
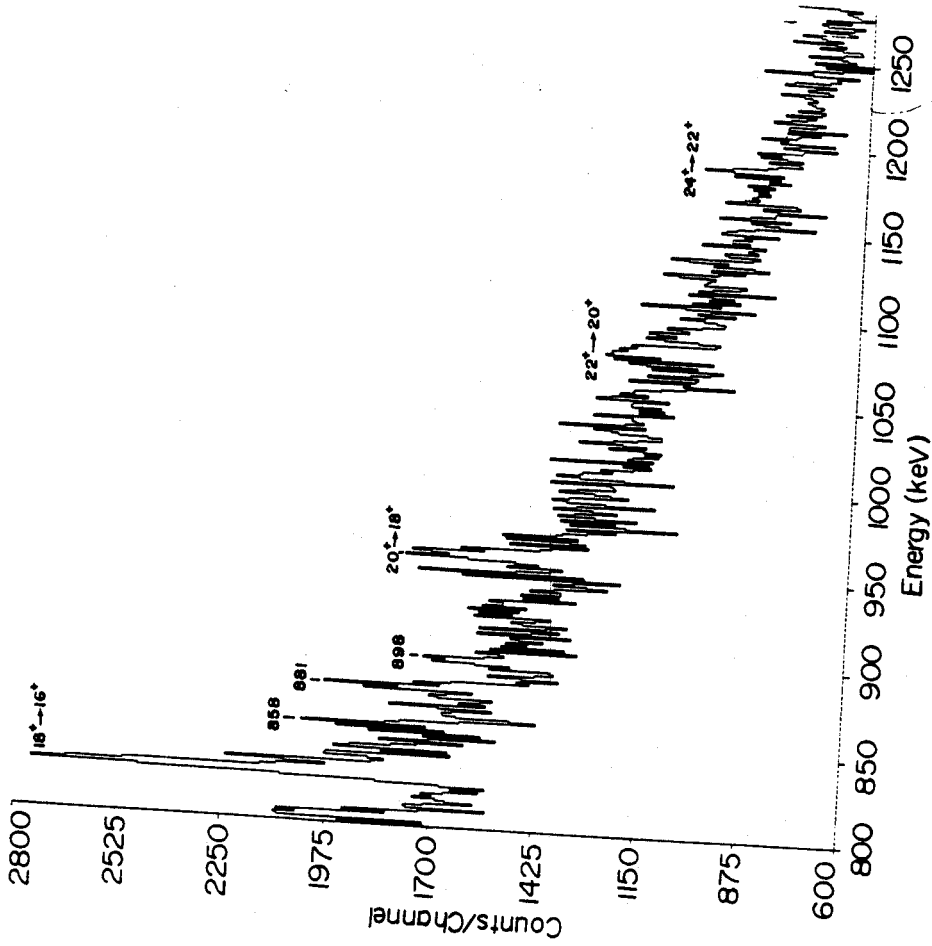Figure 6.5 "Sum spectrum" for the ^{128}Ce coincidence experiment.

Figure 6.6 Expanded portion of the "Sum spectrum" showing the new yrast transitions (marked with an asterisk).
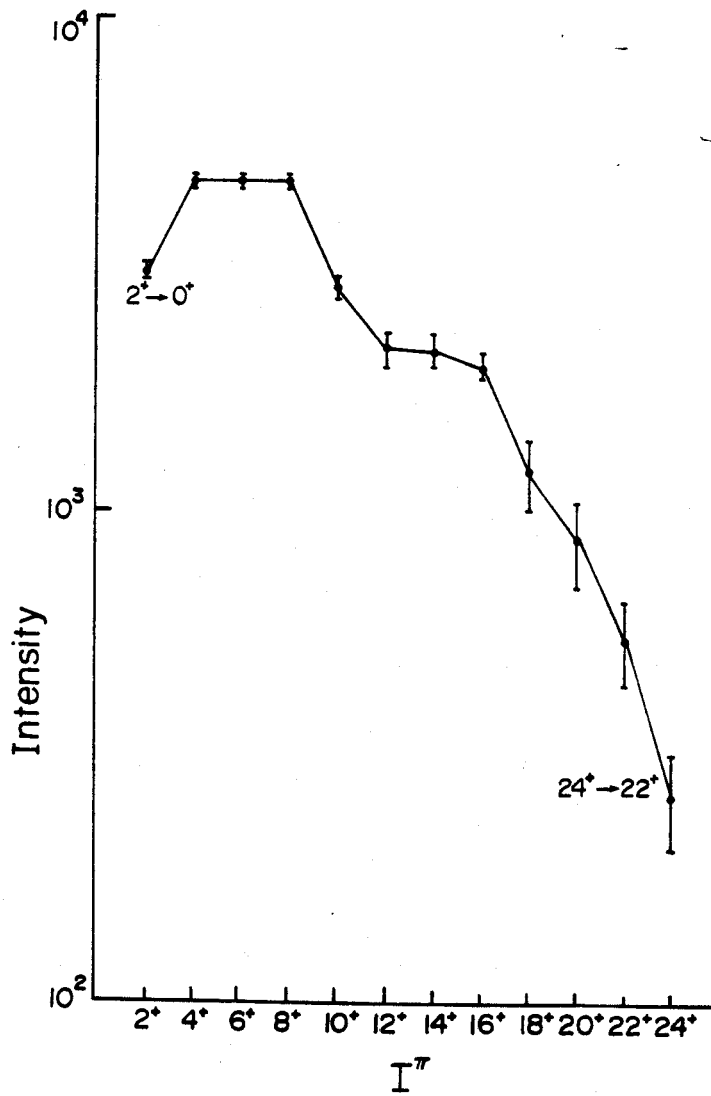
Figure 6.7 Intensity for the yrast transitions versus
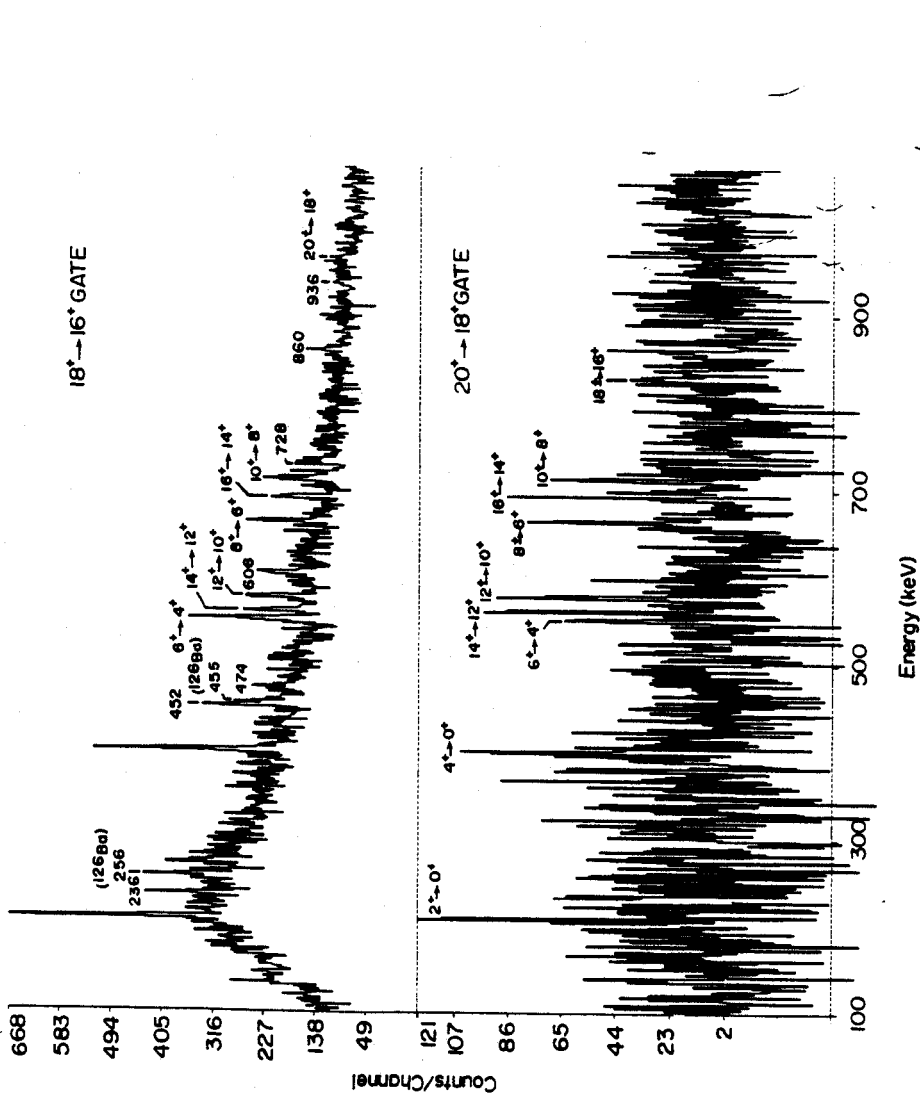I^π from the "Sum spectrum".

Figure 6.8 The $20^+ \rightarrow 18^+$ and the $18^+ \rightarrow 16^+$ gated spectra
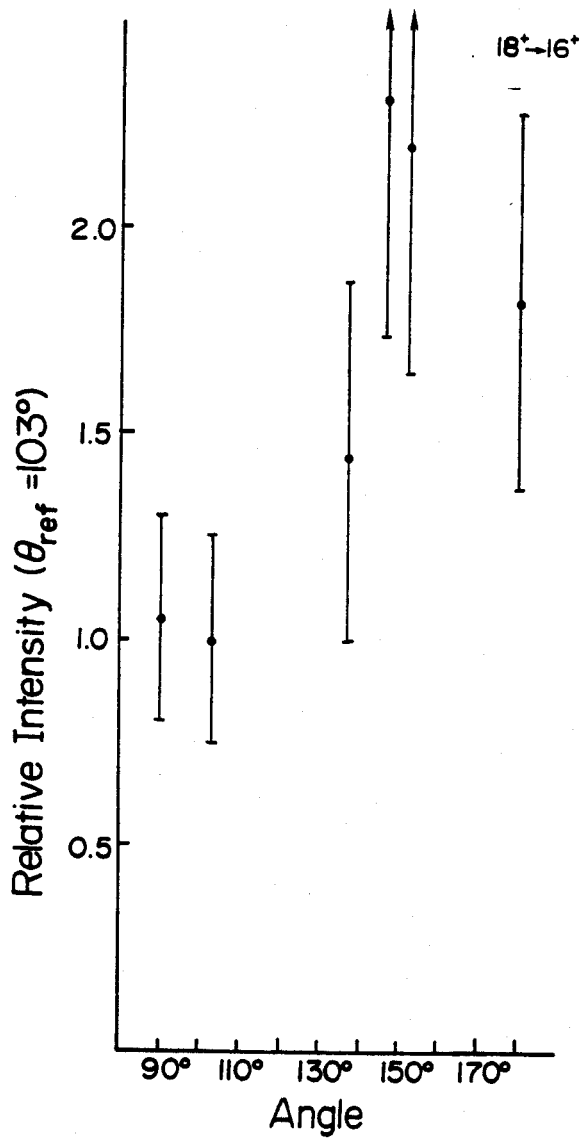from the ^{128}Ce coincidence experiment.

Figure 6.9   Angular distribution for the $18^+ \rightarrow 16^+$ yrast transition.

contaminants, as can be seen in Figure 6.10. To better ascertain and evaluate such interferences, any peak of interest in the total coincidence spectrum was sliced in several ways in order to enhance the coincidence information from each of the components in the complex multiplets. The multiplet of γ rays lying within the gate set on the $12^+ \rightarrow 10^+$ transition (see Figure 6.10) was cut into 570-572, 573-575, and 576-580 keV slices and the corresponding three coincidence spectra are shown in Figure 6.11. It can be seen that the 230-, 422-, 694-, and 764-keV transitions are contaminant lines that are enhanced in the 576-580 keV slice. These are the ground state rotational band (g.s.b.) transitions in ^{124}Ba [Co74], and appeared strongly in the $12^+ \rightarrow 10^+$ (577 keV) gate in ^{128}Ce because the $6^+ \rightarrow 4^+$ transition of ^{124}Ba is of the same energy.

The ^{128}Ce isotope displays a strong backbend between spins 10^+ and 12^+ as seen in a classical $2\mathfrak{J}/\hbar^2$ versus $\hbar^2\omega^2$ plot (Figure 6.12). The occurrence of the backbending would indicate that the interaction between the g- and s-bands is small. In a phenomenological analysis, this interaction becomes smaller with increasing number as indicated by the sharpness of the backbend from ^{128}Ce to ^{134}Ce.

The $^{128-134}$Ce isotopes are situated near the neutron closed shell N=82. This implies that these isotopes could be in a transitional region between prolate-deformed to spherical shape. In reference [De74] it was stated that the ratio B(E2, $4^+ \rightarrow 2^+$)/B(E2, $2^+ \rightarrow 0^+$) for the g.s.b. indicates that ^{134}Ce is in a transitional region while ^{130,132}Ce behave like (permanent) deformed nuclei. The rotational
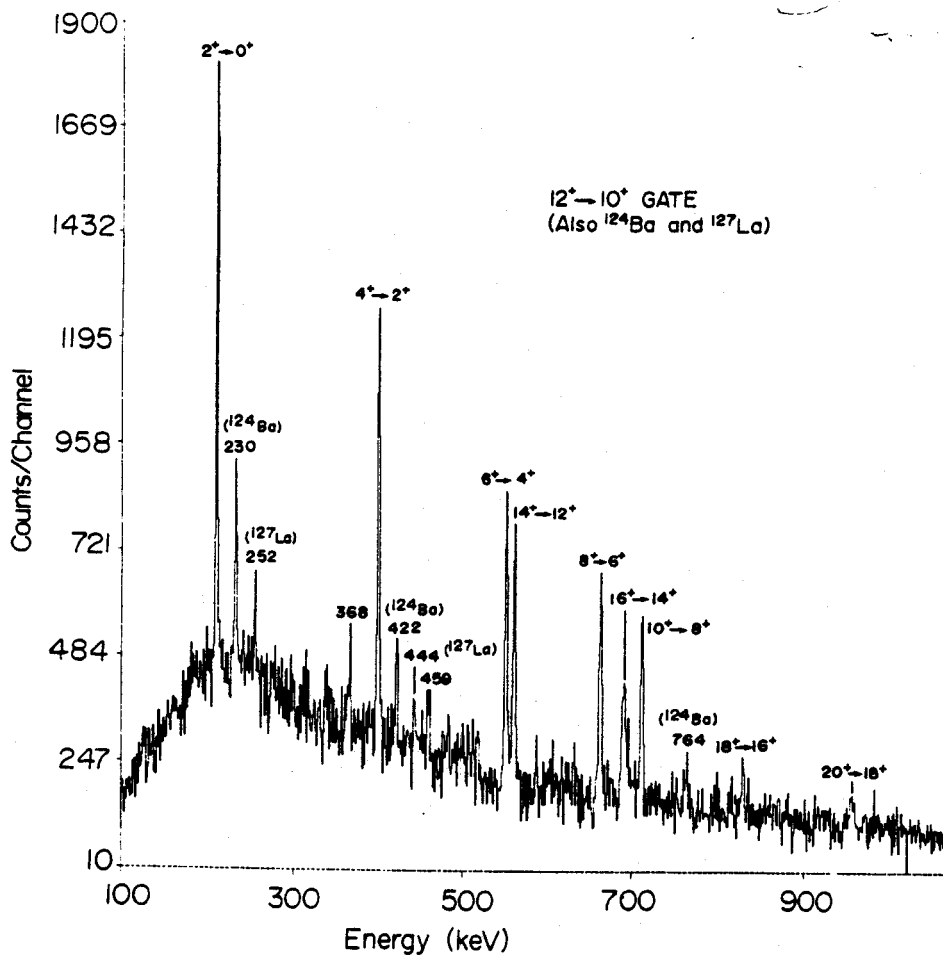
Figure 6.10   Spectrum gated on the $12^+ \rightarrow 10^+$ transition in ^{128}Ce.
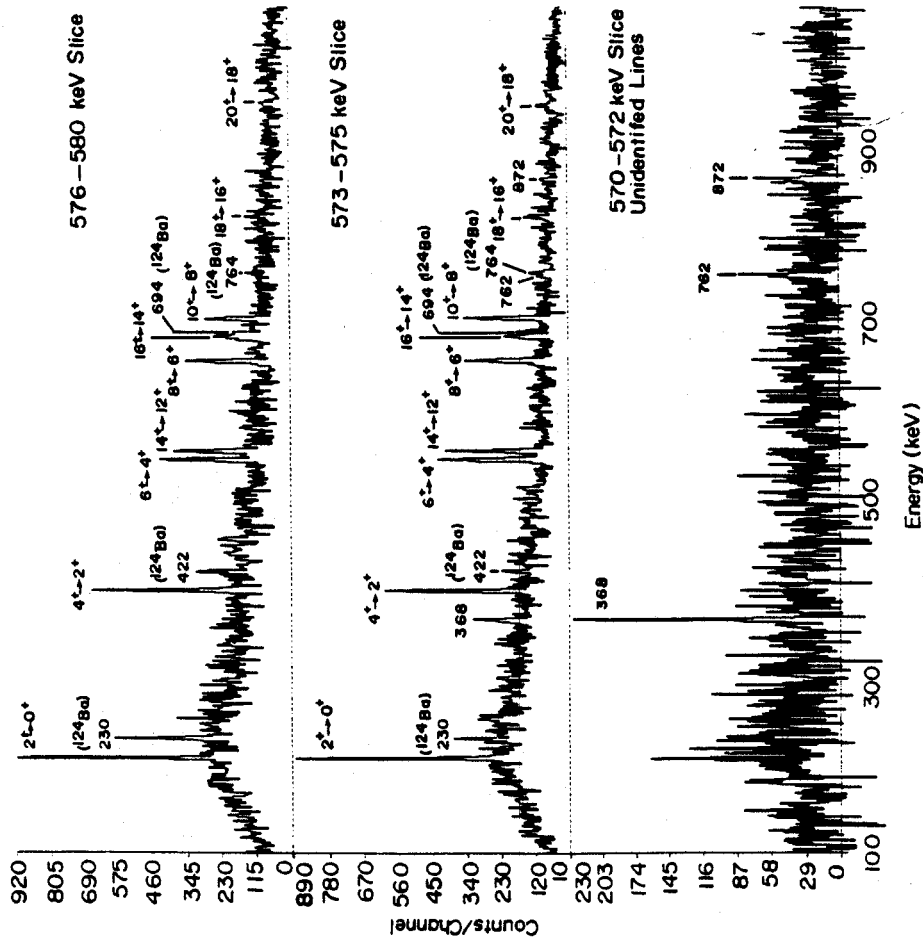
Figure 6.11 Different energy slices of a multiplet in the total coincidence spectrum for the ^{128}Ce coincidence experiment.
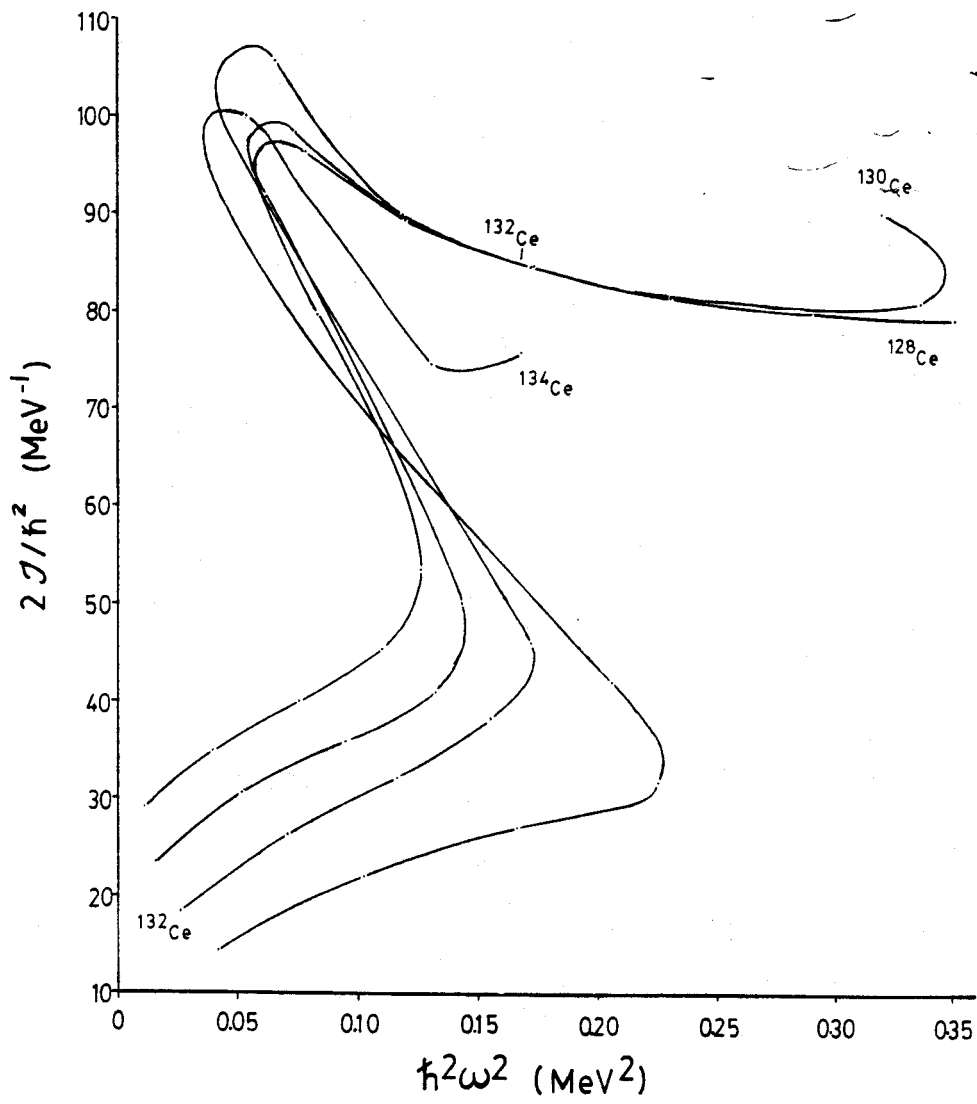
Figure 6.12 Plot of $2\mathcal{J}/\hbar^2$ versus $\hbar^2\omega^2$ for $^{128-134}$Ce.

behavior of the $^{128-134}$Ce isotopes are readily observed by the level sequences as in Figure 6.13 where E_I (level energy) versus $I(I+1)$ is plotted. It can be seen that the yrast band displays rotational behavior both before and after the backbending region.

The different deformation among the Ce isotopes is further deduced from the increase in energy of the first excited 2^+ states as neutrons are added. (The $2^+ \rightarrow 0^+$ transition energy increases from 207 keV for ^{128}Ce to 409 keV for ^{134}Ce.) In addition, with increasing neutron number the measured lifetimes for the first 2^+ levels of the $^{130-134}$Ce isotopes [De74] decrease indicating that the heavier Ce isotopes are less deformed. The arguments above can be extrapolated to ^{128}Ce leading to the conclusion that it is more deformed than ^{130}Ce. Recent lifetime measurements for ^{128}Ce performed at Oak Ridge [Jo81] seem to support this conclusion. Another illustrative way to demonstrate the behavior of the yrast sequence is in an I_x versus $\hbar\omega$ plot as shown in Figure 6.14. In this figure, the g-bands of the $^{128-134}$Ce isotopes show a sequence where, at the same I_x, these bands have different rotational frequencies. This increase of rotational frequency indicates that at the same spin state (at low excitation energy), the more prolate-deformed ^{128}Ce will rotate slower (higher moment of inertia) than the more spherical ^{134}Ce. Hence there is an indirect relationship between the difference in rotational frequency for the same spin among the g-bands and the deformation pattern among the isotopes.
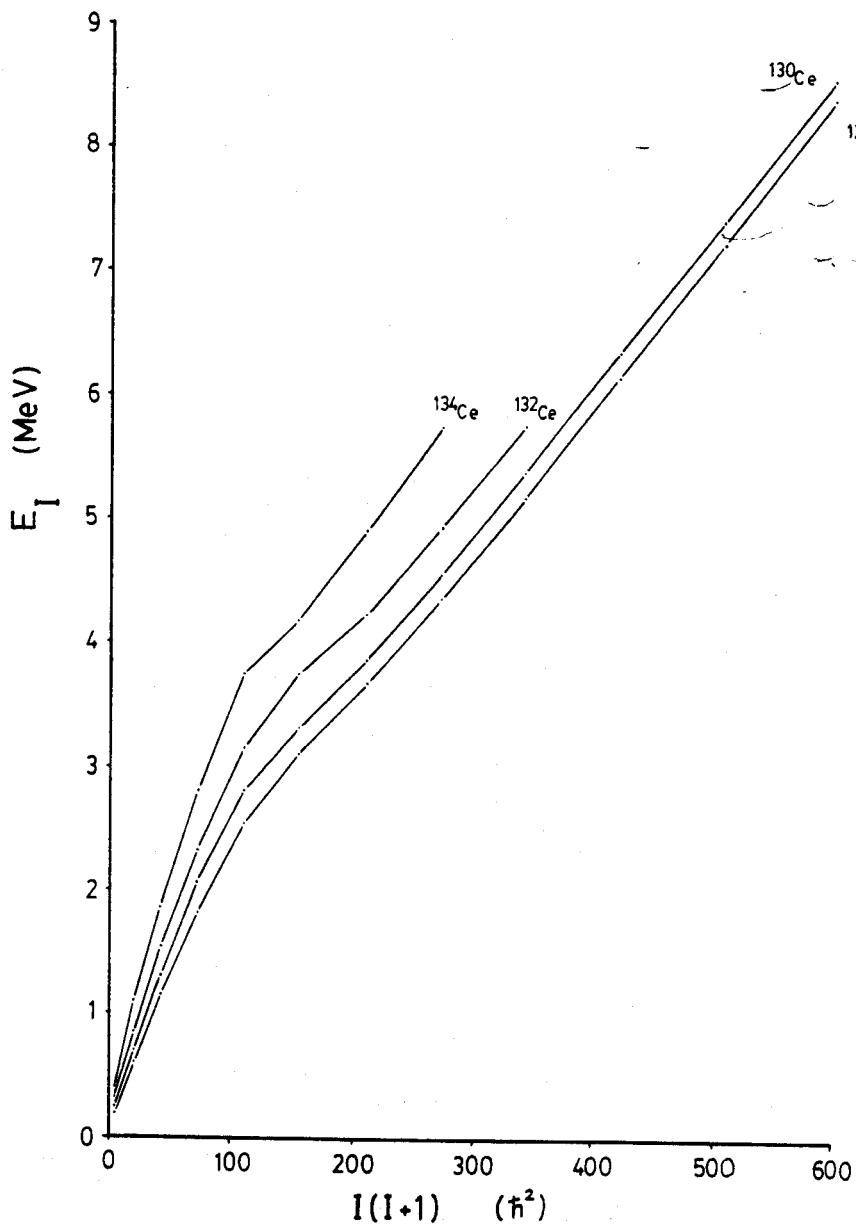
Figure 6.13 Plot of E_I versus $I(I+1)$ for the g.s.b. of $^{128-134}$Ce.
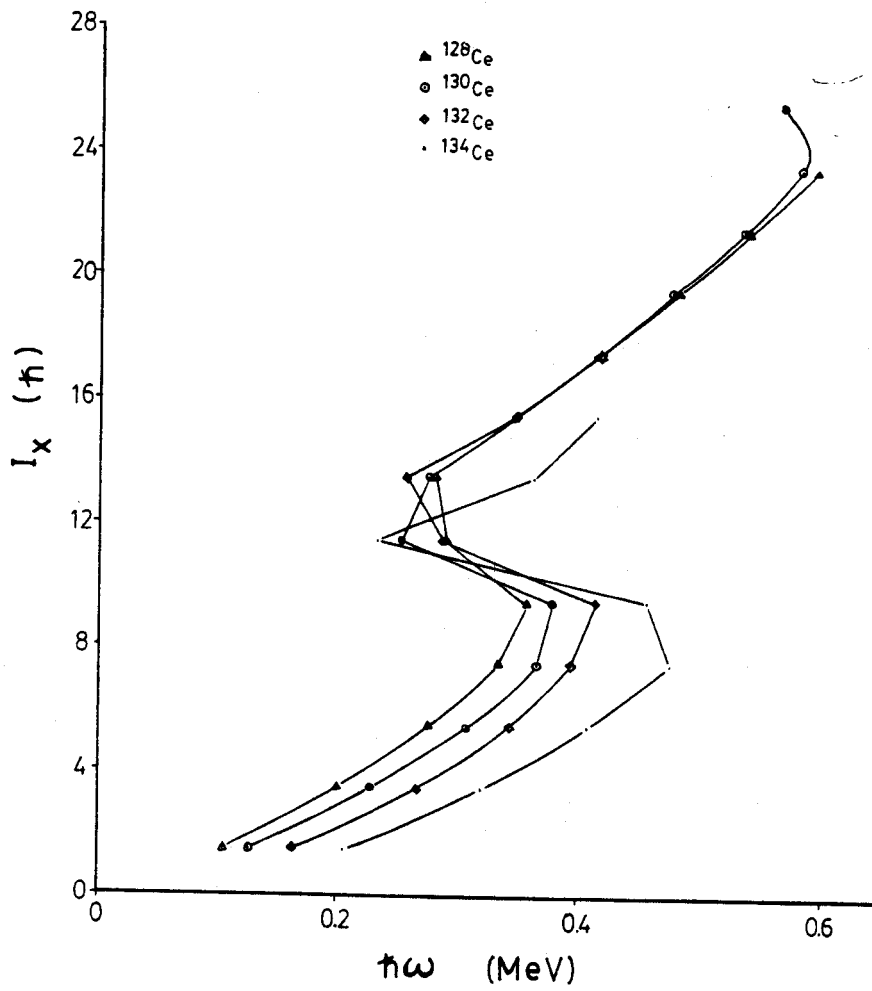
Figure 6.14 Plot of I_x versus $\hbar\omega$ for $^{128-134}$Ce.

The gain in alignment between the g- and s-bands can also be obtained semi-quantitatively from the I_x versus $\hbar\omega$ graph by the difference in I_x near the crossing frequency. For $^{128,130,132,134}Ce$, the ΔI_x values are (on the average) about 8.0, 9.0, 10.0 and 9.3 $\hbar$, respectively, at around $\hbar\omega$ = 0.3 MeV. The large alignment gain indicates that the s-band is a high-j quasiparticle band. This is schematically seen in Figure 6.15. The $h_{11/2}$ nucleons are coupled to zero angular momentum and the g.s.b. results from the collective motion of the nuclear core. With inreasing rotational frequency, the Coriolis forces will strongly decouple a high-j nucleon pair (in the case of an even-even nucleus) from time-reversed orbits, and align the pair along the rotational axis. The maximum alignment contribution from this decoupled $h_{11/2}$ nucleon pair is 11/2 + 9/2 = 10 $\hbar$. From the Nilsson level diagram for protons (Figure 6.16) in ^{128}Ce at ε_2 = 0.26 and ε_4 = 0.00 deformation, it is seen that the lowest unoccupied $h_{11/2}$ orbital is near the Fermi surface, and easily accessible through low excitation energy. Hence, a large alignment gain can be obtained by decoupling the proton pair in the time-reversed $h_{11/2}$ orbits.

One interesting feature of the I_x versus $\hbar\omega$ plot (Figure 6.14) is the fact that the s-bands for $^{128,130,132}Ce$ are amazingly similar in I_x values up to $\hbar\omega \sim$ 0.5 MeV where the second backbend for ^{130}Ce commences. Could this similarity indirectly imply that the deformation for the s-bands is the same for all these three Ce isotopes? This question can not be easily answered without a detailed calculation about the nuclear shape at such excitation energy which is beyond
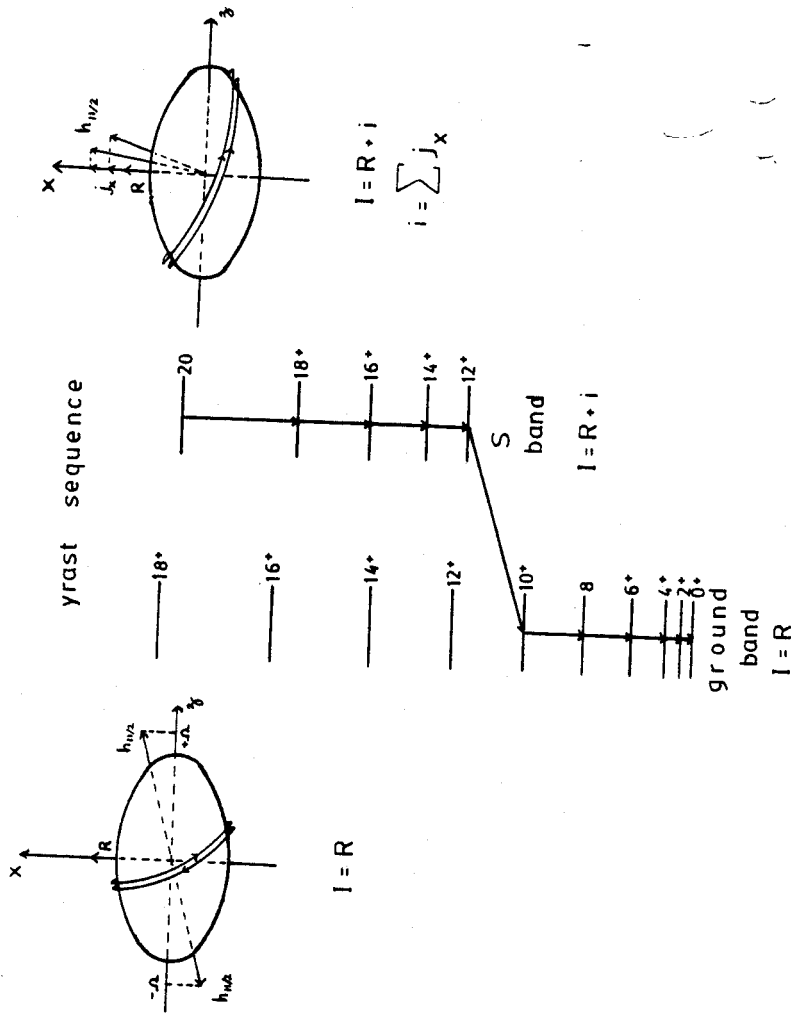
Figure 6.15 Schematic drawing for coupling and decoupling of a pair of $h_{11/2}$ nucleons in time-reversed orbits.
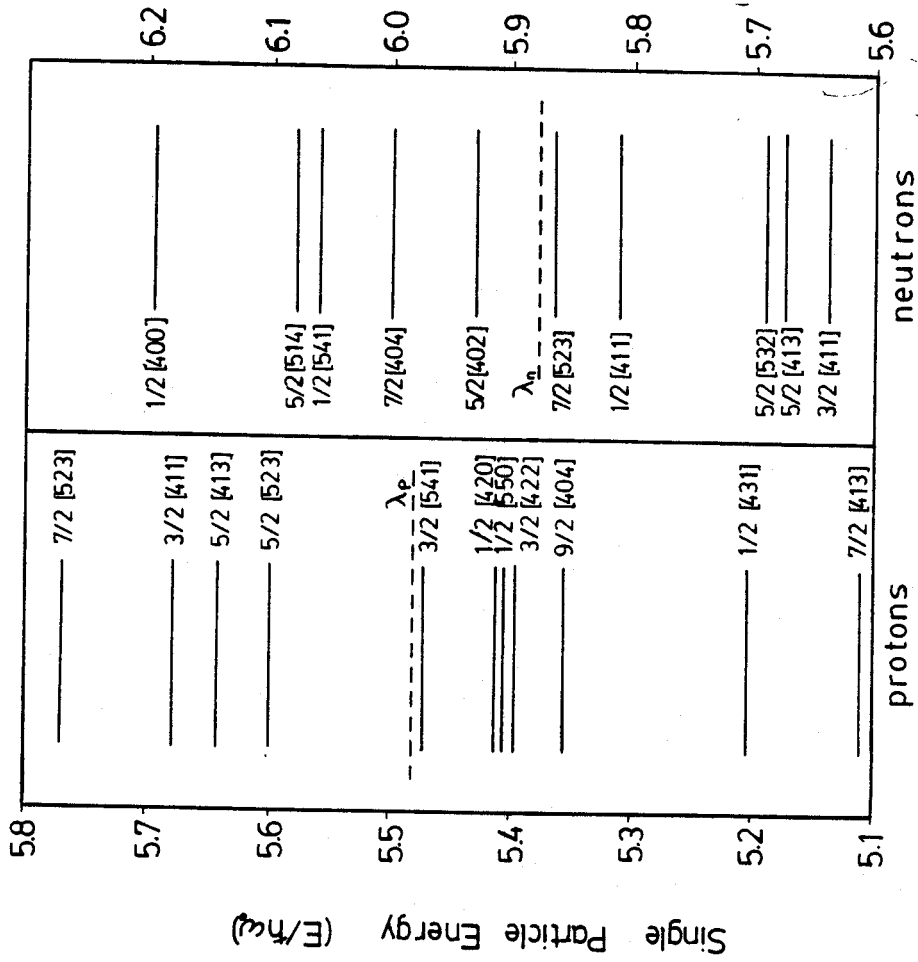
138

Figure 6.16 Nilsson level diagram for ^{128}Ce using ε_2=0.260 and ε_4=0.00 deformation.

the scope of this work. This suggests the possibility that the s-bands for these three Ce isotopes have similar band structure because of the resemblance displayed in the I_x versus $\hbar\omega$ plot. The adding of neutrons did not seem to significantly alter the structure of the s-bands, indirectly indicating that these bands may possibly have a proton configuration. The s-band structure is well understood in the CSM, and further discussion is left to a later section.

6.2 The Sideband 1

The analysis of the sidebands was quite difficult due to the complexity of the total coincidence spectrum in the energy region of interest for intraband transitions (between 300-800 keV). Several factors contributed to this spectrum complexity, namely: 1) contamination due to other reaction channels; 2) similarity in the energy of band transitions among neighboring final reaction products; and 3) restriction on the size of the two-dimensional matrix (2K by 2K) that could be built in disk storage (resolution was reduced).

By using the analytical techniques described in the previous section, it was possible to build sequences of coincident transitions. The quality of each gated spectrum depended on: 1)if the transition of interest was part of a multiplet; and 2) how far up a specific gated transition is in the band sequence. Even though some 240 million coincident-pair events were recorded, the statistics in the gated spectra for the sidefeeding transitions were not very high. Error bars could, sometimes, be as large as the peak areas of interest

in such a gated spectrum.

One of the sequences built is seen in Figure 6.1 as the band at which the lowest observed level is 1890 keV. The angular distribution results indicate that the intraband transitions are of stretched E2 character, suggesting a $\Delta I = 2$ sequence for the band. For the 425-keV sidefeeding transition, which corresponds to the (2246 keV) $\rightarrow 8_g^+$ decay, the angular distribution coefficients are consistent with the following transition possibilities: a) (M1,E2) mixed; b) pure or stretched E1; and c) pure or stretched M1. Because the 425-keV transition decays to the 8_g^+ state, possibility a) indicates that the parent level would be 7^+, 8^+, or 9^+ while (b) is consistent with 7^- or 9^-. The third possibility for the 2246-keV level suggests 7^+ or 9^+ spin assignment. Since the parity of the sideband cannot be determined from an angular distribution experiment, the above results can be combined to a tentative overall spin assignment of (7,8,9).

A similar sideband was observed in ^{130}Ce [NoP] (with a sequence of intraband transitions of 358-, 448-, 559-, 707-, 836-, and 896-keV). Its sidefeeding pattern can also be used on a general guide in spin assignment for the sideband 1 in ^{128}Ce. The lowest observed level of the similar sideband in ^{130}Ce decays to the 6_g^+ level, while the next level up (which corresponds to the 2246-keV level in ^{128}Ce) decays both to 8_g^+ and to 6_g^+, placing an upper limit of spin 8 to the parent level (assuming that $\Delta l > 3$ multipolarities are not observed for transitions in a low-lying sideband in this mass region). Then, by comparison, the 2246-keV level can be assumed to also have an upper

limit of spin 8, reducing the tentative assignment from (7,8,9) to (7,8). Then, the lowest observed level of the sideband 1 in ^{128}Ce is tentatively assigned spins (5,6).

Using these spin assignments, a plot of E_I versus $I(I+1)$ is drawn in Figure 6.17, and it can be seen that the sideband behaves like a rotational band with either assignment. A discussion of the band structure will follow in the Cranking Shell Model (Chapter VI, Section 4) discussions.

6.3 The Sideband 2

For the second sequence of coincident transitions, four levels were established (possibly five) and only one sidefeeding transition was determined (Figure 6.1). The lowest level observed in this sideband has been placed at 1988.8 keV. The level at 2418.7 keV feeds into the 8_g^+ member of the ground band via a 598.2-keV transition which is coincident with a close-lying γ ray at 597.2 keV. The latter transition is a member of this sideband since it is observed in all gated spectra corresponding to the intra-band transitions. Reasonably good angular distribution results could not be obtained for this sidefeeding transition because of the irregular behavior at different angles; therefore, no tentative spin assignment was given. This irregular behavior can be understood if it is assumed that the intraband transitions are E2 and that the observed sidefeeding transition can be (M1,E2), pure E1 or pure M1, as argued for sideband 1. Then, the intensity of such a doublet will oscillate, depending on the intensity of the individual γ rays at different angles.
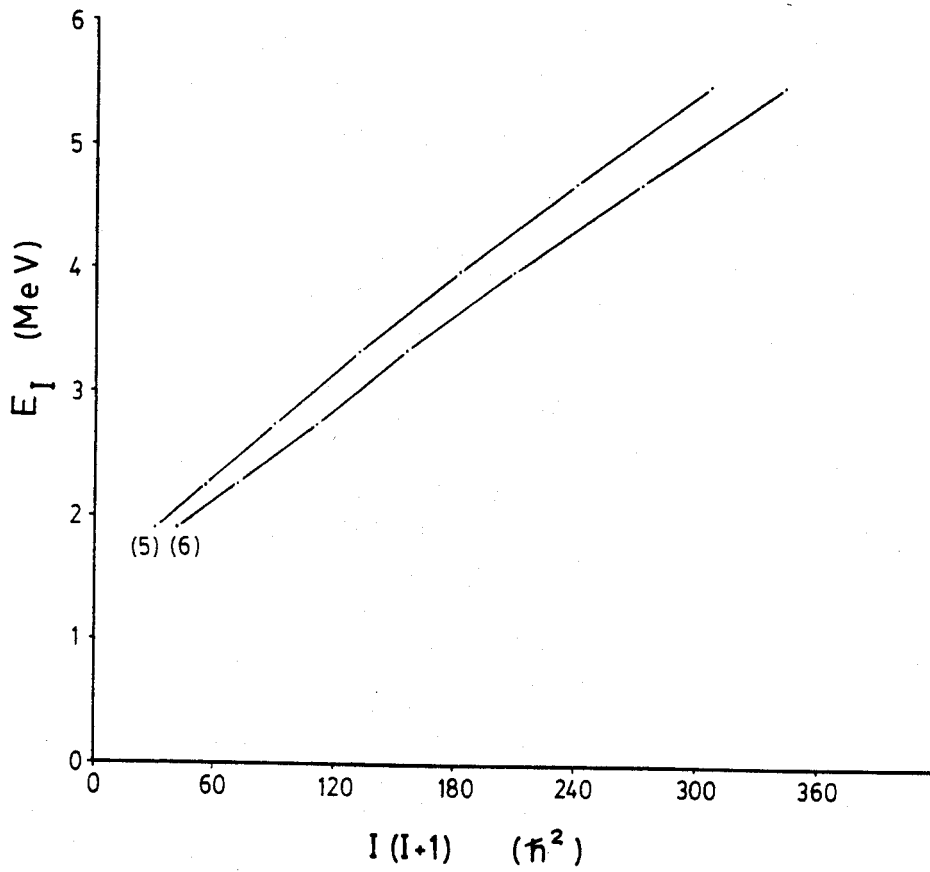
Figure 6.17 Plot of E_I versus $I(I+1)$ for sideband 1 in ^{128}Ce.

A similar sideband has also been observed in ^{130}Ce [NoP] with a sequence of transitions 427-, 610-, 767-, 895-, and 977-keV as compared to the 430-, 598-, 751-keV and possibly 858-keV transitions in ^{128}Ce. An interesting point in the ^{130}Ce data is that transitions between the sidebands were observed while in ^{128}Ce, no such transitions were evident. The latter fact may simply be due to the low statistics in the gated spectra. These interband transitions in ^{130}Ce could indicate that these two sidebands are decoupled bands due to Coriolis forces. Therefore, high-j quasiparticles would be necessary in order to form the band structure, and, consequently, large alignment gain is obtained with increasing rotational frequency.

6.4 The Cranking Shell Model and the Observed Bands in ^{128}Ce

One of the main advantages of the Cranking Shell Model is the simplification into compact diagrams of some of the characteristics of the nuclear behavior. The usual Routhian e' versus ℏω diagram indicates, for example, which quasiparticles are involved in a certain band structure (and, consequently, the band parity), how much alignment gain and relative energy are involved in a quasiparticle excitation, the rotational frequency where two bands cross each other as well as and the interaction strength between the crossing bands. Therefore, such diagrams can be used to study the gradual changes in the valence-nucleon pairing.

The rotating frame calculations can give an insight of the behavior of the observed bands in ^{128}Ce. The reference band is taken to be the s-band since it changes gradually with increasing rotational

frequency, and it is not affected as much by a backbending as the g-band. The $\mathfrak{J}_0$ and $\mathfrak{J}_1$ obtained are 16.5 $\hbar MeV^{-1}$ and 24 $\hbar^3 MeV^{-3}$, respectively. These parameters represent a compromise among different values that yield constant alignment for both the g- and s-bands.

The experimental Routhians (e') can be obtained by using the extracted $\mathfrak{J}_0$ and $\mathfrak{J}_1$ values. In Figure 6.18, a plot of the experimental Routhian e' versus $\hbar\omega$ is shown. For the yrast band, the crossing frequency for the g- and s-bands is $\hbar\omega_c \sim 0.315$ MeV, and the alignment gain is about 8.9 $\hbar$ (i = -de'/dω). The alignment gain is also conveniently observed in an i versus $\hbar\omega$ (Figure 6.19). This large alignment indicates the high-j quasiparticles are needed for the s-band structure. In the Nilsson level diagram for ^{128}Ce (Figure 6.16) it is seen that, for both protons and neutrons, $h_{11/2}$ orbitals are nearest to the Fermi surface and are logical choices for the s-band structure (high-j orbitals). One way to determine if the s-band is either quasiproton or quasineutron is by the observed blocking of the odd-proton in the neighboring $^{127}_{57}La$ [Wa75]. The flat behavior of the (11/2⁻) one-quasiproton band around the crossing frequency in the i versus $\hbar\omega$ plot (Figure 6.19) indicates that such proton (and its orbital) is involved in the s-band structure of ^{128}Ce. Simplistically, the odd-proton blocks the excitation of a core-proton into its quasiparticle orbital (Pauli principle); therefore, a crossing quasiparticle band is not formed and no backbending is observed in ^{127}La at around $\hbar\omega_c \sim 0.315$ MeV. In ^{128}Ce, the quasiproton pair is excited into $h_{11/2}$ quasiparticle orbitals, and

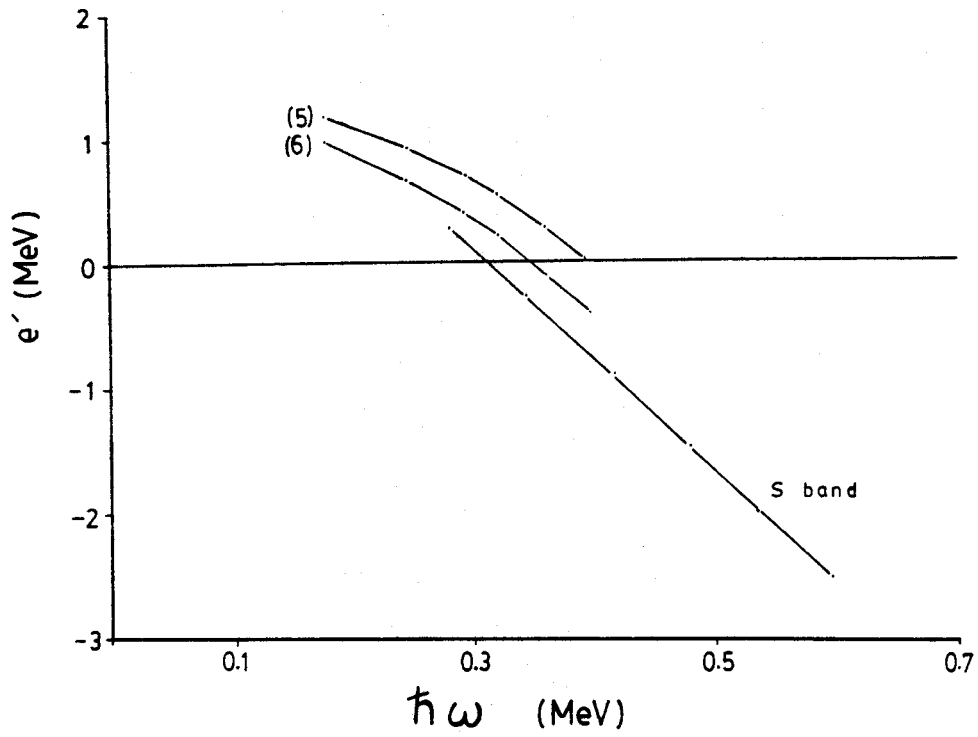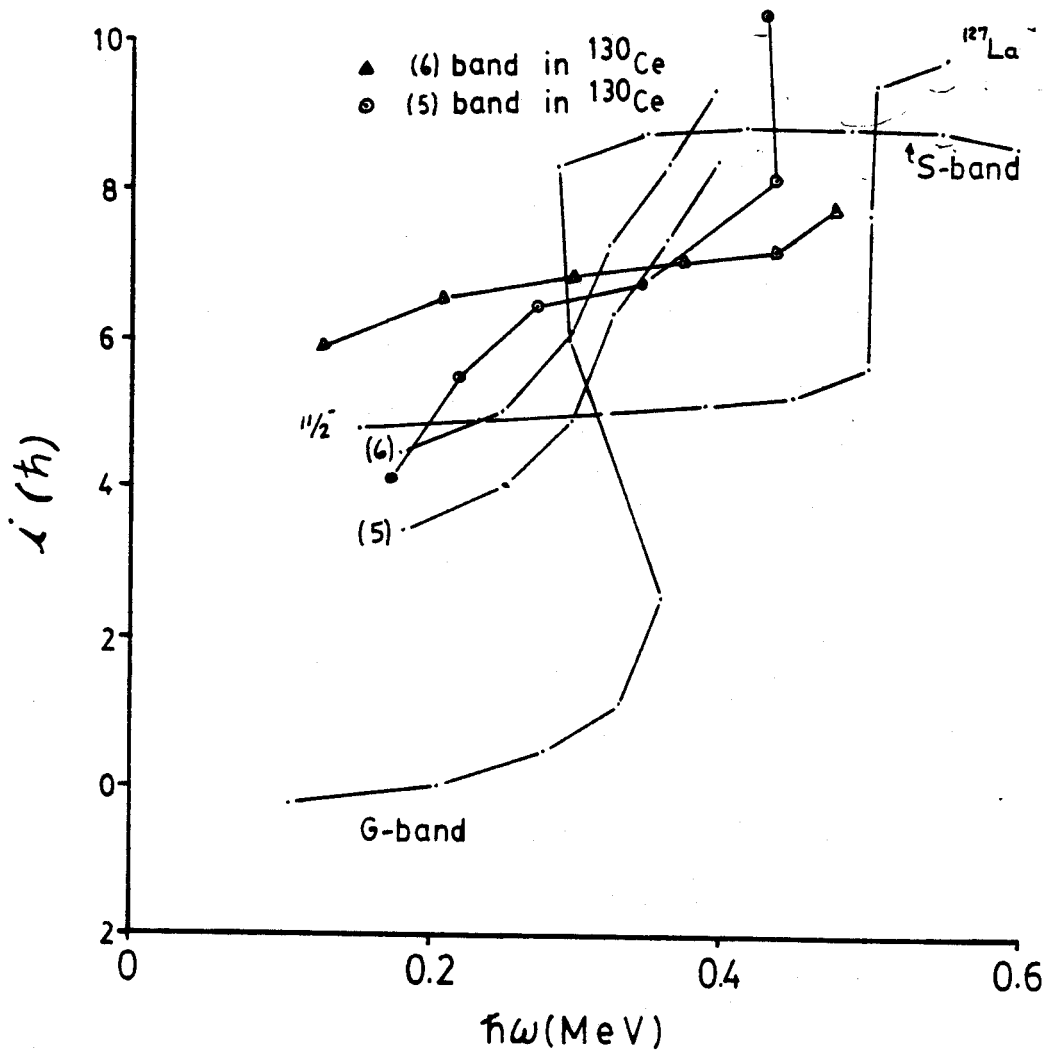Figure 6.18 Experimental Routhian e' versus ℏω for ^{128}Ce.

Figure 6.19 Experimental i versus ℏω for ^{128}Ce.
Also, ^{130}Ce sidebands are plotted.

backbending occurs with the crossing of the g- and s-bands. Then, both quasiprotons contribute to the s-band structure.

The theoretical Routhian diagram (e' versus $\hbar\omega$) for protons in ^{128}Ce is obtained from the Cranking Shell Model calculations, and is presented in Figure 6.20. The crossing frequency between the g- and s-bands is calculated to be around $\hbar\omega_c$ = 0.317 MeV(obtained as the rotational frequency of closest approach between curves A and -A as well as B and -B), and the alignment gain is about 5.0 + 3.4 = 8.4 $\hbar$ (obtained by adding the maximum slope of the curves A and B) which agrees well with the experimental data in the rotational frame ($\hbar\omega_c$ = 0.315 MeV and 8.9 $\hbar$ for the alignment gain). Additionally, the theoretical Routhian diagram for neutrons in ^{128}Ce (Figure 6.21) yields $\hbar\omega_c \sim$ 0.66 MeV for the first backbending, implying, therefore, that the s-band is indeed a $h_{11/2}$ two-quasiproton band.

The sideband 1 is more difficult to understand in terms of the Cranking Shell Model. In the i versus $\hbar\omega$ plot (Figure 6.19), the side-band is shown to continuously gain alignment with rotation of the core, meaning that there is no blocking of $h_{11/2}$ quasiprotons and, therefore, this sideband could have quasineutrons in its structure (see explanation of blocking particles in this section). There is also a small kink around $\hbar\omega \sim$ 0.32 MeV that could be somehow related to the first backbend ($\hbar\omega_c \sim$ 0.315 MeV).

There are two possible explanations for the observed behavior of sideband 1. One is that sideband 1 starts as a ($h_{11/2}d_{5/2}$) two-quasiproton band at low rotational frequency and crosses with a
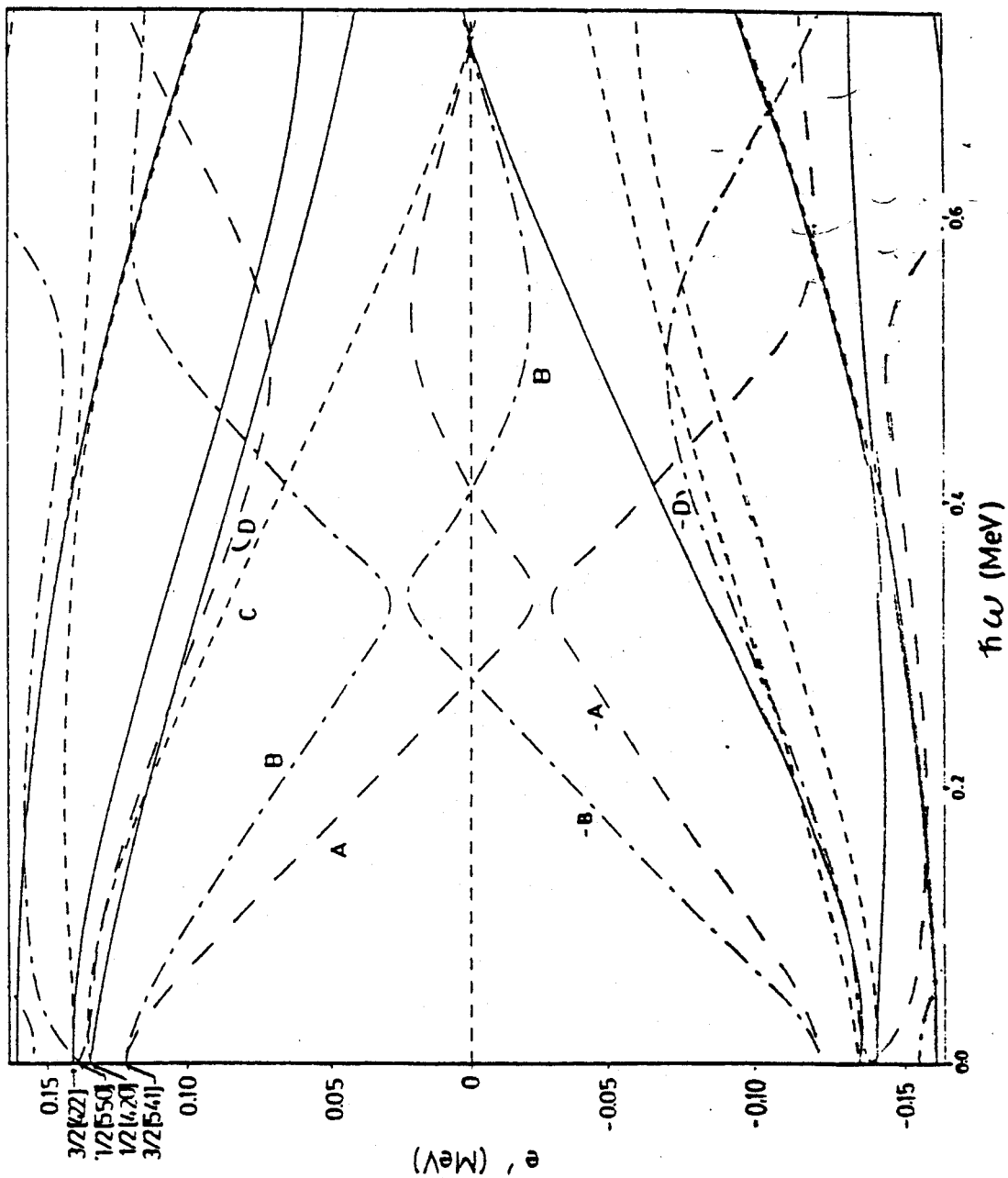
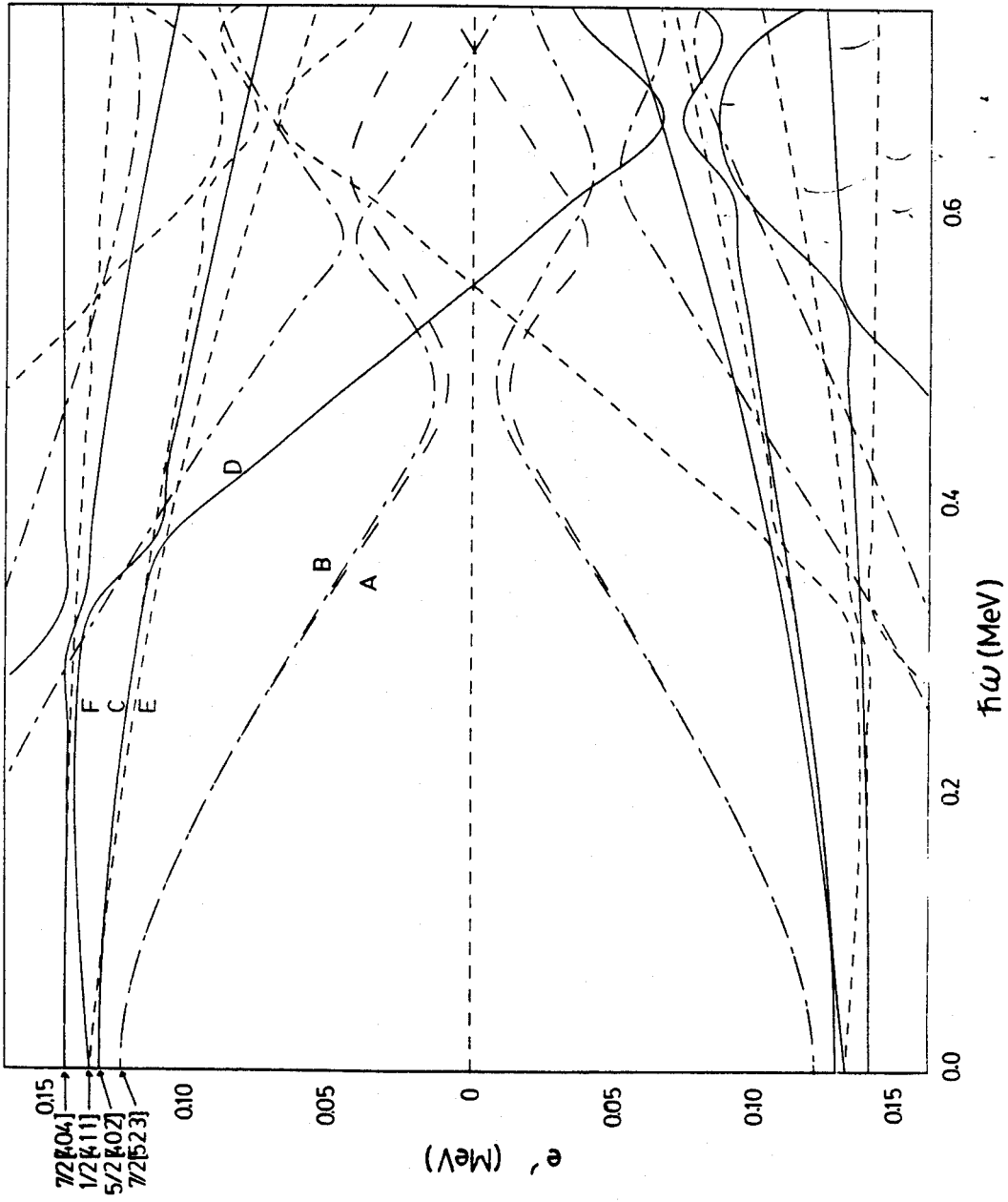Figure 6.20   Theoretical Routhian e' versus $\hbar\omega$ diagram for protons in ^{128}Ce.

Figure 6.21 Theoretical Routhian e' versus ℏω diagram for neutrons in ^{128}Ce.

$(h_{11/2}^3 d_{5/2})$ four-quasiproton band (at a rotational frequency higher than the backbending frequency seen in the yrast sequence) with a possible maximum alignment of 11 $\hbar$ (adding the maximum slopes of curves A,B,C,and D). This is schematically seen in Figure 6.22(a) in an ideal i versus $\hbar\omega$ plot. The flat behavior of the sideband around ω_c shows the blocking of a $h_{11/2}$ quasiproton, indicating the presence of this quasiproton in the sideband structure. This behavior is similar to ^{127}La where the one-quasiproton g.s.b. crosses with a three-quasiproton band [NoP] at $\hbar\omega \sim 0.50$ MeV (Figure 6.19) and has a Δi of about 5 $\hbar$. One of the problems for this possibility is that sideband 1 starts at low rotational frequency with an alignment (for either spin assignment) that is smaller than what is observed for the $h_{11/2}$ one-quasiproton band in ^{127}La, suggesting that sideband 1 may not start (at low $\hbar\omega$) as a twoquasiproton band.

A more plausible explanation is that the sideband starts (at low $\hbar\omega$) as a $(h_{11/2}d_{5/2})$ two-quasineutron band and crosses with a $(h_{11/2}d_{5/2})_n(h_{11/2})_p^2$ two-quasiproton-two-quasiproton band (Figure 6.22(b)). Therefore, this is a 2n → 2n2p excitation. Two "fingerprints" of the crossing can be seen in the i versus $\hbar\omega$ plot (Figure 6.19): 1) the crossing frequency - the two-quasineutron excitation is not blocked by the two-quasiprotons in the s-band, therefore, sideband 1 should strongly backbend around $\hbar\omega \sim 0.32$ MeV (actually, it only "upbends" slightly); 2) large alignment gain due to the presence of $h_{11/2}$ quasiprotons in the four-quasiparticle excitation - higher spins were not seen for the sidebands, but from
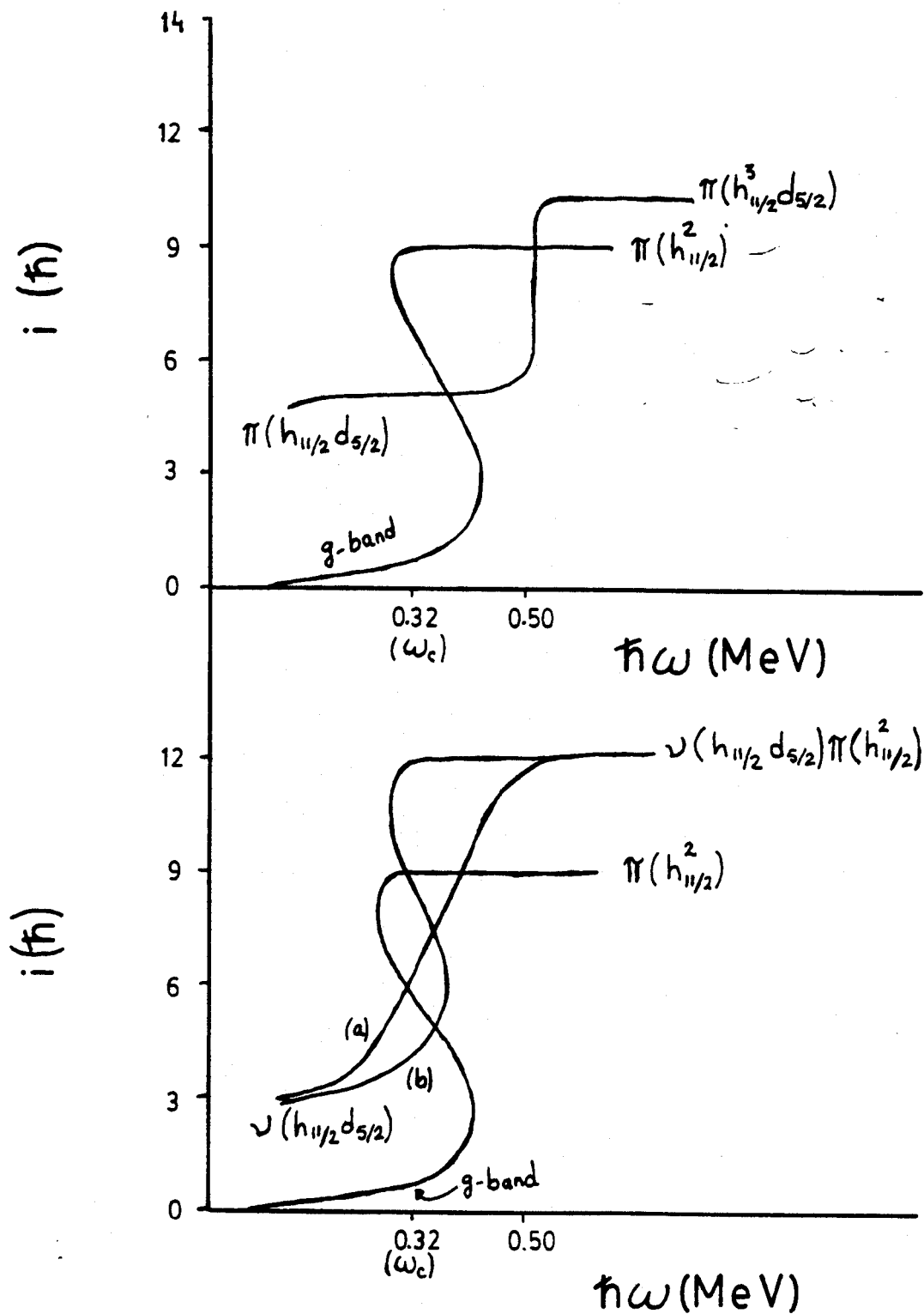
Figure 6.22   Schematic diagram for two possible
               excitations for sideband 1 in ^{128}Ce.

Figure 6.19 it is seen that the sideband is still gaining alignment up to measured spins with yet no indication of reaching maximum alignment. The "upbend" and "backbend" behavior is a reflection of the interaction strength between the crossing bands, where the former indicates large interaction, as discussed in Chapter II. This difference in interaction ("upbend" for the sideband versus "backbend" for the yrast band) could possibly indicate a deformation change for the excitation related to the sideband.

In summary, the experimental resuls for the crossing frequency of the first backbend ($\hbar\omega_c \sim 0.315$ MeV) as well as the s-band structure ($h_{11/2}$ two-quasiproton band) are reproduced very well by the Cranking Shell Model calculations. For sideband 1, it is more difficult to obtain an accurate picture of its behavior with this model. One possible reason for the observed behavior is that the band starts as a two-quasineutron band and crosses with a two-quasineutron-two-quasiproton band at $\hbar\omega_c \sim 0.32$ MeV. The model can account for the alignment gain and crossing frequency, but the interaction strength is not so well predicted. For sideband 2, additional information about the spins of the levels is necessary in order to use the Cranking Shell Model.

CHAPTER VII

CONCLUDING REMARKS

The nuclei studied in this work, ^{128}Ce and ^{168}Yb, represent two different regions of deformation. The former is in a prolate-spherical transitional region, while the latter is in a well-deformed (rare-earth) region. Therefore, their single-particle and collective spectra should differ somewhat because of the different valence orbitals involved in the spectra. In this study it was possible to extend to higher spin states the known sidebands in ^{168}Yb as well as to determine the band members of the previously known 5⁻ isomer. For ^{128}Ce, the yrast band was extended well beyond the first backbend and two sidebands were also determined.

A useful nuclear model should account for the observed spectra, such as those obtained for ^{168}Yb or ^{128}Ce. One such model that has been successfully applied in the well-deformed rare-earth region, especially for the light Yb isotopes like ^{160}Yb, is the Cranking Shell Model. The main ideas in the CSM are that the excited states in the rotational spectra result from the arrangement of a few quasiparticle orbitals, and that these excited states are composed of quasiparticle(s) relative to a reference state. The nuclei studied in this work were good examples to test the wide applicability of the model because of the different deformed regions involved and the

153

backbending/non-backbending behavior of the two isotopes. This work represents one of the first attempts to apply the model in the mass region around A ~ 128.

For ^{168}Yb, CSM was reasonably successful in predicting band structure, alignment gain, and excitation energy of the observed rotational bands. Also, the non-backbending behavior was accurately described. For ^{128}Ce, the backbending behavior was predicted reasonably well, and the band structure and alignment gain of the s-band were accurately described. One of the sidebands could be only partially described, probably due to band structure changes at higher rotational frequency. It is clear that more theoretical work is needed in relation to proton-neutron mixture and high-K bands in order to explain finer spectroscopic details of the rotational spectra.

APPENDIX

APPENDIX A

Some Important Gated Coincidence Spectra of Transitions in ^{168}Yb

This section shows some of the important background subtracted gated spectra that were obtained from a coincident experiment with two planar Ge and large volume Ge(Li) detectors.

The peaks with a * could not be identified and those with a † are contaminant γ rays originating from ^{169}Yb, ^{19}F, ^{27}Al, or the oxide matrix. Since these spectra are compressed, statistical fluctuations in the background may add up to give a peak but these are easily identified in the normal 4K spectra.

The spectra numbered A1 through A12 are the "Sidefeeding transitions between the γ- and the ground state bands". The spectra numbered A13 through A19 are "Intraband transitions for the K=3$^+$ and K=5$^-$ bands".
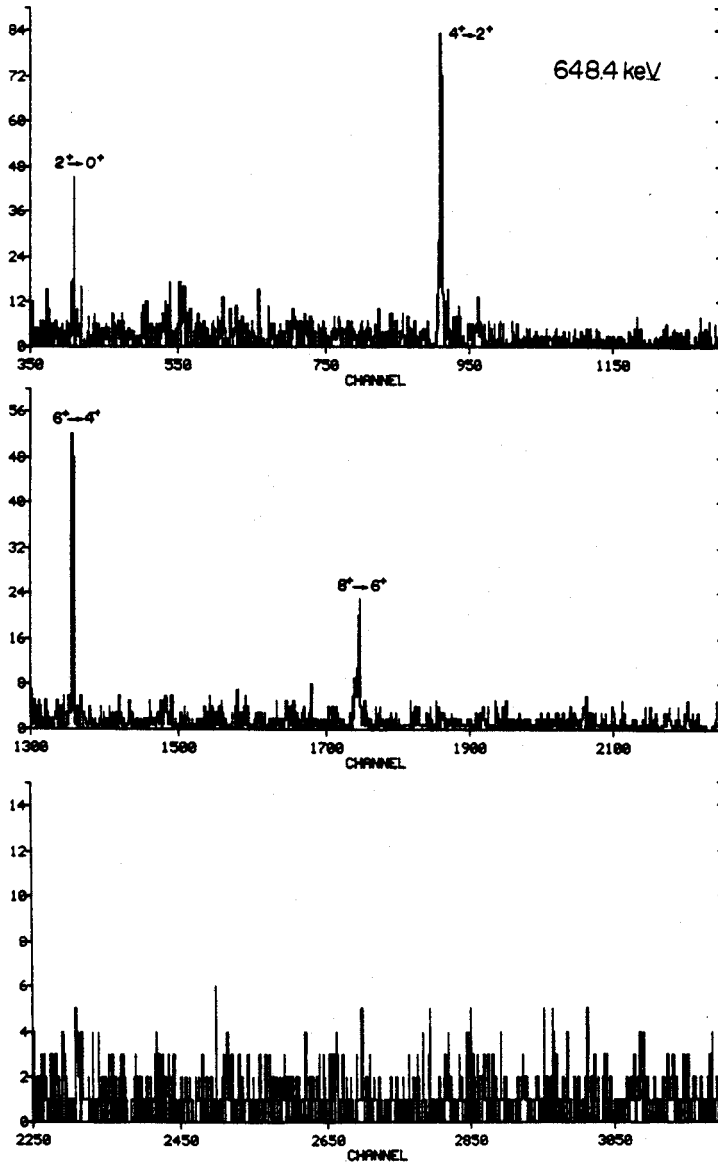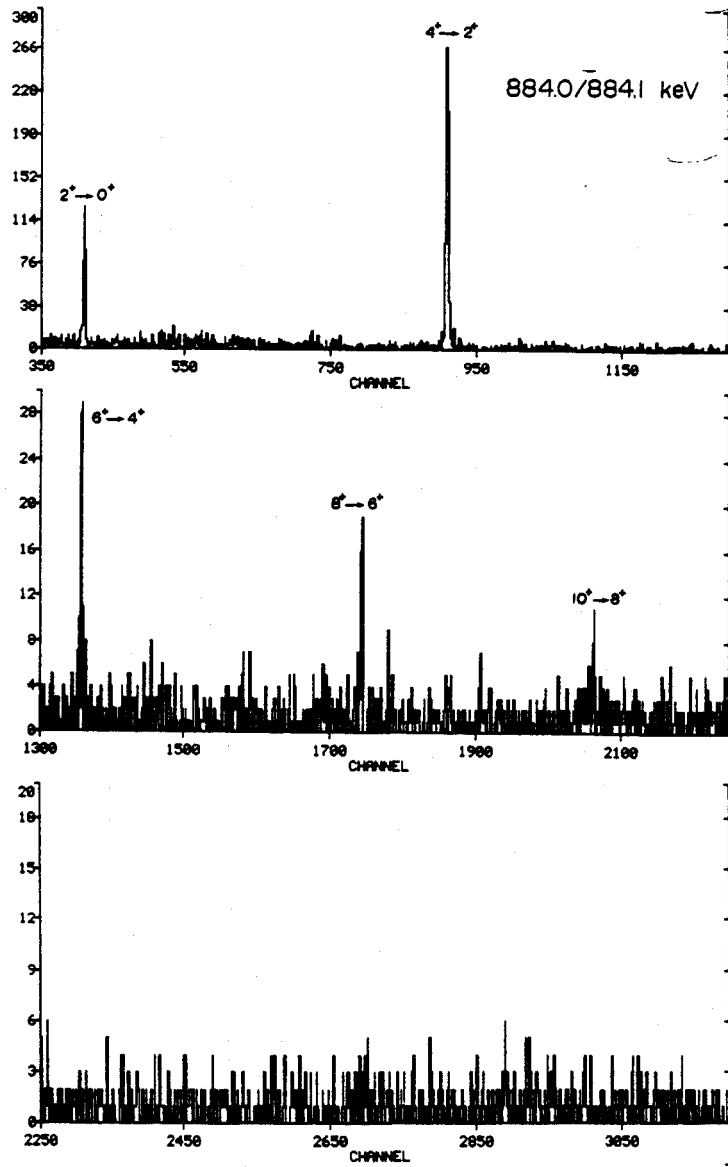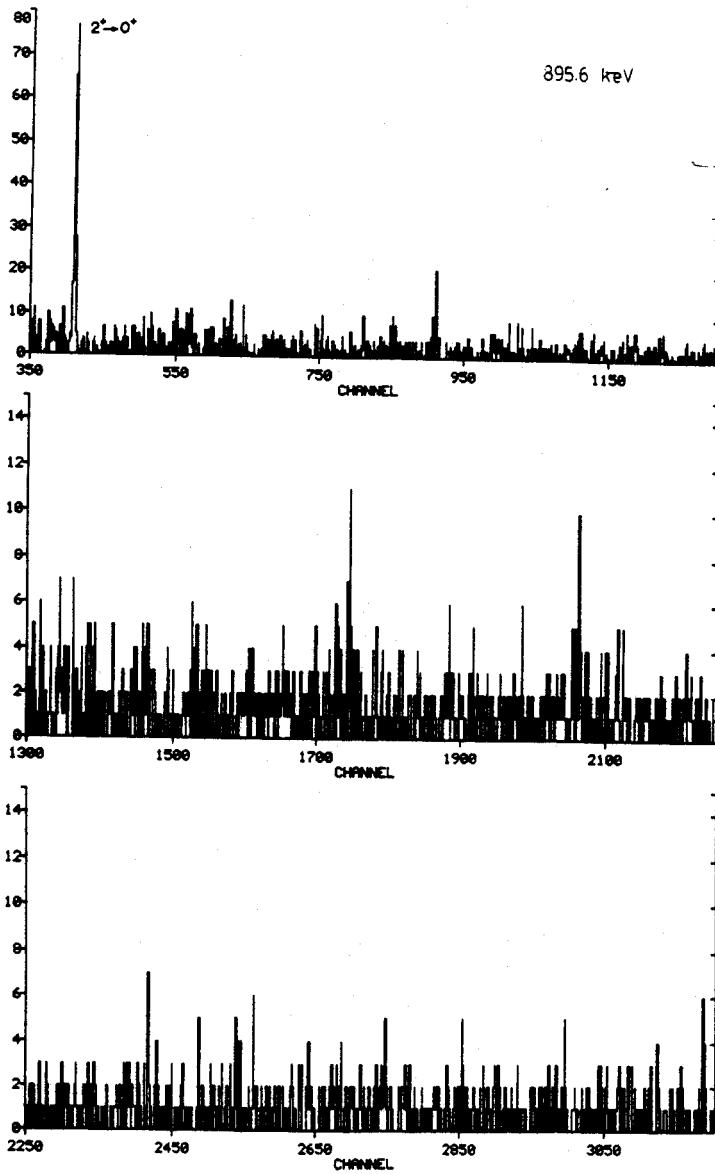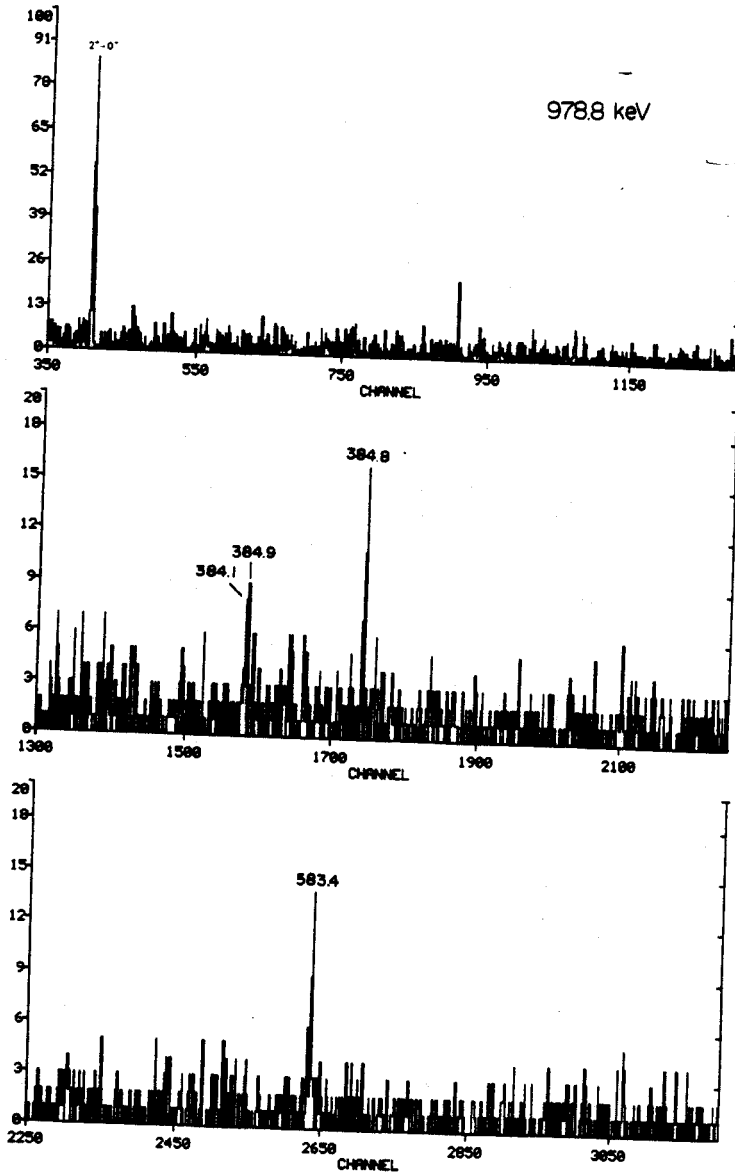
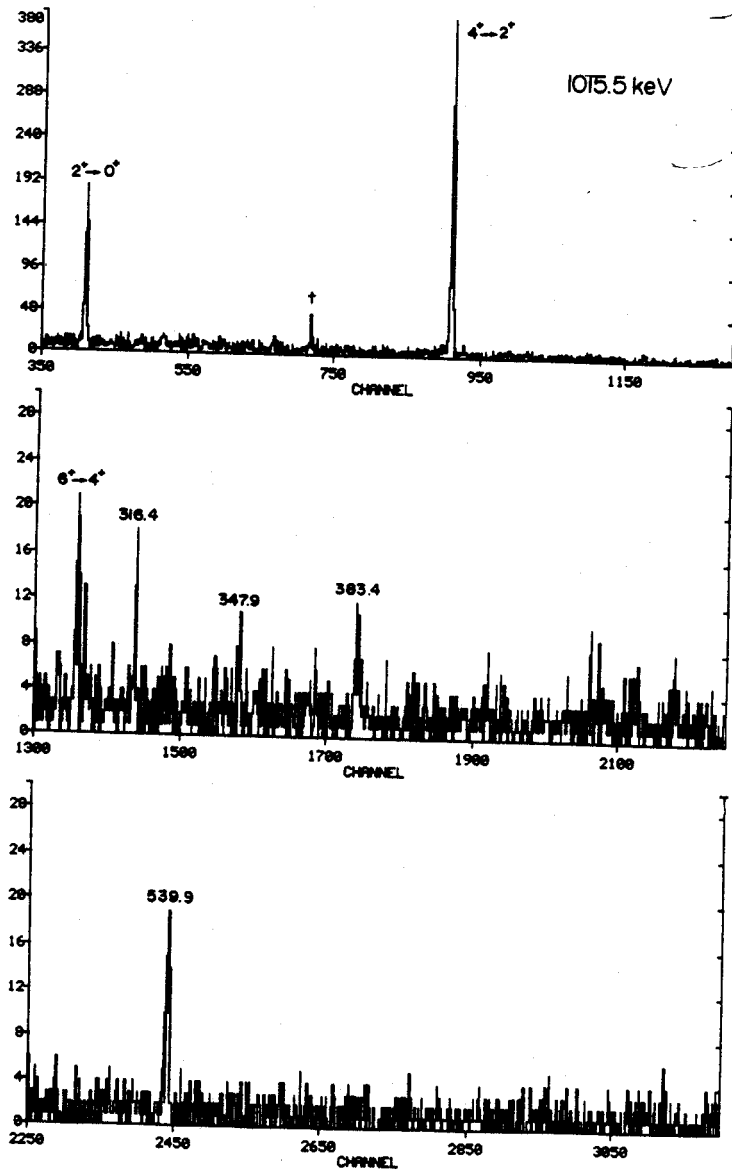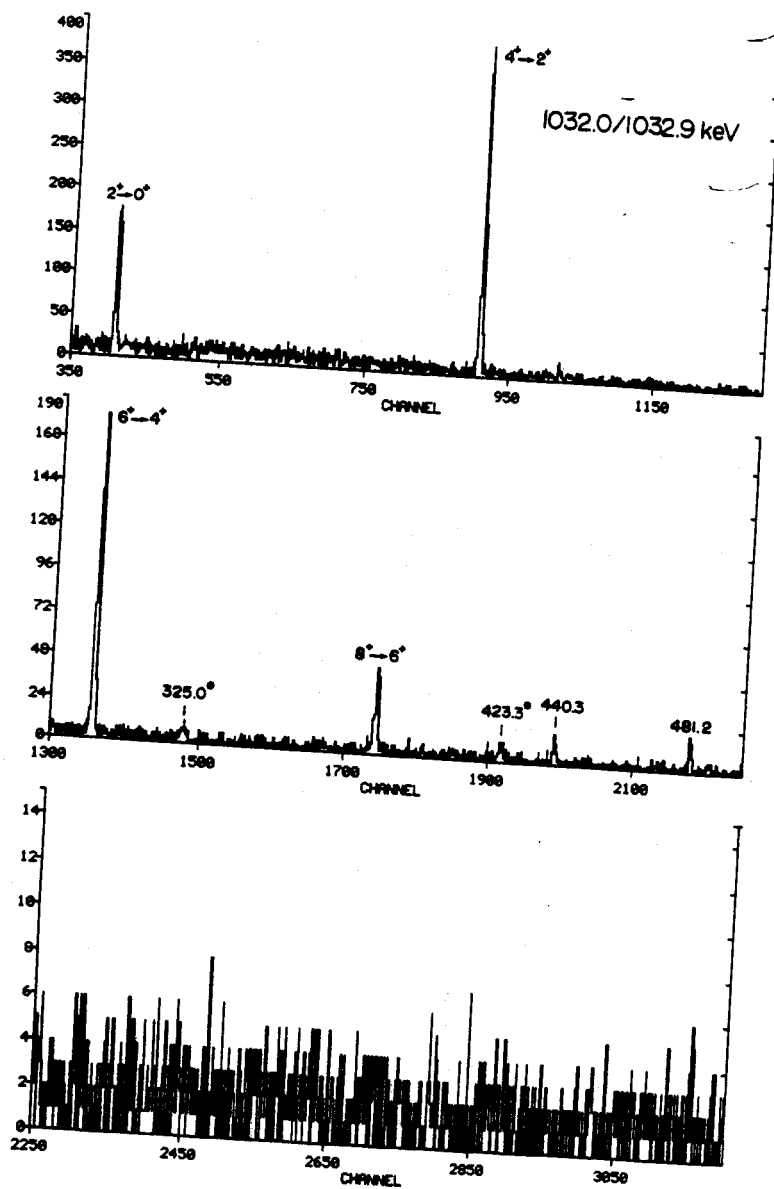Figure A1
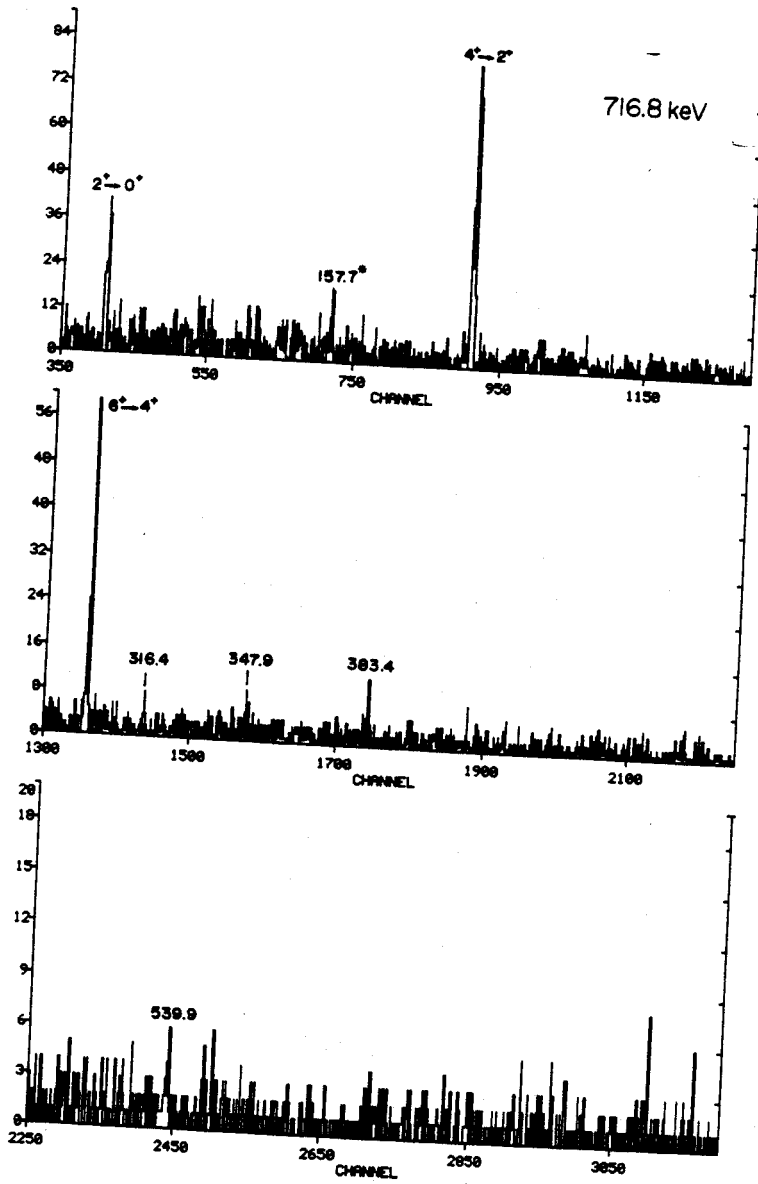
Figure A2
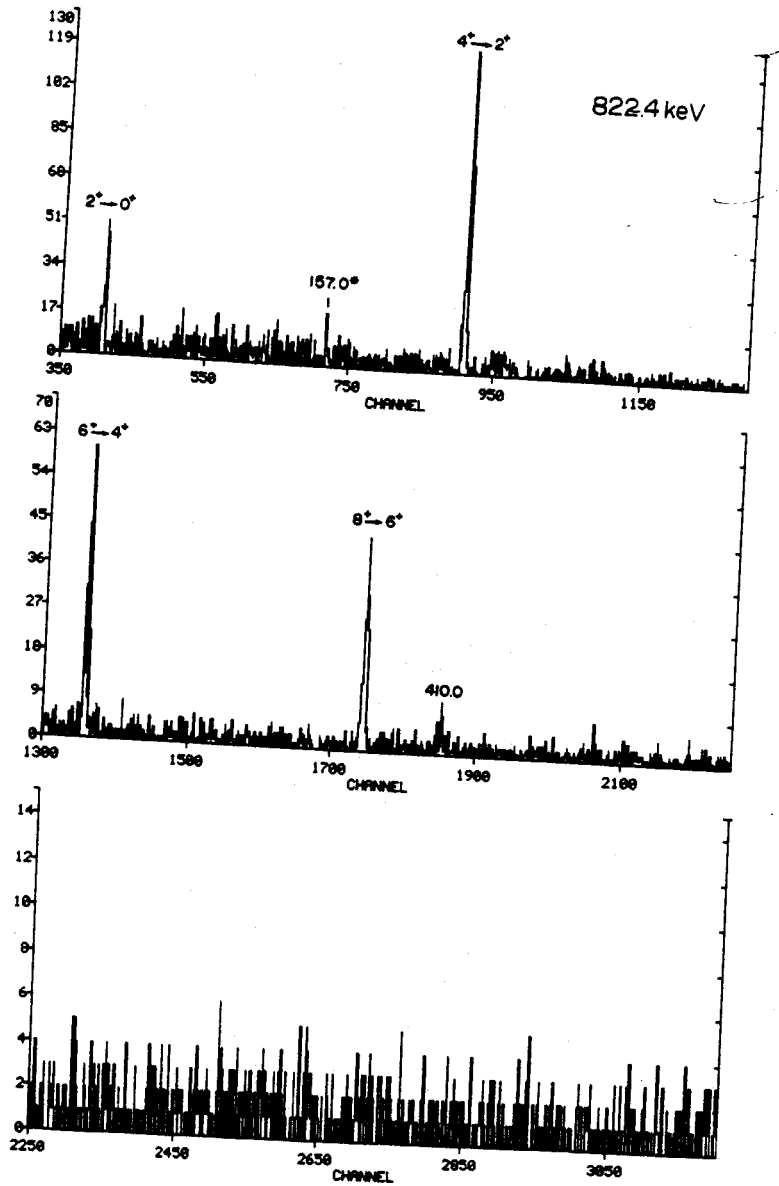
Figure A3
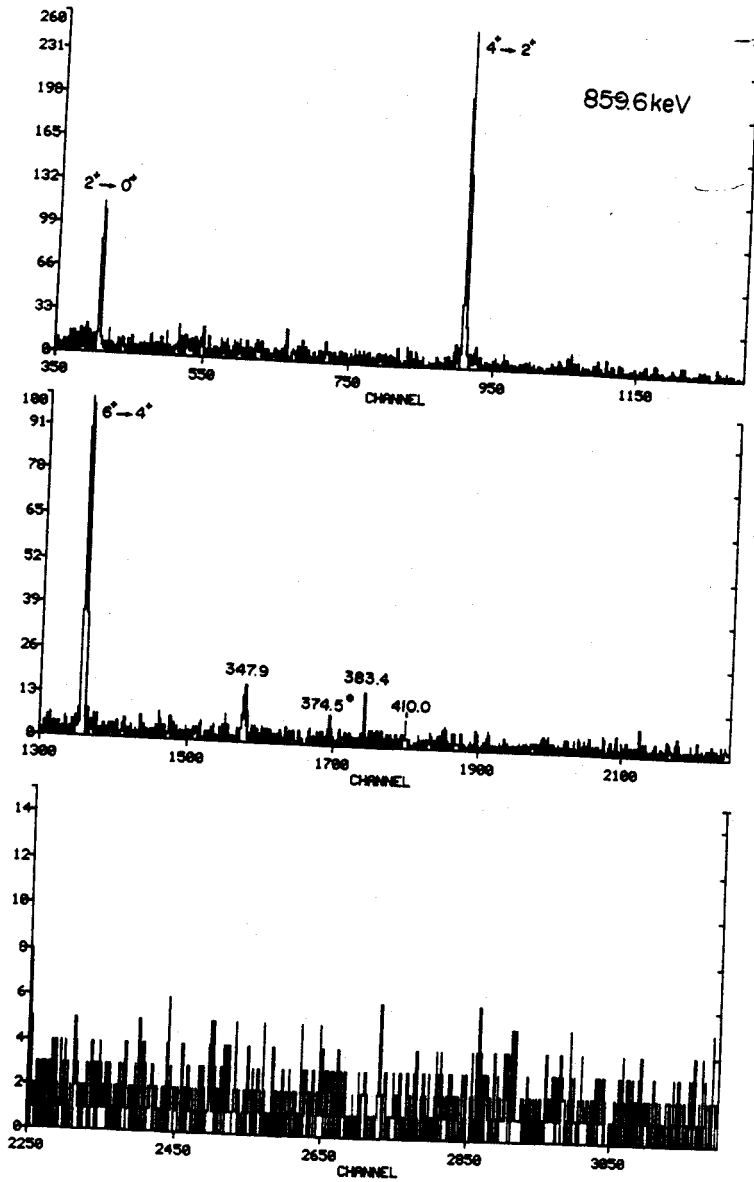
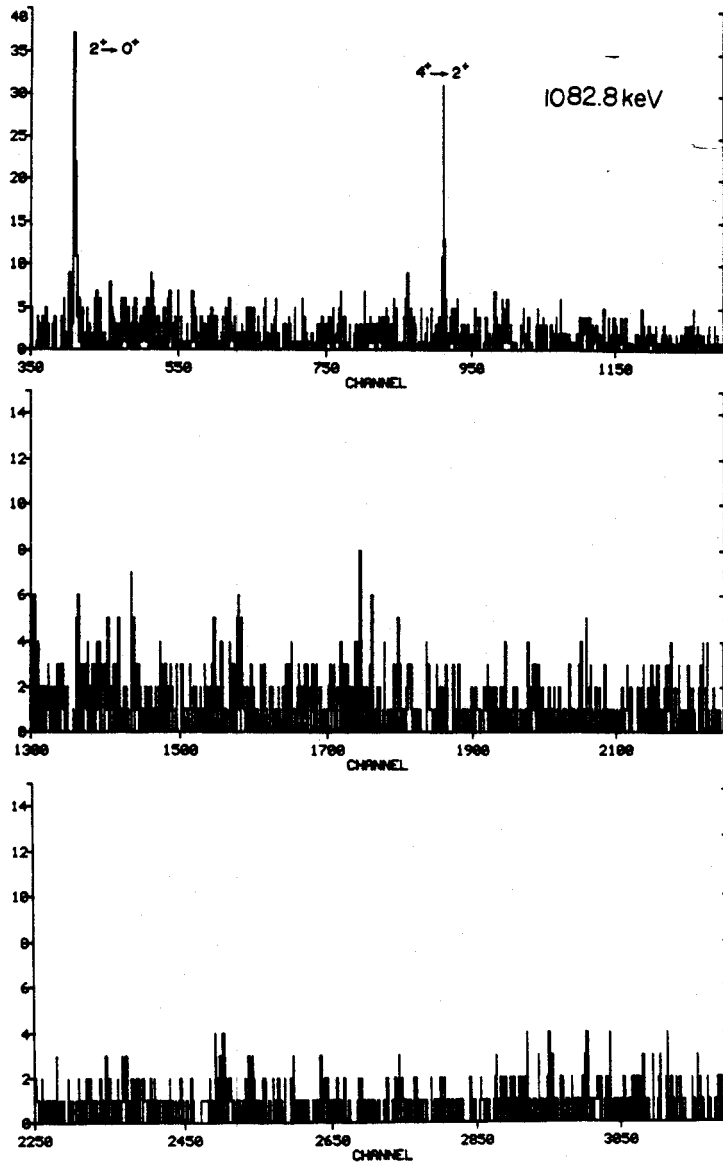Figure A4
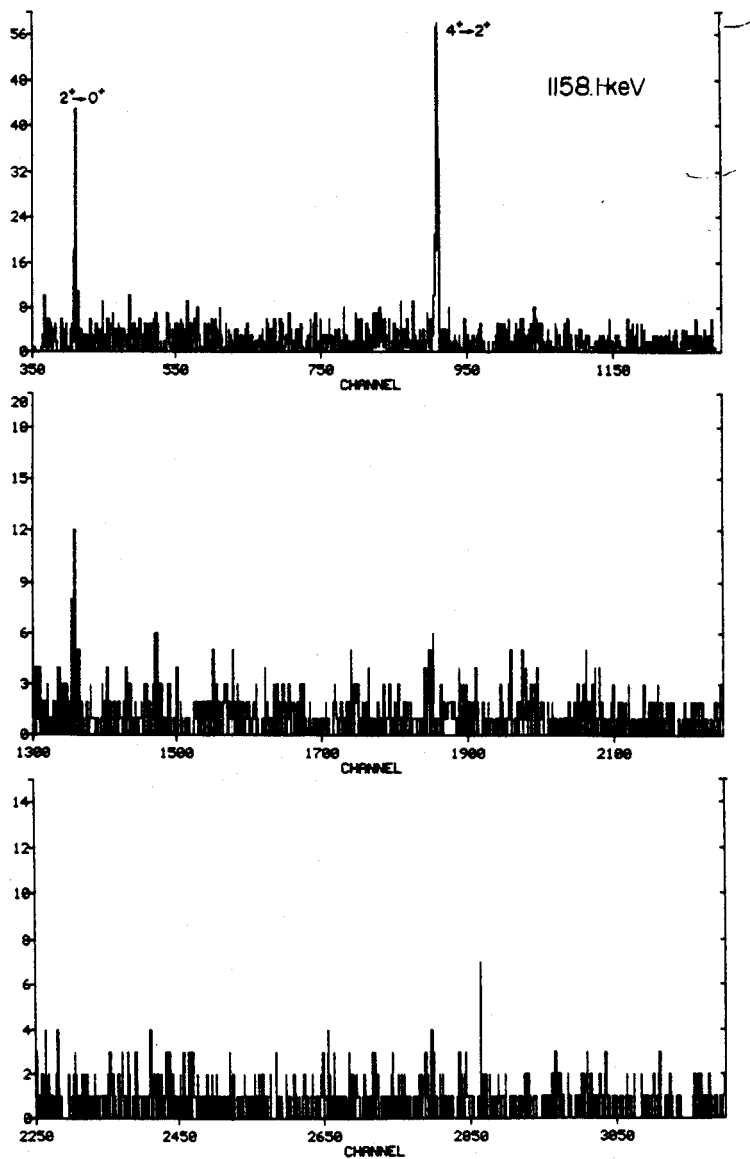
Figure A5
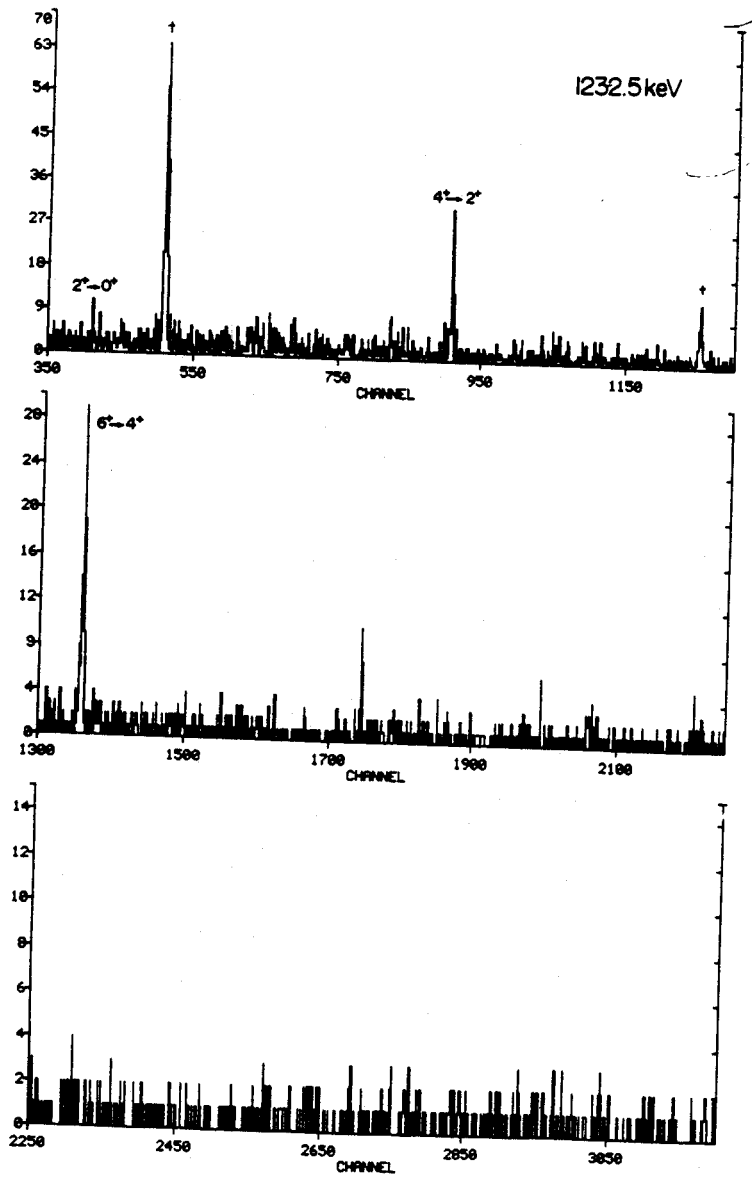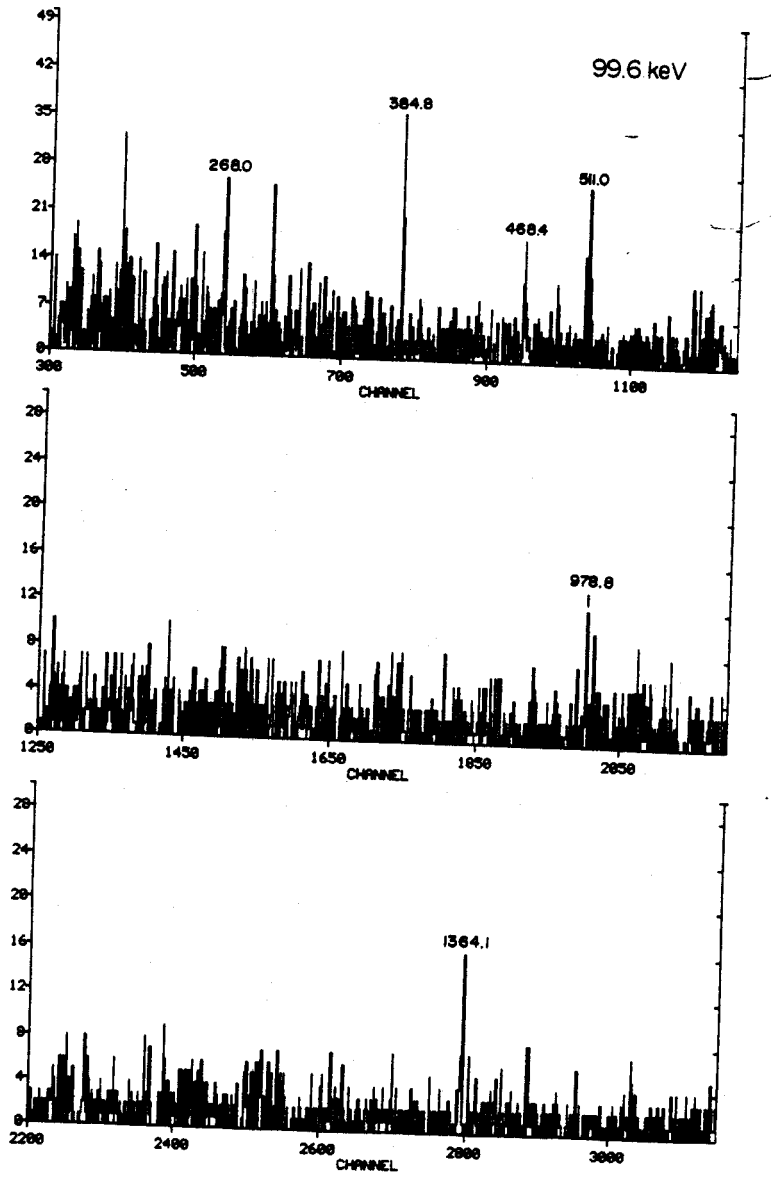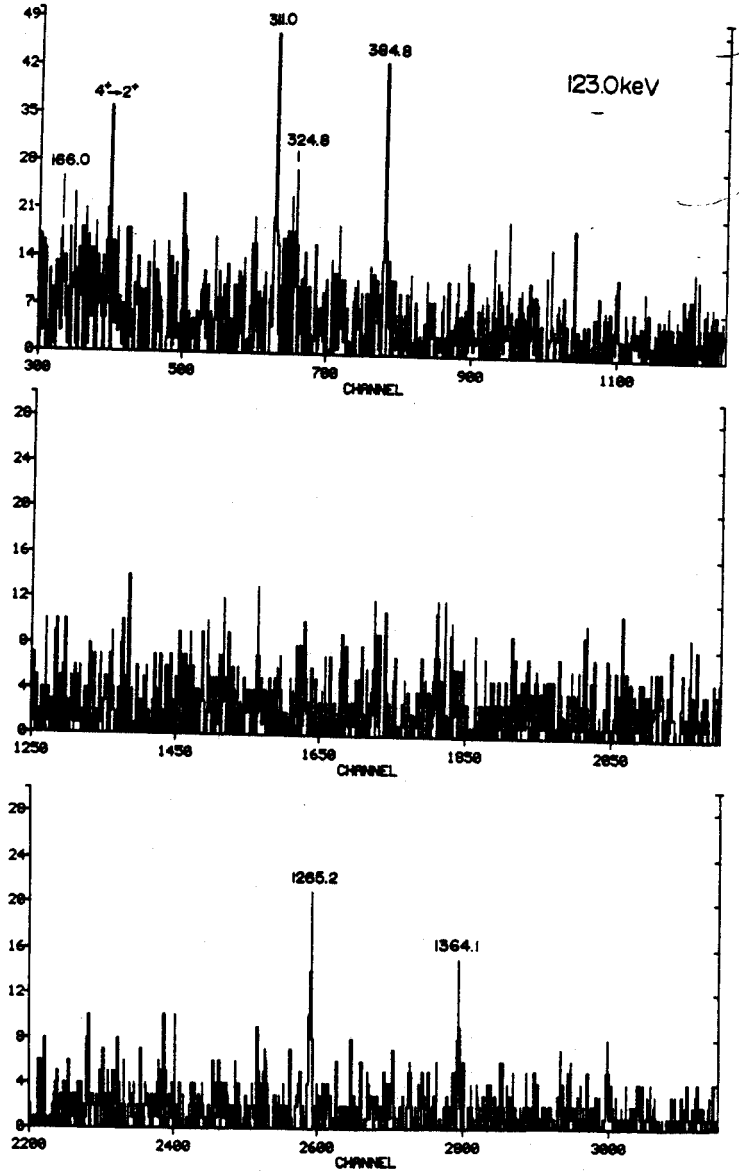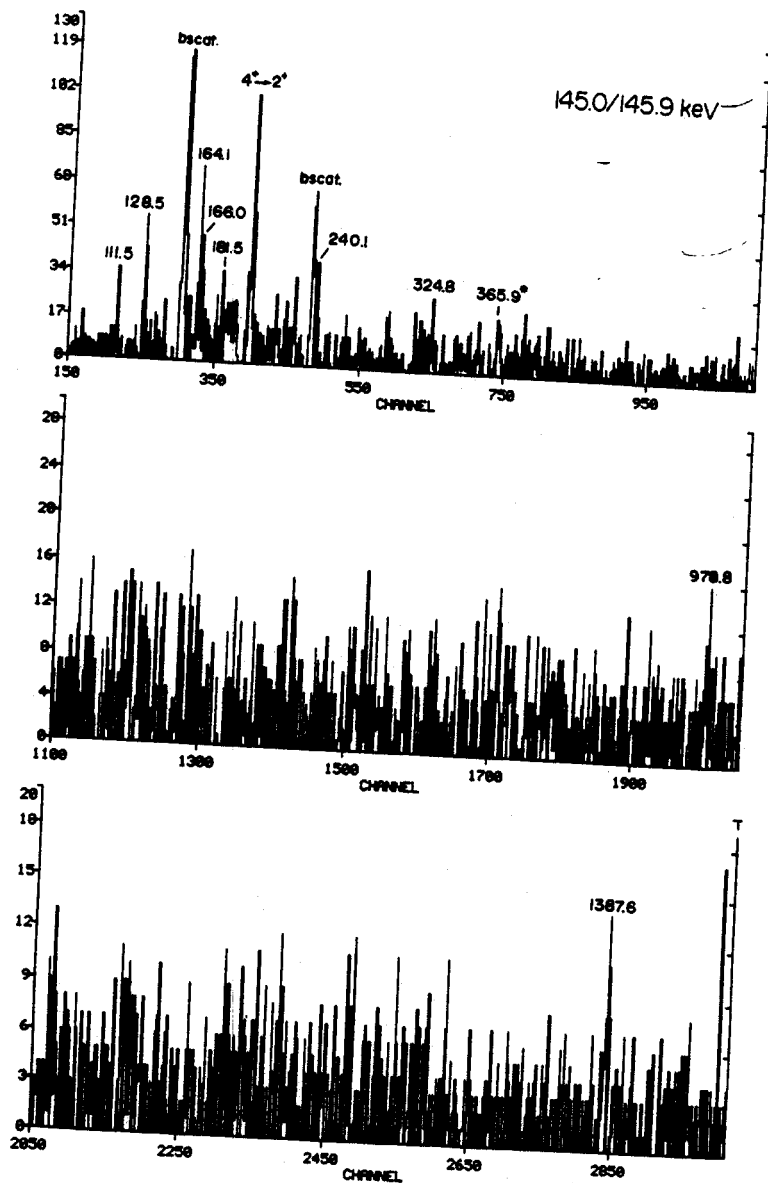
Figure A6

Figure A7

Figure A8

Figure A9

Figure A10

Figure A11

Figure A12

Figure A13

Figure A14

Figure A15
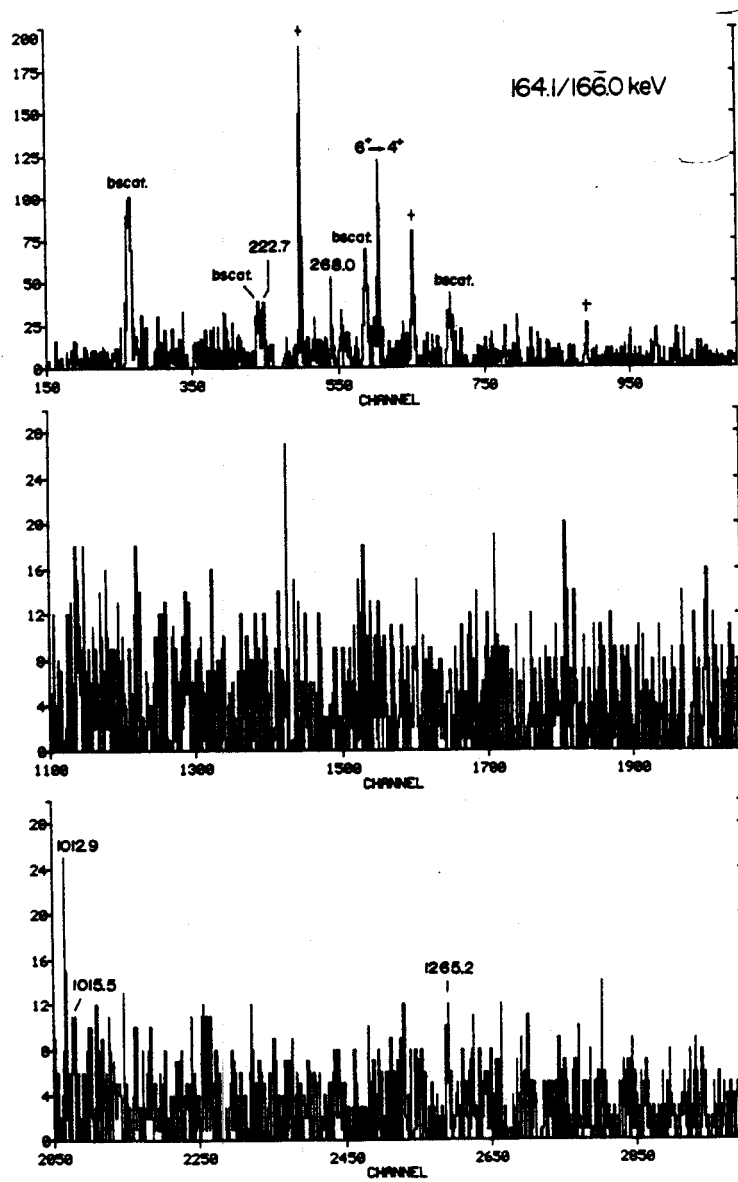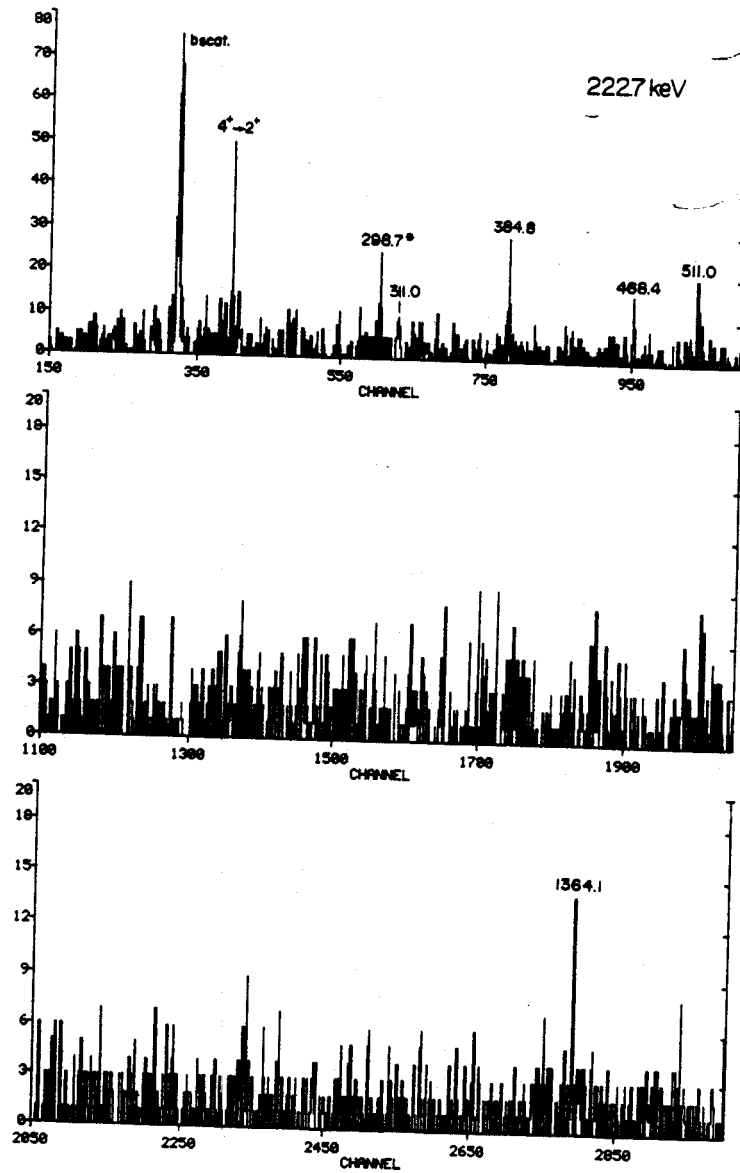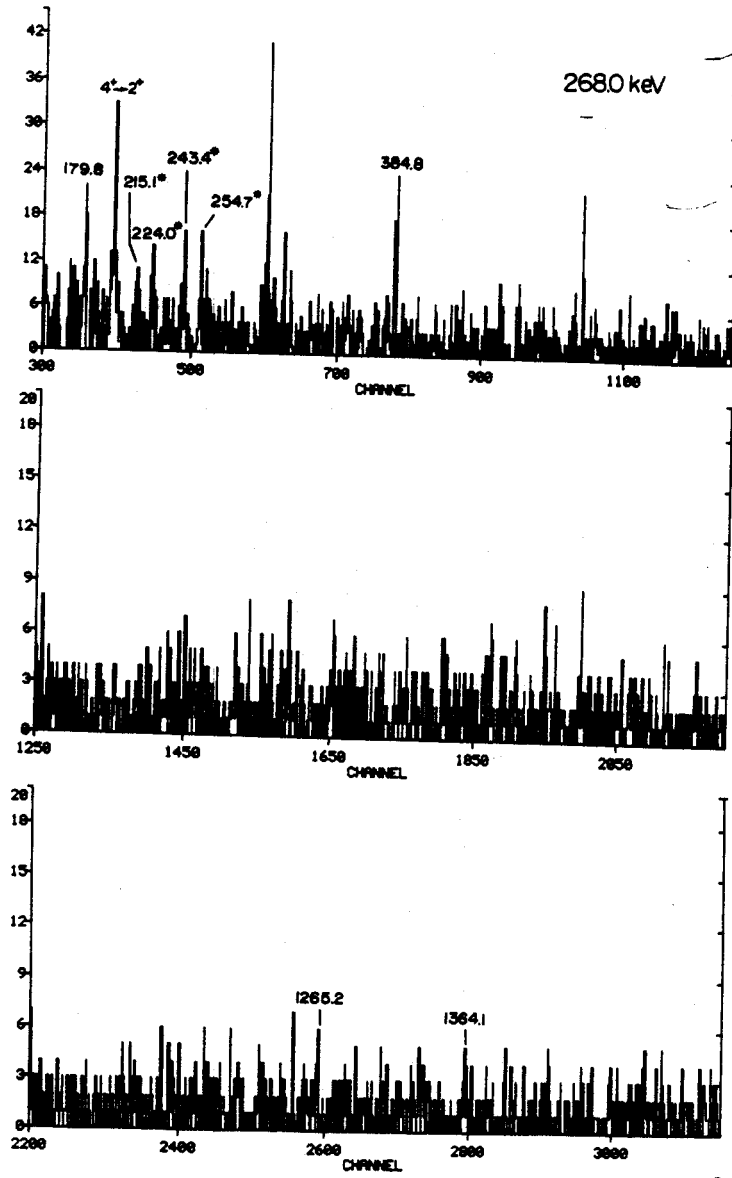
Figure A16

172

Figure A17

Figure A18
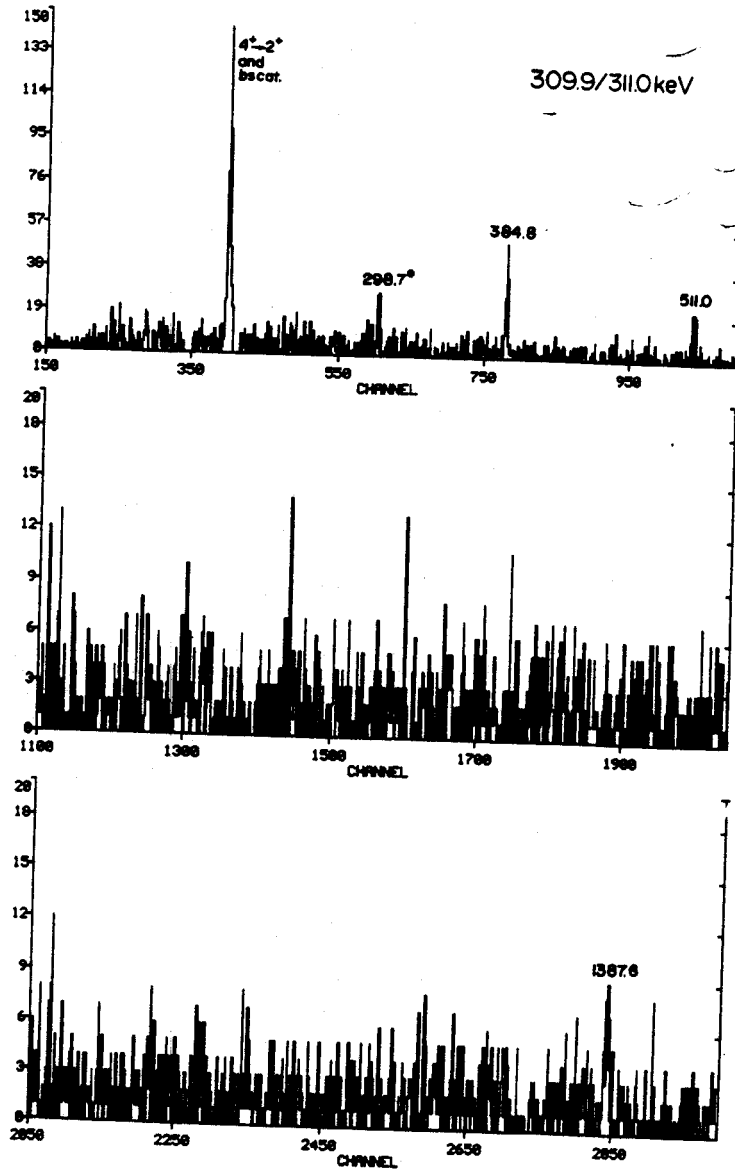
Figure A19

REFERENCES

REFERENCES

A

[An76] Andersson, G., Larsson, S.E., Leander, G., Moller, P.,
Nilsson, S.G., Ragnarsson, I., Aberg, S., Bengtsson, R.,
Dudek, J., Nerlo-Pomoska, B., Pomorski, K., and Szymanski, Z.,
Nucl. Phys. A268 (1976) 205.

[Au72] Au, R., IIEVENT, National Superconducting Cyclotron
Laboratory, Michigan State University, 1972, unpublished.

B

[Ba57a] Bardeen, J., Cooper, L.N., and Schreiffer, J.R., Phys. Rev.
106 (1957) 162.

[Ba57b] Bardeen, J., Cooper, L.N., and Schreiffer, J.R., Phys. Rev.
108 (1957) 1175.

[Be36] Bethe, H.A., and Bacher, R.F., Rev. Mod. Phys. 8 (1936) 82.

[Be37] Bethe, H.A., Rev. Mod. Phys. 9 (1937) 69.

[Be59] Belyaev, S.T., Mat. Fys. Medd. Dan. Vid. Selsk. 31, No. 11
(1959).

[Be77] Bengtsson, R., and Frauendorf, S., Proc. Int. Symp. on High-
Spin States and Nuclear Structure, Dresden, E. Germany,
September 1977.

[Be79a] Bengtsson, R., and Frauendorf, S., Nucl. Phys. A314 (1979) 27.

[Be79b] Bengtsson, R., and Frauendorf, S., Nucl. Phys. A237 (1979) 139.

[Bo36] Bohr, N., Nature 137 (1936) 344.

[Bo52] Bohr, A., Dan. Mat. Fys. Medd. 26, No. 14 (1952).

[Bo53] Bohr, A., and Mottelson, B.R., Dan. Mat. Fys. Medd. 27, No. 16
(1953).

[Bo69] Bohr, A., and Mottelson, B.R., Nuclear Structure, Vol. I
(Benjamin, New York, 1969).

[Bo75]   Bohr, A., and Mottelson, B.R., Nuclear Structure, Vol. II
         (Bemjamin, New York, 1975).

[Bo77]   Bohr, A., and Mottelson, B.R., Proc. Int. Conf. on Nucl.
         Struc., Tokyo, 1977.

[Bu67]   Burke, D.G., Elberk, B., Mat. Fys. Medd. Dan. Vid. Selsk. 36,
         No. 6 (1967).

                                C

[Ca69]   Camp, D.C. and Van Lehn, A.L., Nucl. Instr. Meth. 79 (1969)
         192.

[Ch70]   Charvet, A., Duffait, R., Emsallem, A., and Chery, R., Nucl.
         Phys. A156 (1970) 276.

[Ch72]   Charvet, A., Chery, R., Phuoc, D.H., Duffait, R., Emsallem, A.,
         and Marguier, G., Nucl. Phys. A197 (1972) 490.

[Ch73]   Charvet, A., Chery, R., Duffait, R., Morgue, M., and Sau, J.,
         Nucl. Phys. A213 (1973) 117.

[Che]   Chen, Y.S., private communication.

[Co74]   Conrad, J., Repnow, R., Grosse, E., Homeyer, H., Jalschke, E.,
         and Wurm, J.P., Nucl. Phys. A234 (1974) 157.

[CS78]   Frauendorf, S., and Bengtsson, R., "CS Code", Copenhagen, 1978.

                                D

[de74]   der Mateosian, E., and Sunyar, A.W., Atomic Data and Nuclear
         Data Tables 13 (1974) 392; ibid. 408.

[De74]   Dehnhardt, W., Mills, S.J., Miller-Veggian, M., Neumann, U.,
         Pelte, D., Poggi, G., Povh, B., and Taras, P., Nucl. Phys.
         A255 (1974) 1.

[Di66]   Diamond, R.M., Matthias, E., Newton, J.O., and Stephens, F.S.,
         Phys. Rev. Lett. 16 (1966) 1205.

[Dr77]   Dracoulis, G.D., Ferguson, S.M., Newton, J.O., and Slocombe,
         M.G., Nucl. Phys. A279 (1977) 251.

E

[Elb]   Elbek, B., unpublished.

F

[Fr81a]   Frauendorf, S., Nuclear Physics Workshop, International Center
            for Theoretical Physics, Trieste, October 1981.

[Fr81b]   Frauendorf, S., "The CSM Bible Lectures", University of
            Tennessee, April 1981.

G

[Ga80]   Gavron, A., Projection Angular Momentum Coupled Evaporation
            Monte Carlo Code (PACE), Oak Ridge National Laboratory, 1980,
            unpublished.

[Gav]   Gavron, A., private communication.

[Gi77]   Gizon, J., and Gizon, A., Z. Phys. A281 (1977) 99.

[Gi78]   Gizon, J., and Gizon, A., Z. Phys. A285 (1978) 259.

[Go74]   Goodman, A.L., Nucl. Phys. A230 (1974) 466.

[Gr67]   Grover, J.R., Phys. Rev. 157 (1967) 832.

[Gu67]   Gustafsson, C., Lamm, I.L., Nilsson, B., and Nilsson, S.G.,
            Ark. Fys. 36 (1967) 613.

H

[Ha49]   Haxel, O., Jensen, J.H.D., and Suess, H.E., Phys. Rev. 75
            (1949) 1766.

[Ha81]   Hattula, J., to be published.

I

[In54]   Inglis, D.R., Phys. Rev. 96 (1954) 1059.

[In69]   Inglis, D.R., Physics Today, 22 (1969) 29.

J

[Je70]   Jett, J.H., and Lind, D.A., Nucl. Phys. <u>A155</u> (1970) 182.

[Jo72]   Johnson, A., Ryde, H., and Hjorth, S.A., Nucl. Phys. <u>A179</u> (1972) 753.

[Jo81]   Johnson, N.R., unpublished.

K

[Kh73]   Khoo, T.L., Waddington, J.C., and Johns, M.W., Can. J. Phys. <u>51</u> (1973) 2307.

[Kr68]   Krumlinde, J., Nucl. Phys. <u>A121</u> (1968) 306.

L

[Li37]   Livingston, M.S., and Bethe, H.A., Rev. Mod. Phys. <u>9</u> (1937) .

[Lo70]   Lobner, K.E.G., Vetter, M., and Honig, V., Nucl. Data Tables <u>A7</u> (1970) 495.

M

[Ma49]   Mayer, M.G., Phys. Rev. <u>75</u> (1949) 209.

[Ma69]   Mariscotti, M.A.J., Schraff-Goldhaber, G., and Buck, B., Phys. Rev. <u>178</u> (1969) 1864.

[Mi59]   Migdal, A.B., Nucl. Phys. <u>13</u> (1959).

[Mi81a] Milner, W.T., Holifield Acquisition Task (HAC), Oak Ridge National Laboratory, 1981, unpublished.

[Mi81b] Milner, W.T., Disk Monitoring (DISMO), Oak Ridge National Laboratory, 1981, unpublished.

[Mi81c] Milner, W.T., Spectrum Analysis Program (SPASM), Oak Ridge National Laboratory, 1981, unpublished.

[Mo75]   Morgan, C.B., KKRECOVERY, National Superconducting Cyclotron Laboratory, Michigan State University, 1975, unpublished.

[Mo76]   Morinaga, H., and Yamazaki, T., <u>In-Beam Gamma-Ray Spectroscopy</u>, (North Holland, 1976).

[Ne70]   Neergard, K., and Vogel, P., Nucl. Phys. A145 (1970) 33.

[Ne76]   Neergard, K., Pashkevich, V.V., and Frauendorf, S., Nucl.
         Phys. A262 (1976) 61.

[Ni55]   Nilsson, S.G., Dan. Mat. Fys. Medd. 29, No. 16 (1955).

[Ni69]   Nilsson, S.G., Tsang, C.F., Sobiczewski, A., Szymanski, S.,
         Wycech, C., Gustafsson, G., Lamm, I.L., Moller, P., and
         Nilsson, B., Nucl. Phys. A231 (1969) 1.

[No1]   Nolan, P.J., Todd, D.M., Smith, P.J., Love, D.J.G., Twin, P.J.,
         Andersen, O., Garrett, J.D., Hagemann, G.B., and Herskind, B.,
         accepted for publication in Phys. Rev.

[NoP]   Nolan, P.J., private communication.

                              O

[Og71]   Ogle, W., Wahlborn, S., Pilpenbring, R., and Frederiksson, J.,
         Rev. Mod. Phys. 43 (1971) 424.

[Ow81a] Ower, H., Oak Ridge National Laboratory, 1981, unpublished.

[Ow81b] Ower, H., Oak Ridge National Laboratory, 1981, unpublished.

                              P

[Pl77]   Plasil, R., ORNL/TM-6054, Oak Ridge National Laboratory,
         November 1977.

[Pr75]   Preston, M.A., and Bhaduri, R.K., Structure of the Nucleus,
         (Addison-Wesley, Massachusetts, 1975).

                              R

[Ra50]   Rainwater, J., Phys. Rev. 79 (1950) 432.

[Ri80]   Riedinger, L.L., Proc. Int. Conf. on Band Structure and Nuclear
         Dynamics, New Orleans, Louisiana, 1980, and references therein.

[Ri81]   Riedinger, L.L., Phys. Scr. 24 (1981) 324, and references
         therein.

[Rie]   Riedinger, L.L., private communication.

[Ro05]   Routh, E.J., A Treatise on the Dynamics of a System of Rigid Bodies, Vol. II, 6th Ed. (Macmillan, London, 1905); reprinted by Dover, New York, 1955.

[Ro69]   Routti, J.T., and Prussin, S.G., Nucl. Instr. Meth. 72 (1969) 125.

[Ro81]   Roy, N., Jonsson, S., Ryde, H., Walus, W., Gaardhoje, J.J., Garrett, J.D., Hagemann, G.B., and Herskind, B., Internal Report, University of Lund, Sweden, November, 1981.

S

[St75]   Stephens, F.S., Rev. Mod. Phys. 47 (1975) 43.

[Sik]   Sikkeland, T., and Lebeck, D., CS8N, University of California, unpublished.

T

[Th62]   Thouless, D.J., and Valatin, J.G., Nucl. Phys. 31 (1962) 211.

[Tj68]   Tjom, P.O., and Elbek, B., Nucl. Phys. A107 (1968) 385.

W

[Wa67]   Ward, D., Stephens, F.S., and Newton, J.O., Phys.Rev.Lett. 19 (1967) 1247.

[Wa75]   Ward, D., Berschat, H., Butler, P.A., Colombani, P., Diamond, R.M., and Stephens, F.S., Phys.Lett. 56B (1975) 139, and references therein.

[Wa79]   Walker, P.M., Faber, S.R., Bentley, W.H., Ronningen, R.M., Firestone, R.B., and Bernthal, F.M., Phys. Lett. 86B (1979) 9.

[Wa80]   Walker, P.M., Faber, S.R., Bentley, W.H., Ronningen, R.M., and Firestone, R.B., Nucl. Phys. A343 (1980) 45.

[Wal]   Walker, P.M., Carvalho, J.L.S., and Bernthal, F.M., to be published.

Y

[Ya67]   Yamazaki, T., Nuclear Data A3 (1967) 1.